

Measurement of Reactor Anti-Neutrino Disappearance in KamLAND

Ph.D. Thesis

Toshiyuki Iwamoto
Graduate School of Science, Tohoku University
Sendai 980-8578, Japan

February 2003

Abstract

The flux of $\bar{\nu}_e$ from distant nuclear reactors has been measured using KamLAND, 1 kton liquid scintillator detector. Correlated positron-neutron events from the reaction $\bar{\nu}_e p \rightarrow e^+ n$ were recorded for a period of 145.1 days (162 ton·year). The ratio of the number of observed inverse β decay events to the expected number of events without disappearance is $0.611 \pm 0.085(\text{stat.}) \pm 0.041(\text{syst.})$ for $\bar{\nu}_e$ energies > 3.4 MeV. The deficit of events is inconsistent with the expected rate for standard $\bar{\nu}_e$ propagation at the 99.95 % confidence level. In the context of two-flavor neutrino oscillations with CPT invariance, these results exclude all oscillation solutions but the 'Large Mixing Angle' solution to the solar neutrino problem.

Acknowledgements

First of all, I would like to express my great appreciation to Professor Atsuto Suzuki, the spokesperson of the KamLAND experiment. He provided me with the opportunity to take part in this experiment from the first stage. He introduced me to the neutrino physics, and supported me during graduate studies. His excellent guidance and continuous encouragement were very valuable to me.

I would like to be thankful to my advisor, Associate Professor Fumihiko Suekane. He gave me many brilliant guidance and suggestions during graduate studies. Without his continuous encouragement and warm guidance, I could not have made this study. I would like to thank Associate Professor Kunio Inoue for very useful suggestions. He provided me a lot of precious guidance and suggestions for this analysis. I am thankful to Associate Professor Junpei Shirai for his helpful comments and advice.

I would like to especially thank the KamLAND collaborators. Many thanks to Dr. Masayuki Koga, Dr. Shuichiro Hatakeyama, Dr. Tadao Mitsui, Dr. Kenji Ishihara, Dr. Kengo Nakamura, Dr. Masakazu Motoki, Dr. Jesse Goldman, Dr. Yasuhiro Kishimoto, Dr. Koichiro Furuno for their helpful advice, comments and discussion about the experiment, physics and so on.

I would like to thank all people of Research Center for Neutrino Science (RCNS) at Tohoku University. Many thanks to Professor Toshio Kitagaki, Professor Koya Abe, Professor Akira Yamaguchi, Professor Hitoshi Yamamoto, Associate Professor Tomoki Hayashino, Dr. Takuya Hasegawa, Dr. Tadashi Nagamine for various suggestions and comments. Thanks to all members of the secretarial, technical and other staffs for their kindly support. Thanks to Hiroshi Ogawa, Sanshiro Enomoto, Osamu Tajima, Hideki Watanabe, Haruo Ikeda, Yoshihito Gando, Fumiaki Handa, Itaru Higuchi, Kyo Nakajima for the discussion about physics and analysis etc. Thanks to all the graduates and seniors of RCNS for their cooperation.

I gratefully acknowledge the cooperation of Kamioka Mining and Smelting Company and financial support of the Japan Society of the Promotion of Science.

Great appreciation goes to my parents, Hiroshi and Hideko Iwamoto, and sister, Masa Iwamoto for their unfailing support through these years. Also special thanks go to my parents-in-law, Hiroyuki and Setsue Kanbayashi, brothers-in-law, Takeshi Kanbayashi, for their heartfelt support and encouragement.

Finally, I want to express my great appreciation for my wife, Ayako. I couldn't complete this work without her patience, support and encouragement. I dedicate this thesis to her.

Contents

1	Introduction	1
1.1	The Neutrino	1
1.2	Neutrino Oscillation	2
1.3	Neutrino Oscillation Experiment	7
1.3.1	Solar Neutrinos	7
1.3.2	Atmospheric Neutrinos	8
1.3.3	Reactor Neutrinos	11
1.4	Reactor Anti-Neutrino Oscillations at KamLAND	11
2	Detector	21
2.1	Detection Method	21
2.2	Site	23
2.3	Design	23
2.4	Balloon	25
2.5	PMTs	25
2.6	Liquid Scintillator and Buffer Oil	28
2.7	Purification System	29
2.8	Front-End Electronics	30
2.9	Trigger	32
2.10	Veto Counter	33
2.11	Water Purification	33
2.12	Calibration System	33
3	Event Reconstruction	34
3.1	Waveform Analysis	34
3.1.1	Raw Data	34
3.1.2	Pedestal Subtraction	35
3.1.3	TQ Fit	37
3.2	Vertex Fitter	40
3.3	Energy Fitter	43
3.3.1	Gain Correction	43

3.3.2	Energy Fitter	44
3.4	Trigger Efficiency	48
3.5	Muon Fitter	50
4	Calibration	53
4.1	PMT gain	53
4.2	PMT timing	54
4.3	Energy Scale	57
5	Event Selection	63
5.1	Detector livetime	63
5.2	Bad Run Selection	65
5.3	Charge Selection	65
5.4	Noise Cut	68
5.4.1	Noise Event	68
5.4.2	Flasher Event	70
5.5	Muon 2ms Cut	70
5.6	Fiducial Selection	71
5.7	Space, Time Correlation	75
5.8	Energy Cut	78
5.9	Spallation Cut	79
5.10	Final Sample	81
6	Background Estimation	84
6.1	Accidental Background	84
6.2	Correlated Background	85
6.2.1	Natural Radioactivity	85
6.2.2	Spallation Background	94
6.2.3	Terrestrial Neutrino Background	100
6.2.4	Atmospheric Neutrino Background	102
6.2.5	Summary	103
7	Analysis	105
7.1	Expected Reactor Flux	105
7.1.1	Reactor Distance from KamLAND	105
7.1.2	Reactor Thermal Power and Fuel Composition	106
7.1.3	Neutrino Flux from Each Fuel	108
7.1.4	Cross-Section	109
7.1.5	Number of Targets	109
7.1.6	Neutron Capture on Proton	111
7.1.7	$\bar{\nu}_e$ Detection Efficiency	111
7.1.8	Expected Reactor Flux	112

7.2	Summary of the Systematic Uncertainties	115
7.3	No Oscillation Probability	115
7.4	Oscillation Analysis	117
7.5	Impact for Neutrino Physics	122
8	Conclusion	125
A	No Spallation Cut Analysis	126

List of Figures

1.1	Exclusion limits and preferred parameter regions from $\nu_e \leftrightarrow \nu_\mu$ oscillation experiments	6
1.2	Allowed regions of the solar neutrino parameter space after the SNO	9
1.3	Zenith angle distribution at SK	10
1.4	The locations of the Japanese commercial reactors and KamLAND.	12
1.5	Example of the fuel burn-up at a Palo Verde Reactor	15
1.6	Example of the fuel burn-up at a Japanese reactor	17
1.7	Neutrino spectrum from four isotopes.	18
1.8	Expected energy spectrum of $\bar{\nu}_e$ at KamLAND	19
1.9	Sensitivity of KamLAND	20
2.1	Total cross section of the reaction, $\bar{\nu}_e + p \rightarrow n + e^+$	23
2.2	Schematic view of the KamLAND detector	24
2.3	detail of the KamLAND detector	24
2.4	Transparency to light of the KamLAND balloon.	26
2.5	Schematic view of the 17-inch and 20-inch PMTs.	26
2.6	The quantum efficiency of KamLAND PMTs.	27
2.7	Emission spectrum of the liquid scintillator.	28
2.8	The refractive index of the detector components.	29
2.9	Schematic view of the KamLAND purification system.	30
2.10	12-channel KamLAND Front-End Electronics board.	31
2.11	Schematic diagram of a KamLAND Front-End Electronics board.	31
3.1	Two different examples of raw waveforms	35
3.2	Examples of mean pedestal values of a PMT	36
3.3	Two different examples of waveform fitting	38
3.4	KamLAND event display.	39
3.5	Measured effective speed of light as a function of z position.	40
3.6	Timing histogram at the beginning and the final of the vertex reconstruction.	41
3.7	Vertex reconstructions at different positions along the z axis.	41
3.8	Vertex fitter performances along with z-axis.	42

3.9	the vertex distribution of the spallation neutron samples as the function of R^3	43
3.10	The vertex position of the spallation neutron samples as a function of the $\cos\theta$	44
3.11	PMT gain stability dependence on run number	45
3.12	Number of bad PMTs as a function of the run number.	45
3.13	Corrected charge as a function of the vertex position z	46
3.14	Charge dependence on the vertex position using the spallation neutron samples	47
3.15	Charge distribution of the neutron induced by muon spallation	48
3.16	Prompt trigger efficiency	49
3.17	Delayed trigger efficiency	49
3.18	Charge distribution with the events selected as muons and time difference distribution from muon to muon	50
3.19	KamLAND event display for the muon event.	51
3.20	Relation with muon track length versus charge	52
4.1	Single photo-electron distribution of a typical 17-inch PMT	53
4.2	mean single photo-electron peaks of all PMTs before and after gain calibration	54
4.3	Laser calibration system set up.	55
4.4	Example of TQ map for one PMT	56
4.5	timing distribution of all PMTs before and after timing calibration	56
4.6	Energy distribution of ^{60}Co calibration	57
4.7	Energy distribution of ^{65}Zn calibration	58
4.8	Energy distribution of ^{68}Ge calibration	59
4.9	Energy distribution of 2.22, 4.95 MeV γ from muon induced neutron capture	59
4.10	Visible energy versus original source energy	62
4.11	The fractional difference of the reconstructed energy	62
5.1	KamLAND detector operation conditions	64
5.2	OD PMT hits versus total charge of inner detector	66
5.3	Distribution of the number of OD PMT hits	67
5.4	Total charge distribution of the inner detector with muons and low energy events	67
5.5	Time distribution of the normal and noise events	68
5.6	Noise event selection criteria	69
5.7	Flasher cut conditions	71
5.8	Energy spectrum before and after muon 2ms cut with fiducial 5 m.	72
5.9	Charge distribution after Muon, flasher, noise and muon 2 msec cut	72
5.10	Energy spectrum at various fiducial volumes	73
5.11	Vertex distribution of the delayed coincidence events	74
5.12	Vertex distribution of the low energy events as functions of R and Z	75

5.13	Energy spectrum of single events with fiducial cut	76
5.14	Simulated vertex correlation and the detection inefficiency	77
5.15	Detection efficiency distribution dependent on the vertex position from the space correlation	77
5.16	Timing distribution of very close coincidence events	78
5.17	Neutron capture time of muon induced neutrons	79
5.18	Residual charge distribution of showering and non-showering muons	80
5.19	Dead volume dependence on the muon track	80
5.20	The various profiles of $\bar{\nu}_e$ events. Prompt, delayed energy, space and time correlation histograms are shown. Lines are the selection criteria and all the cut except one for each figures are applied.	82
5.21	Time vs vertex, prompt vs delayed energy, delayed energy vs space cor- relation and delayed energy vs time correlation are shown. Lines are the selection criteria and all the cut except one for each figures are applied. . .	83
6.1	Time and energy spectrum of accidental coincidence events	85
6.2	Prompt and delayed energy spectra of ^{214}Bi - ^{214}Po coincidence events	88
6.3	Prompt and delayed energy spectrum of ^{212}Bi - ^{212}Po coincidence events . .	89
6.4	Time and vertex distribution of the ^{214}Bi - ^{214}Po coincidence events	89
6.5	Time and Vertex distribution of the ^{212}Bi - ^{212}Po coincidence events	90
6.6	Vertex correlation of ^{214}Bi - ^{214}Po events	91
6.7	Content of ^{238}U and ^{232}Th in the liquid scintillator	92
6.8	Radon concentration in the center cylindrical region with radius 1 m	93
6.9	$^8\text{He}/^9\text{Li}$ energy spectrum	96
6.10	Decay time distribution of ^8He , ^9Li samples	97
6.11	Tracking efficiency of the muon and time distribution of ^8He and ^9Li events with the distance more than 3 m from non-showering muon	98
6.12	Various plots of fast neutron events	99
6.13	Energy spectrum of the protons recoiled by fast neutrons.	100
6.14	Expected geo $\bar{\nu}_e$ energy spectrum	101
6.15	Atmospheric $\bar{\nu}_e$ fluxes with different models	103
6.16	Background energy spectrum	104
7.1	Fission flux at KamLAND from each reactor versus the distance to Kam- LAND.	108
7.2	Uncertainties of neutrino spectra from four isotopes	109
7.3	Energy spectrum of the AmBe source	112
7.4	Space correlation of 4.44 MeV γ and neutron captured 2.22 MeV γ from AmBe source	113
7.5	Expected reactor $\bar{\nu}_e$ energy spectrum at KamLAND.	114
7.6	$\bar{\nu}_e$ energy spectra distortions at various oscillation parameters	114
7.7	Observed and expected reactor $\bar{\nu}_e$ energy spectra	115

7.8	Ratio of measured to expected $\bar{\nu}_e$ flux from reactor experiments	118
7.9	Excluded regions of neutrino oscillation parameters	119
7.10	MSW effect at KamLAND	121
7.11	Excluded regions of neutrino oscillation parameters with matter effects . .	122
A.1	timing distribution of $\bar{\nu}_e$ without spallation cut from the last muon with 0.9 MeV threshold	127
A.2	timing distribution of $\bar{\nu}_e$ without spallation cut from the last muon with 2.6 MeV threshold	127

List of Tables

1.1	The summary of the sensitivities and results of previous reactor experiments.	11
1.2	Thermal power, number of cores, distance, and thermal power flux at KamLAND from Japanese and Korean reactors.	13
1.3	Energy release per fission	15
5.1	Number of events at each selection step	82
6.1	Decay schemes of ^{214}Bi - ^{214}Po and ^{212}Bi - ^{212}Po decay chains	86
6.2	Selection criteria for the ^{214}Bi - ^{214}Po and ^{212}Bi - ^{212}Po delayed coincidence events.	87
6.3	Summary of the detection efficiency and the systematic error of the ^{214}Bi - ^{214}Po events.	91
6.4	Summary of the detection efficiency and the systematic error of the ^{212}Bi - ^{212}Po events.	91
6.5	Summary of the nuclei for neutron emitter	95
6.6	The summary of the background rates from different sources.	103
7.1	Detailed distances from KamLAND to reactor cores and the types	107
7.2	The summary of the number of atoms in the liquid scintillator.	110
7.3	The summary of the energy and the probability of the captured neutron by different nuclei.	111
7.4	Summary of the detection efficiency for $\bar{\nu}_e$ delayed coincidence.	111
7.5	Summary of the systematics for the $\bar{\nu}_e$ detection.	116

Chapter 1

Introduction

For a long time the solar neutrino problem that there is a deficit of neutrinos emanating from the sun has been discussed. An apparent solution to this problem is the theory of neutrino oscillations, particularly in light of the compelling atmospheric neutrino data from Super-Kamiokande (SK). The Sudbury Neutrino Observatory (SNO) charged current (CC) and neutral current (NC) measurements of solar neutrino flux have provided strong evidence for neutrino flavor conversion. In the context of the SK results, the presence of a non-electron flavor active neutrino component in the solar ν_e flux has been established at the 5.5σ level. The SNO and SK results, together with the data from the radiochemical experiments, Homestake, Gallex, GNO and SAGE favor the Large Mixing Angle (LMA) solution based on the MSW resonant matter conversion as the most probable solution of the solar neutrino puzzle. This solution is characterized by the best fit values of $\tan^2\theta = 0.41$, $\Delta m^2 = 6.06 \times 10^{-5} \text{ eV}^2$ for the neutrino mixing parameters. The KamLAND was designed to explore the LMA solution through the detection of reactor anti-neutrinos.

The structure of this chapter is as follows. The history and the general explanation of the neutrino are described in section 1.1. The deficits in the observed solar neutrino flux and a discussion of neutrino oscillations as the most likely solution can be found in section 1.2. Neutrino oscillation experiments using various sources are summarized in section 1.3 and lastly, neutrino oscillations at KamLAND are discussed in section 7.1.2.

1.1 The Neutrino

The neutrino was introduced by W. Pauli in 1930 to conserve energy in nuclear β decay which required a final state electrically neutral particle with a spin of $1/2$ [1]. Anti-neutrinos from reactors were discovered by F. Reines and C. Cowan in 1956 [2] by making use of the reaction $\bar{\nu}_e + p \rightarrow n + e^+$. The positron and electron annihilate, giving two simultaneous photons. The neutron is thermalized until it is eventually captured by a Cadmium nucleus, emitting photons some 15μ seconds after the positron signal. These

delayed coincidence signals were detected and the existence of the neutrino was confirmed. The neutrinos produced in association with muons were observed at the Brookhaven National Laboratory in 1962 [3] and were found not to be the same as those produced in association with electrons. This was the discovery of a second type of neutrino (ν_μ). The tau particle was discovered at the Stanford Linear Accelerator Center in 1975 [4] and its associated tau neutrino was also discovered by DONUT Collaboration in 2000 [5]. The precise measurement of the decay width of the Z boson in $e^+ e^-$ collider at LEP constrains the number of light neutrino families to three [6].

In the Standard Model, 12 particles, 6 quarks and 6 leptons, are the constituents of matter. All of these have been discovered experimentally. Each charged lepton (electron, muon, tau) is associated with a neutral lepton or neutrino (ν_e, ν_μ, ν_τ). The quarks are grouped by pairs according to the same rule and so the three generations of leptons and quarks can be written down as follows.

$$\begin{pmatrix} \nu_e \\ e \end{pmatrix} \begin{pmatrix} \nu_\mu \\ \mu \end{pmatrix} \begin{pmatrix} \nu_\tau \\ \tau \end{pmatrix} \quad \text{leptons}$$

$$\begin{pmatrix} u \\ d \end{pmatrix} \begin{pmatrix} c \\ s \end{pmatrix} \begin{pmatrix} t \\ b \end{pmatrix} \quad \text{quarks}$$

In the standard model, the neutrino has a zero mass, a zero charge and a spin 1/2.

Because neutrinos are electrically neutral, they are not affected by the electro-magnetic interactions which act on electrons and other charged particles. They are affected only by a weak interaction of much shorter range than electromagnetism, and are therefore able to travel great distances in matter without interacting.

There is no compelling reason why neutrinos should have zero mass (like the photon), and many experiments have tried to find the neutrino mass directly by measuring the energy spectrum of tritium β decays. There was no evidence of finite mass, and the upper limit for the $\bar{\nu}_e$ mass is now 3 eV at 95% C.L [7]. So, the neutrino mass is lighter than that of the electron by more than 5 orders of magnitude. This large mass difference between electron and ν_e can not be explained naturally by the standard model, and may imply new physics.

1.2 Neutrino Oscillation

Neutrino oscillations take place when physical mass eigenstates ν_i differ from flavor eigenstates ν_α , where ν_α is defined to be the neutrino state which connects to a charged lepton α via charged current interactions. The flavor eigenstate ν_α can be expressed as a linear combination of the mass eigenstates ν_i , $\nu_\alpha = \sum_i U_{\alpha i} \nu_i$, where U is a unitary mixing matrix.

A mass eigenstate of generation i after a time interval t is given by

$$|\nu_i(t)\rangle = e^{-iE_i t} |\nu_i(0)\rangle.$$

A neutrino of the generation α after a time interval of t is given by

$$\begin{aligned} |\nu_\alpha(t)\rangle &= \sum_i U_{\alpha i} |\nu_i(t)\rangle \\ &= \sum_i U_{\alpha i} e^{-iE_i t} |\nu_i(0)\rangle \end{aligned}$$

The time propagation equation of a flavor eigenstate neutrino can be written,

$$|\nu_\alpha(t)\rangle = U_{\alpha i} e^{-iE_i t} U_{i\alpha}^\dagger |\nu_\alpha(0)\rangle$$

To simplify the discussion, we assume that only two neutrino flavors are mixed, that is, ν_e and ν_μ . It is a convenient assumption for such the case as the disappearance experiment $\nu_e \rightarrow \nu_x$. If ν_x are thought to be the state like the linear combination of ν_μ and ν_τ , this flavor transition is regarded to be a purely two-flavor transition. The mixing matrix U then depends only on one mixing angle θ , and the oscillation probability is given by a simple formula.

$$\begin{pmatrix} \nu_e \\ \nu_\mu \end{pmatrix} = \begin{pmatrix} \cos \theta & \sin \theta \\ -\sin \theta & \cos \theta \end{pmatrix} \begin{pmatrix} \nu_1 \\ \nu_2 \end{pmatrix}.$$

The flavor transition probability $\nu_e \rightarrow \nu_e$ after a time interval t is

$$P(\nu_e \rightarrow \nu_e) = |\langle \nu_e(0) | \nu_e(t) \rangle|^2$$

Combining the above expressions gives the relation,

$$\begin{aligned} P(\nu_e \rightarrow \nu_e) &= \left| \begin{pmatrix} 1 & 0 \end{pmatrix} \begin{pmatrix} \cos \theta & \sin \theta \\ -\sin \theta & \cos \theta \end{pmatrix} \begin{pmatrix} e^{-iE_1 t} & 0 \\ 0 & e^{-iE_2 t} \end{pmatrix} \begin{pmatrix} \cos \theta & -\sin \theta \\ \sin \theta & \cos \theta \end{pmatrix} \begin{pmatrix} 1 \\ 0 \end{pmatrix} \right| \\ &= \left| e^{-iE_1 t} \cos^2 \theta + e^{-iE_2 t} \sin^2 \theta \right|^2 \end{aligned}$$

For $p \gg m_i$, E_i is expanded as $E_i = \sqrt{p^2 + m_i^2} \simeq p + m_i^2/2p \simeq p + m_i^2/2E$, the survival probability for a neutrino of energy E at a distance L from the origin is

$$\begin{aligned} P(\nu_e \rightarrow \nu_e) &= 1 - \sin^2 2\theta \sin^2 \frac{m_1^2 - m_2^2}{4p} t \\ &\simeq 1 - \sin^2 2\theta \sin^2 1.27 \frac{\Delta m^2 (\text{eV}^2) L (\text{m})}{E (\text{MeV})} \end{aligned}$$

where $\Delta m^2 \equiv m_2^2 - m_1^2$.

To test for oscillations, one can perform either an appearance search, in which one looks for new neutrino flavors, or a disappearance test in which one looks for a deficit of the original flavor in the flux at the detector.

When neutrinos propagate in matter, such as in the solar interior, their oscillation pattern may be modified. This happens because electron neutrinos can forward scatter on electrons by charged current interactions while other neutrino flavors cannot. Under such circumstances, a resonance enhancement of the oscillation amplitude. The effect was first pointed out by Wolfenstein. Mikheyev and Smirnov applied the effect to the solar neutrino problem and found the possibility of resonant enhancement of oscillations in the matter of the sun. Therefore, it is called the MSW effect [8].

The potential of ν_e is different from the other types of neutrinos because of its charged current interaction of ν_e . This additional potential energy is calculated to be

$$V_e = \sqrt{2}G_F N_e,$$

where G_F is the Fermi coupling constant and N_e is the electron number density. In the case of neutrino propagation in matter, the following equation is formed to obtain the time evolution of each neutrino flavor,

$$i \frac{d}{dt} \begin{pmatrix} \nu_e \\ \nu_\mu \end{pmatrix} = \left[U \begin{pmatrix} E_1 & 0 \\ 0 & E_2 \end{pmatrix} U^{-1} + \begin{pmatrix} V_e & 0 \\ 0 & 0 \end{pmatrix} \right] \begin{pmatrix} \nu_e \\ \nu_\mu \end{pmatrix}$$

Taking out a common diagonal phase factor, the above equation can be rewritten

$$i \frac{d}{dt} \begin{pmatrix} \nu_e \\ \nu_\mu \end{pmatrix} = \begin{pmatrix} -\frac{\Delta m^2}{4E} \cos 2\theta + V_e & \frac{\Delta m^2}{4E} \sin 2\theta \\ \frac{\Delta m^2}{4E} \sin 2\theta & \frac{\Delta m^2}{4E} \cos 2\theta \end{pmatrix}$$

Here, the eigenvector of the above matrix, which is analogous to vacuum oscillations, is defined as,

$$\begin{pmatrix} \nu_e \\ \nu_\mu \end{pmatrix} = \begin{pmatrix} \cos \theta_m & \sin \theta_m \\ -\sin \theta_m & \cos \theta_m \end{pmatrix} \begin{pmatrix} \nu_1^m \\ \nu_2^m \end{pmatrix}$$

where ν_1^m and ν_2^m are considered as mass eigenstates of neutrinos in matter, and θ_m is the neutrino mixing angle in matter which is

$$\tan 2\theta_m = \frac{\sin 2\theta}{\frac{2EV_e}{\Delta m^2} - \cos 2\theta}$$

The mixing angle is also written down as

$$\sin^2 2\theta_m = \frac{\sin^2 2\theta}{\sin^2 2\theta + \left(\frac{A}{\Delta m^2} - \cos 2\theta\right)^2}$$

where $A = 2\sqrt{2}EG_F N_e$.

The mass eigenstates E_1^m and E_2^m are given by

$$E_{1,2}^m = \frac{\frac{A}{\Delta m^2} \pm \sqrt{\left(\frac{A}{\Delta m^2} - \cos 2\theta\right)^2 + \sin^2 2\theta}}{\frac{2E}{\Delta m^2}}$$

It is now easy to find the probability of $\nu_e \leftrightarrow \nu_\mu$ oscillation in matter,

$$P(\nu_e \rightarrow \nu_\mu) = \sin^2 2\theta_m \sin^2\left(\pi \frac{L}{L_m}\right)$$

where L_m is the oscillation length in matter and is given by

$$L_m = \frac{2\pi}{E_2^m - E_1^m} = \frac{\frac{4\pi E}{\Delta m^2}}{\sqrt{\sin^2 2\theta + \left(\frac{A}{\Delta m^2} - \cos 2\theta\right)^2}}.$$

For anti-neutrinos, one must replace V_e by $-V_e$.

If the following condition, $A/\Delta m^2 = \cos 2\theta$ ($\theta_m = \pi/4$), is satisfied, neutrino mixing is greatly enhanced even with a small vacuum mixing angle, $\sin^2 2\theta$. This is called resonance condition.

Fig.1.1 shows the exclusion limits as well as preferred parameter regions from $\nu_e \leftrightarrow \nu_\mu$ oscillation experiments in the context of two-flavor neutrino oscillations [11]. Lines indicate 90% exclusion limits for parameters at larger Δm^2 and $\tan^2 \theta$ (or $\sin^2 2\theta$) and filled regions indicate allowed parameters at the 90% and 99% C.L.'s, except where marked as excluded (the Super-Kamiokande zenith angle spectrum exclusion regions). CPT invariance is assumed and neutrino and anti-neutrino limits are both shown.

The neutrinos coming from the decay $\mu^+ \rightarrow e^+ \nu_e \bar{\nu}_\mu$ from μ^+ at rest were studied by the Liquid Scintillator Neutrino Detector (LSND) experiment [10]. While this decay does not include $\bar{\nu}_e$, an excess of $\bar{\nu}_e p \rightarrow e^+ n$ scattering was observed above the expected background. This excess is interpreted as due to oscillation of some of the $\bar{\nu}_\mu$ produced by μ^+ decay into $\bar{\nu}_e$. The corresponding allowed regions (labeled as LSND) for oscillation parameters are shown in Fig.1.1. The related KARlsruhe Rutherford Medium Energy Neutrino (KARMEN) experiment sees no indication for such an excess and doesn't confirm the LSND experiment [12]. The preferred region from LSND is restricted by this result (labeled as KARMEN2). LSND result must be confirmed or refuted by other experiments such as MiniBooNE [13].

Both solar and atmospheric neutrino measurements have yielded significantly smaller interaction rates than expected. The solar neutrino problem and the atmospheric neutrino anomaly can be explained by neutrino flavor transformations caused by oscillations. Solar neutrino experiments detect predominantly ν_e 's and atmospheric experiments detect ν_μ . The explanation for the solar neutrino experiments is described in the section 1.3.1, and that for the atmospheric neutrino experiments is described in the section 1.3.2. Four allowed regions LMA, LOW, SMA and VAC from all solar neutrino experiments are shown in Fig.1.1. Two of them, SMA and VAC, are excluded by the zenith angle spectrum measurement of Super-Kamiokande [14].

There is no positive oscillation signal from reactor anti-neutrino measurements, and the excluded regions are only shown in Fig.1.1. The best limit for Δm^2 parameter is obtained by the CHOOZ experiment. These are explained in the section 1.3.3.

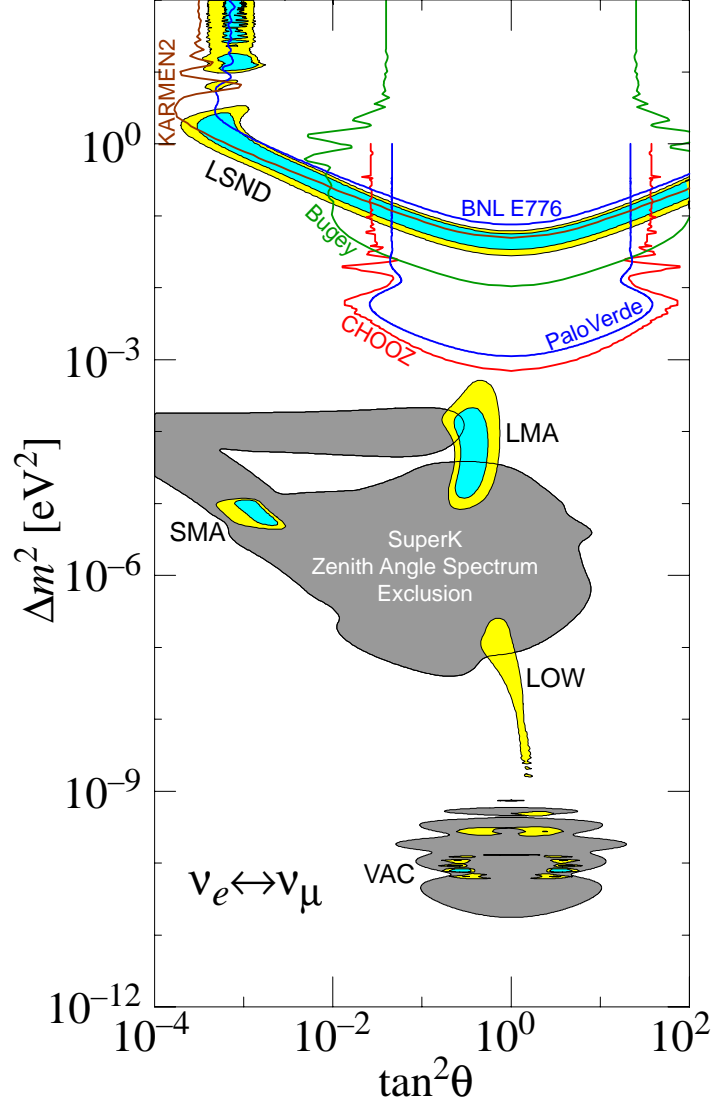


Figure 1.1: Exclusion limits and preferred parameter regions from $\nu_e \leftrightarrow \nu_\mu$ oscillation experiments in the context of two-neutrino oscillations [11].

By the way, the experiments such as $\bar{\nu}_\mu \rightarrow \bar{\nu}_e$ are called as appearance experiments. Appearance experiments are suitable to test the small mixing angle region. On the contrary, the experiments such as $\bar{\nu}_e \rightarrow \bar{\nu}_e$ and $\nu_e \rightarrow \nu_e$, are called as disappearance experiments. Reactor experiments and solar neutrino experiments are suitable to test small Δm^2 regions by making use of the low energy neutrino source and the long distance to the detector.

1.3 Neutrino Oscillation Experiment

1.3.1 Solar Neutrinos

The first solar neutrino observation was carried out by R. Davis and his Brookhaven collaborators in 1968 [15]. The detector consisted of a 615 m³ C₂Cl₄ and was located in the Homestake Gold Mine in Lead, South Dakota, United States. Davis *et al.* used the inverse β decay reaction $^{37}\text{Cl} + \nu_e \rightarrow ^{37}\text{Ar} + e^-$ to detect solar neutrinos and the ratio of the measured rate to the expected rate from the Standard Solar Model [16] was found to be 0.33 ± 0.06 [17]. Subsequently, the 3000 m³ water cherenkov Kamiokande detector was used to observe recoil e^- from $\nu_e e^-$ scattering (1987) [18]. Since the direction and energy could be reconstructed using Cherenkov photons, solar neutrino events could be identified using a direction correlation with the sun. The energy threshold was ~ 7.0 MeV, and ^8B and Hep neutrinos were included in the solar neutrino samples. The ratio of the measured flux to the expected was $0.55^{+0.13}_{-0.11}$ [19]. Gallex and SAGE were radiochemical experiments using Gallium. Solar neutrinos were detected by the inverse β decay interaction $^{71}\text{Ga} + \nu_e \rightarrow ^{71}\text{Ge} + e^-$. Since the energy threshold was low (233 keV), pp neutrinos could be detected. The Gallex detector was located at Gran Sasso Underground Laboratory at a depth of 3,800 meters water equivalent. The target material was 101 tons of GaCl₃ and the ratio of the measured rate to the expected rate was 0.60 ± 0.07 [20].

The SAGE detector is located in a tunnel in the northern Caucasus mountains in southern Russia at a depth of 4700 m.w.e. The target is 50 tons of metallic Ga and the ratio of the measured rate to the expected rate is 0.52 ± 0.07 [21].

All of these solar neutrino experiments found that the detected number of solar neutrino were smaller than expected.

More recently, Super-Kamiokande and SNO have studied the solar neutrino problem. Super-Kamiokande is a 50,000 ton water Cherenkov detector located near the old Kamiokande site. SK observes solar neutrinos via elastic neutrino-electron scattering. The observation of solar neutrinos began in 1996. The SK energy threshold is 5.0 MeV except for at the beginning (6.5 MeV) and the fiducial volume is 22.5 kton. The ratio of the measured flux to the expected is $0.465 \pm 0.005^{+0.014}_{-0.012}$ for a data set corresponding to 1496 days [22].

SNO has studied the flux of high energy solar neutrinos from ^8B decay. This experi-

ment detects neutrinos via the reactions

$$\begin{aligned}\nu + d &\rightarrow e^- + p + p & (CC), \\ \nu + d &\rightarrow \nu + p + n & (NC), \\ \nu + e &\rightarrow \nu + e & (ES).\end{aligned}$$

The charged current deuteron breakup, can be initiated only by a ν_e . Thus, it measures only the ν_e flux $\phi(\nu_e)$. The second reaction, neutral current deuteron breakup, can be initiated with equal cross sections by neutrinos of all active flavors. Thus, it measures $\phi(\nu_e) + \phi(\nu_{\mu,\tau})$, where $\phi(\nu_{\mu,\tau})$ is the flux of ν_μ and/or ν_τ from the Sun. Finally, the third reaction, neutrino electron elastic scattering, can be triggered by a neutrino of any active flavor, but $\sigma(\nu_{\mu,\tau}e \rightarrow \nu_{\mu,\tau}e) \cong \sigma(\nu_e e \rightarrow \nu_e e) / 6.5$. Thus, this reaction measures $\phi(\nu_e) + \phi(\nu_{\mu,\tau}) / 6.5$. From the observed rates, SNO finds that $\phi(\nu_e) = (1.76 \pm 0.10) \times 10^6 \text{ cm}^{-2}\text{s}^{-1}$, and $\phi(\nu_{\mu,\tau}) = (3.41_{-0.64}^{+0.66}) \times 10^6 \text{ cm}^{-2}\text{s}^{-1}$, assuming the standard shape of the ^8B neutrino energy spectrum [23]. $\phi(\nu_{\mu,\tau})$ is 5.3σ deviation from zero. This clearly non-vanishing ν_μ/ν_τ flux from the Sun is convincing evidence that the electron neutrinos produced in the solar core do indeed change flavor.

Combining all solar neutrino experiments, the allowed regions for neutrino oscillation parameters so far are shown in Fig.1.2.

These results suggest that the most likely explanation of the behavior of the solar neutrinos is the LMA solution combined with MSW effect, although the LOW solution remains a possibility at 99.73% C.L..

1.3.2 Atmospheric Neutrinos

Atmospheric neutrinos are created when primary cosmic rays strike the nitrogen and oxygen nuclei in the earth's atmosphere and produce a shower of pions, which subsequently decay via $\pi^\pm \rightarrow \mu^\pm \nu_\mu (\bar{\nu}_\mu)$, $\mu^\pm \rightarrow e^\pm \nu_e \bar{\nu}_\mu (\bar{\nu}_e \nu_\mu)$. The resulting atmospheric neutrinos therefore are expected to follow the ratio $\nu_\mu : \nu_e = 2 : 1$, which is essentially independent of the details of the complicated process that created them. In addition, the direction of the incoming neutrinos relative to the direction of the leptons (e and μ) created by the charged current interactions can be measured and the zenith angle distribution accurately measured.

Four detectors (IMB [25], Soudan 2 [26], Kamiokande [27], Super-Kamiokande [28]) confirmed that the ν_μ/ν_e ratio was noticeably smaller value (about 60% of the expected value) than expected, while Frejus reported results consistent with the expected within errors [29]. The anomalous zenith angle dependence was first observed in Kamiokande, and has now been confirmed, with much better statistical significance, by Super-Kamiokande [30]. The zenith angle distributions of electrons show good agreement with Monte Carlo simulations based on atmospheric neutrino flux calculations. However, there are more significant distortions for muons than expected. In 1998, these results are reported as the

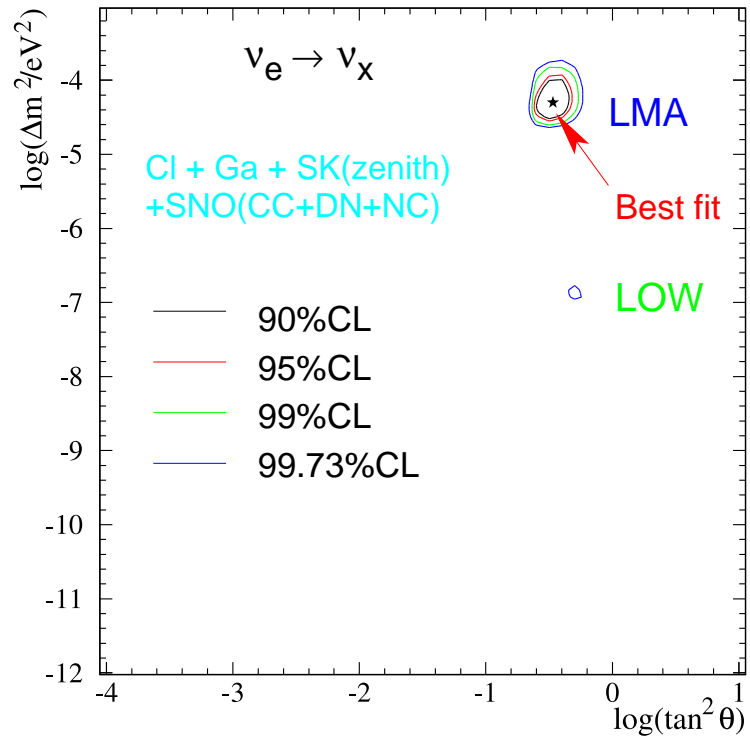


Figure 1.2: Allowed regions of the solar neutrino parameter space after the SNO day and night spectra measurement including flux information from the Homestake, SAGE and Gallex, the day and night spectra from the SK, and solar model predictions [24].

evidence for oscillation of atmospheric neutrinos. Fig.1.3 shows the zenith angle distribution of Sub-GeV single ring e-like events, μ -like events, Multi-GeV single ring e-like events and μ -like events + partially contained events [31]. Black circles indicate the data and the two histograms indicate atmospheric neutrino MC events without neutrino oscillation and best fit oscillated expectation with $\Delta m^2 = 2.5 \times 10^{-3} \text{ eV}^2$ and $\sin^2 2\theta = 1.0$, respectively.

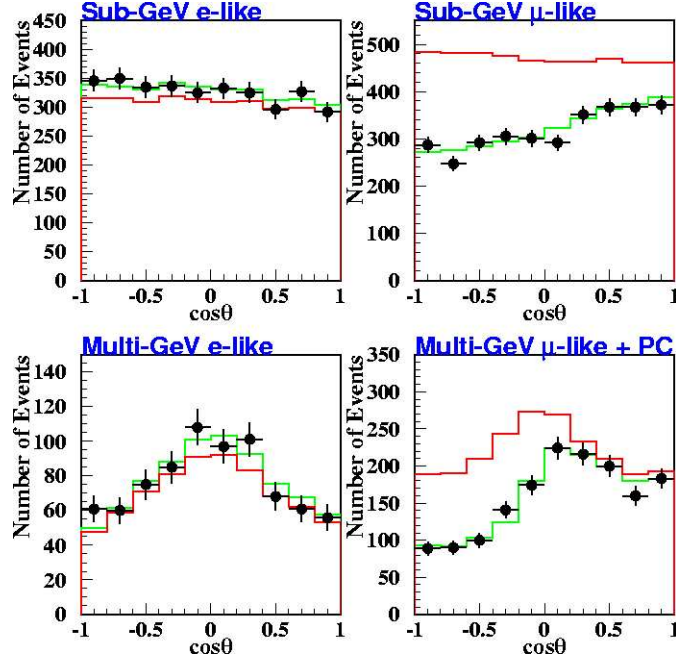


Figure 1.3: Zenith angle distribution of Sub-GeV single ring e-like events, μ -like events, Multi-GeV single ring e-like events and μ -like events + partially contained events at SK. Black circles indicate the data and the two histograms indicate MC events without neutrino oscillation and best fit oscillated expectation with $\Delta m^2 = 2.5 \times 10^{-3} \text{ eV}^2$ and $\sin^2 2\theta = 1.0$, respectively.

The data prefer a mixing angle $\sin^2 2\theta > 0.92$ and $\Delta m^2 \approx 1.6\text{--}3.9 \times 10^{-3} \text{ eV}^2$ in the 90% C.L. range. Because there is no excess e-like appearance signal, $\nu_\mu \leftrightarrow \nu_e$ oscillations are disfavored relative to $\nu_\mu \leftrightarrow \nu_\tau$.

The KEK to Kamioka long-baseline neutrino oscillation experiment (K2K) uses an accelerator-produced neutrino beam with a baseline distance of 250 km to probe the same Δm^2 region as that explored with atmospheric neutrinos. The result supports the oscillation interpretation of the atmospheric neutrino data [32]. K2K reported 56 beam neutrino events observed at the Super-Kamiokande with an expectation of $80.1^{+6.2}_{-5.4}$. This means that the probability that the observed flux at SK is explained by statistical fluctuations alone without neutrino oscillation is less than 1%. The 90% C.L. contour crosses the Δm^2 axis at 1.5 and $3.9 \times 10^{-3} \text{ eV}^2$ for maximal mixing. These results are

consistent with the ranges given by SK.

1.3.3 Reactor Neutrinos

Reactors have also been used as intense $\bar{\nu}_e$ sources. In the fission of ^{235}U , ^{238}U , ^{239}Pu and ^{241}Pu , neutron rich nuclei are produced and $\bar{\nu}_e$'s are subsequently emitted via β decay. The absolute flux of the neutrinos from the reactors is constrained to within a few % uncertainty by the Bugey experiment [33]. Experiments using reactor $\bar{\nu}_e$ s are particularly suitable for low Δm^2 measurement because the mean energy of the reactor $\bar{\nu}_e$ is a few MeV, which is much smaller than that of accelerator neutrinos. The distance from the reactor core to previous reactor experiments ranged from several tens of meters to 1 km and the sensitivity to the Δm^2 was above 10^{-3} eV^2 at $\langle E_\nu \rangle \sim 4 \text{ MeV}$. In table 1.1, the results and the systematic errors of the typical previous reactor experiments are summarized.

Experiment	Distance	Sensitivity (Δm^2)	Result
Bugey	15m,40m,95m	0.01 eV^2	$0.987 \pm 0.014(\text{sys.}) \pm 0.027(\sigma_{V-A})$ [33]
CHOOZ	1km	0.001 eV^2	$1.01 \pm 0.028(\text{sta.}) \pm 0.027(\text{sys.})$ [34]
Palo Verde	750m,2×890m	0.001 eV^2	$1.01 \pm 0.024(\text{sta.}) \pm 0.053(\text{sys.})$ [35]

Table 1.1: The summary of the sensitivities and results of previous reactor experiments.

The overall systematic errors including the $\bar{\nu}_e$ flux uncertainty and detector uncertainty are constrained to within a few % at these experiments. At the Bugey experiment, the experimental systematic error and the theoretical error of the cross section of $\bar{\nu}_e p \rightarrow n + e^+$ reaction are estimated to be 1.4% and 2.7%, respectively. Previous reactor experiments don't obtain any positive oscillation signals, so only the excluded regions from Bugey, CHOOZ and Palo Verde are shown in Fig.1.1.

1.4 Reactor Anti-Neutrino Oscillations at KamLAND

The KamLAND experiment is a very long baseline reactor $\bar{\nu}_e$ oscillation experiment, designed to detect $\bar{\nu}_e$'s coming from reactors, an average distance of 180 km away. There are 54 nuclear power reactors in Japan, supplying one third of the total electric power in the country.

Fig.1.4 shows the locations of the Japanese commercial reactors and KamLAND, and Table.1.2 contains various information about Japanese and Korean reactors.

The contribution to the $\bar{\nu}_e$ flux from Korean reactors is estimated to be $2.46 \pm 0.25\%$. Other reactors around the world contribute an average $0.7 \pm 0.35\%$ which is estimated using reactor specifications from the International Nuclear Safety Center [43]. Although

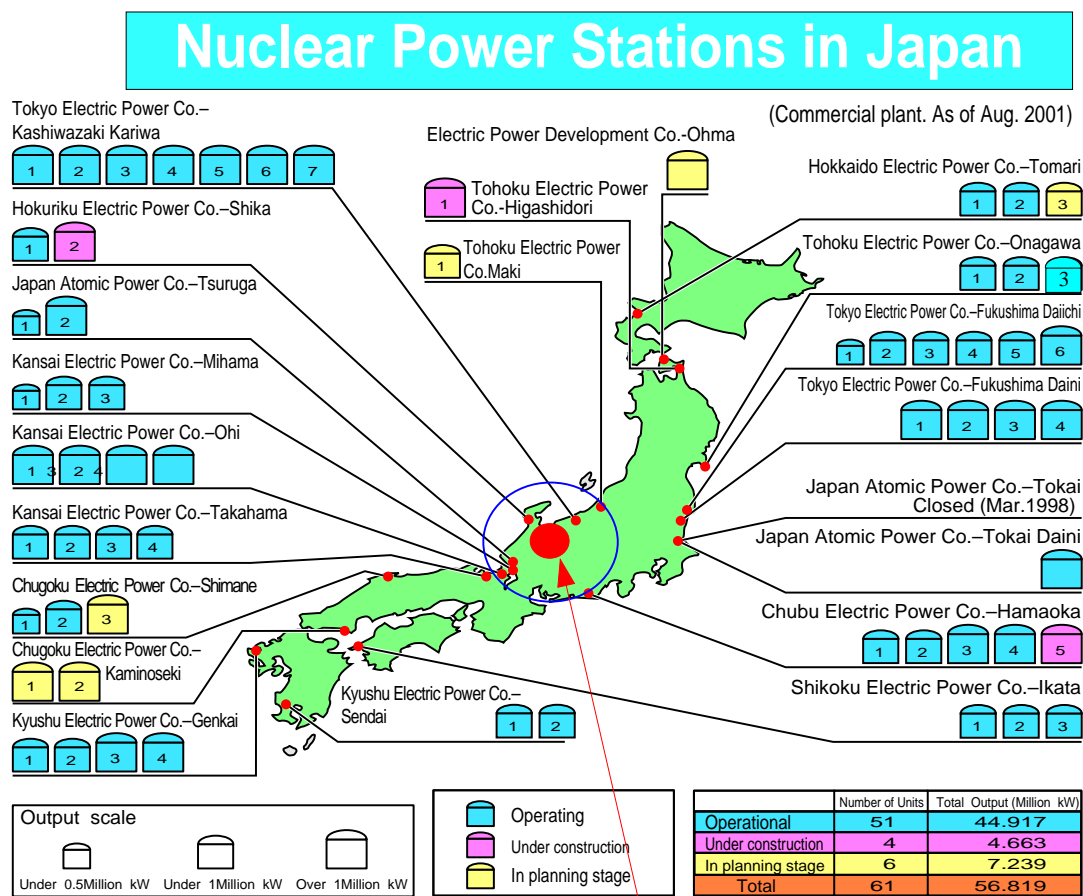


Figure 1.4: The locations of the Japanese commercial reactors and KamLAND.

Reactor Name	Thermal Power (GW)	Number of cores	distance (km)	power flux (GW/cm^2)	contribution (%)
Japan					
Kashiwazaki	24.5	7	160	7.62×10^{-15}	30.9
Ohi	13.7	4	179	3.40×10^{-15}	13.8
Takahama	10.2	4	191	2.22×10^{-15}	9.0
Shika	1.9	1	88	1.95×10^{-15}	7.9
Tsuruga	4.5	2	138	1.88×10^{-15}	7.6
Hamaoka	10.6	4	214	1.84×10^{-15}	7.5
Mihama	4.9	3	146	1.83×10^{-15}	7.4
Fukushima1	14.2	6	349	0.93×10^{-15}	3.8
Fukushima2	13.2	4	351	0.85×10^{-15}	3.5
Tokai2	3.3	1	295	0.30×10^{-15}	1.2
Shimane	3.8	2	401	0.19×10^{-15}	0.8
Onagawa	4.1	3	431	0.18×10^{-15}	0.7
Ikata	6.0	3	561	0.15×10^{-15}	0.6
Genkai	6.7	4	754	0.094×10^{-15}	0.4
Sendai	5.3	2	830	0.061×10^{-15}	0.2
Tomari	3.3	2	783	0.043×10^{-15}	0.2
Fugen	0.5	1	138	0.21×10^{-15}	0.9
Monju	0.8	1	141	0.32×10^{-15}	1.3
Korea					
Kori	9.5	4	735	0.14×10^{-15}	0.6
Wolsong	8.4	4	709	0.13×10^{-15}	0.5
Yonggwang	14.9	5	986	0.12×10^{-15}	0.5
Ulchin	11.8	4	712	0.19×10^{-15}	0.8
Total	176.1	71		2.4×10^{-14}	100

Table 1.2: Thermal power, number of cores, distance, and thermal power flux at KamLAND from Japanese and Korean reactors.

the anti-neutrino flux at the KamLAND site is due to many nuclear reactors at a range of distances, the $\bar{\nu}_e$ flux is actually dominated by a few reactors at an average distance of ~ 180 km. More than 79 % of the computed flux arises from 26 reactors within the distance range 138-214 km. One reactor at 88 km contributes an additional 6.7 % to the flux and the other reactors are more than 295 km away. This relatively narrow band of distances implies that, for some oscillation parameters, KamLAND can observe a distortion of the $\bar{\nu}_e$ energy spectrum.

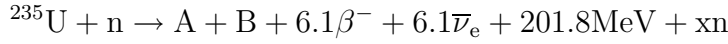
Since the efficiency of reactor operation is about 80%, the total thermal power flux at KamLAND is estimated to be 1.9×10^{-14} GW/cm². The neutrino flux at KamLAND can be calculated approximately as,

$$\text{Total Neutrino Flux at KamLAND} = \frac{\text{Number of Neutrinos/Fission} \times \text{GW/cm}^2}{\text{Release Energy(MeV)/Fission}}$$

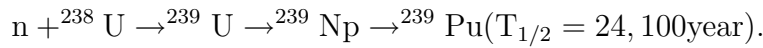
Using a mean energy release per fission of about 200 MeV and the number of neutrino per fission of about 6, the total neutrino flux at KamLAND is estimated to be 3.6×10^6 /cm²/s.

The calculation of the $\bar{\nu}_e$ flux from reactors and its energy spectra were checked by a number of previous experiments to a few percent level precision.

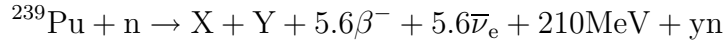
²³⁵U in the reactor core absorbs thermal neutrons and breaks up into several pieces. The $\bar{\nu}_e$ s are emitted as the result of the β decay of these fission fragments.



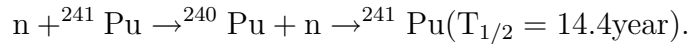
²³⁸U absorbs fast neutrons and breaks up into fragments or produces the ²³⁹Pu via two β decays after capturing a thermal neutron,



The ²³⁹Pu can then absorb thermal neutrons and can become yet another fission energy source.



Alternatively, the ²³⁹Pu can capture two thermal neutrons consecutively to produce ²⁴¹Pu in the following way,



The ²⁴¹Pu produced via the above reaction can also be a fission energy source.

The energy released by these four different fission sources are summarized in Table.1.3 [38].

In the reactor core, these reactions occur continuously and in parallel. Accordingly, the fuel composition in the reactor core has a time variation, called the 'burn-up' effect.

Isotope	Energy release [MeV / fission]
^{235}U	201.8 ± 0.5
^{238}U	205.0 ± 0.7
^{239}Pu	210.3 ± 0.6
^{241}Pu	212.6 ± 0.7

Table 1.3: Energy release per fission [38].

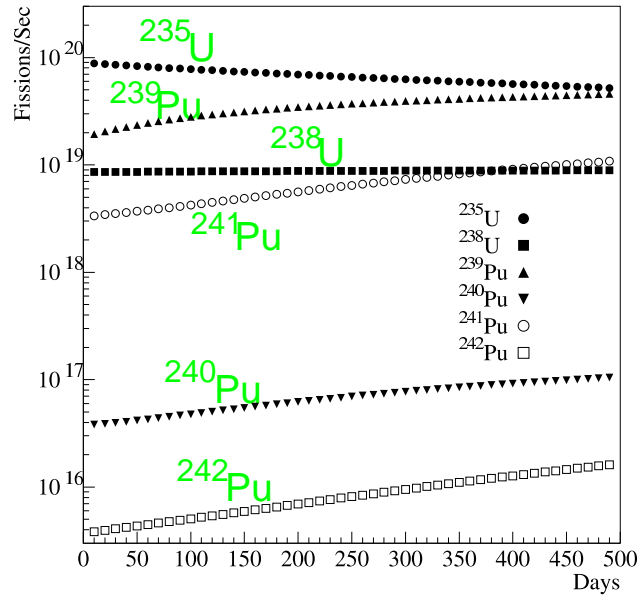
Figure 1.5: Example of the fuel burn-up at a Palo Verde Reactor. From top to bottom, ^{235}U , ^{239}Pu , ^{238}U and ^{241}Pu fission rates are plotted in turn.

Fig.1.5 shows an example of the burn-up effect calculated at the Palo Verde Reactor [39]. As can be seen, ^{235}U and ^{238}U are decreased and ^{239}Pu and ^{241}Pu are increased as a function of time. The contributions of ^{240}Pu and ^{241}Pu are less than 0.1%. Palo Verde group reported the uncertainty in the $\bar{\nu}_e$ flux from that of fission rates was less than 1% by direct measurements of isotopic abundances of four fission nuclei after being burned through several fuel cycles.

In KamLAND, the thermal power and the burn-up data of each reactor are provided by the appropriate Japanese electric power company. And the reactor type such as pressurized or boiling water reactors, volume ratio and the enrichment of the new (replaced) fuel, and the initial mean burn-up informations are also provided. Using a simple model of the reactor core developed by TEPCO SYSTEMS Co.,Ltd. and TOHOKU Univ., the number of fissions per unit time of each isotope, ^{235}U , ^{238}U , ^{239}Pu and ^{241}Pu at each Japanese reactor can be calculated. The uncertainty for $\bar{\nu}_e$ flux is estimated to be 1% compared with detailed simulation by TEPCO SYSTEMS. The thermal power data is needed to normalize the fission rates and this value is monitored at each reactor and controlled within 2% error.

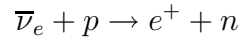
An example of the calculated fission rates at one reactor are shown in Fig.1.6. It can be seen that the main contribution to the fission rate comes from ^{235}U and the fission rate of each fission isotope changes as a function of time.

The neutrino energy spectra from the different isotopes also differ. For all but ^{238}U , direct measurements of the β spectrum from fission of each isotope exists [41]. These data were converted to neutrino spectra by fitting the observed beta spectra to a set of 30 hypothetical beta-branches. The neutrino spectrum of ^{238}U has not been measured due to the high energy of neutrons needed to cause it to fission, and so the calculated spectrum was used for this analysis [42].

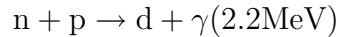
Fig.1.7 shows the neutrino spectrum from four isotopes per fission per MeV. For ^{235}U , ^{239}Pu and ^{241}Pu , the data from the direct measurement of the β decay of these fission fragments are used, and for ^{238}U , the calculated spectra are used.

The width of each spectrum means the systematic error associated with the measurement of β spectrum and the conversion error from β spectrum into $\bar{\nu}_e$'s.

At KamLAND, a $\bar{\nu}_e$ flux of 3.6×10^6 /cm²/s incident from reactors is detected using the inverse β decay reaction,



The positron annihilation constitutes a prompt signal and the final state neutron is quickly thermalized and captured by a proton, producing a 2.2 MeV γ .



This reaction typically happens 210 μ after the prompt signal and so the 2.2 MeV γ -ray signal constitutes a delayed signal. By requiring particular timing and space correlations between the two signals, backgrounds are highly suppressed. The event rates of 3 events/day/kton is expected without neutrino oscillation.

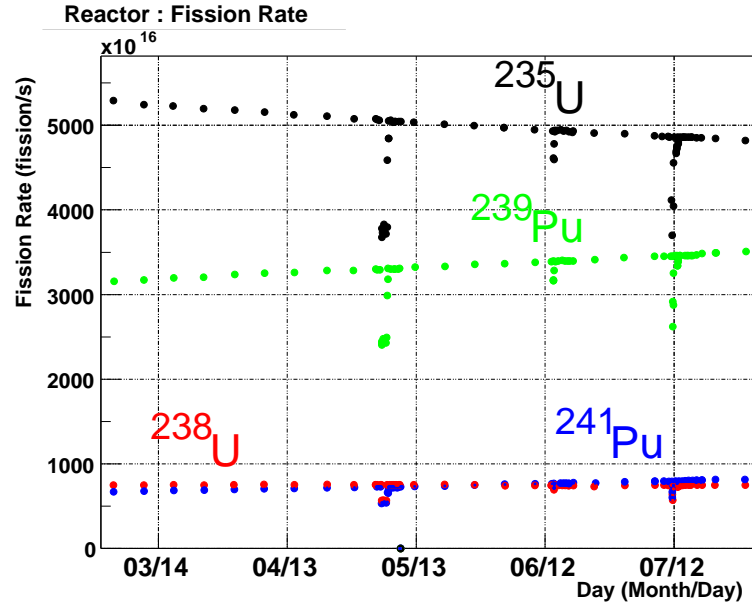


Figure 1.6: Example of the fuel burn-up at a Japanese reactor. From top to bottom, ^{235}U , ^{239}Pu , ^{238}U and ^{241}Pu fission rates are plotted in turn.

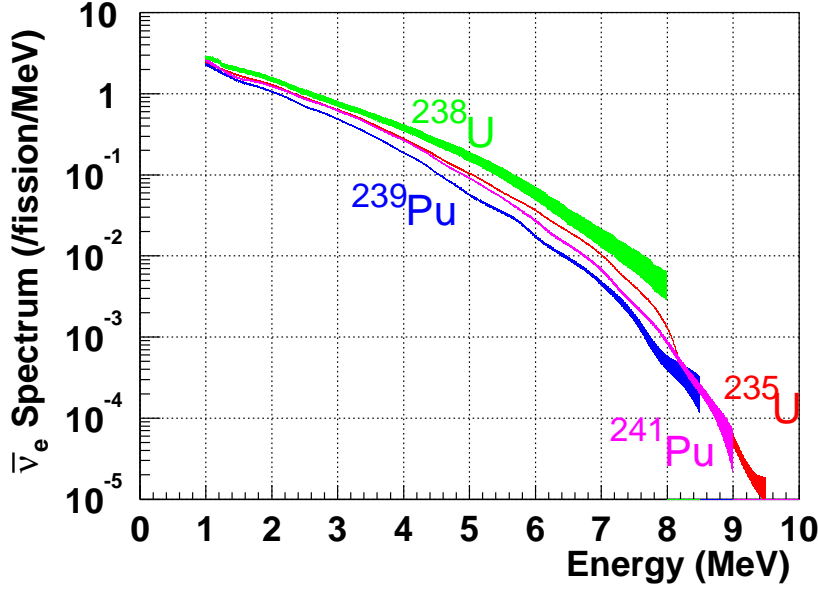


Figure 1.7: Neutrino spectrum from four isotopes.

When neutrino oscillation phenomena are taken into account, the expected $\bar{\nu}_e$ spectrum, $N(E_\nu)$ is,

$$N(E_\nu) = \int dE_\nu \sigma(E_\nu) N_p f_\nu(E_\nu) \sum_i \frac{P_i(E_\nu)}{4\pi d_i^2} \left(1 - \sin^2 2\theta \sin^2 \frac{\Delta m^2 d_i}{4E_\nu} \right)$$

where E_ν is the neutrino energy, d_i and $P_i(E_\nu)$ are the baseline and the total fission number of the reactor i , respectively. $f_\nu(E_\nu)$ is the neutrino energy spectrum per unit fission, $\sigma(E_\nu)$ is the inverse β decay cross section, and N_p is the number of target protons. The expected energy spectrum of the $\bar{\nu}_e$ as a function of the visible energy for the prompt signal is shown in Fig.1.8.

The livetime of this estimation is 145.1 day, the space and timing correlation is $dR < 160\text{cm}$ and $0.5\mu\text{sec} < dT < 660\mu\text{sec}$, and the fiducial volume is set to be 408.5 ton. Two peaks below 2.6 MeV are terrestrial anti-neutrinos coming from the ^{238}U and ^{232}Th β decay in the earth. The peak at higher energy region is from ^{238}U and lower peak contains both from ^{238}U and ^{232}Th . The terrestrial anti-neutrino has never been measured yet. Although to detect the terrestrial anti-neutrino is one of the main purposes at KamLAND, 2.6 MeV threshold is used for this analysis to avoid the ambiguity of terrestrial anti-neutrino flux. The background spectrum is also shown assuming that the $^{238}\text{U}/^{232}\text{Th}$ contents in the liquid scintillator are 10^{-14} g/g and the ^{40}K content is 10^{-15} g/g. These numbers correspond to the requirements for the KamLAND liquid scintillator purity. In

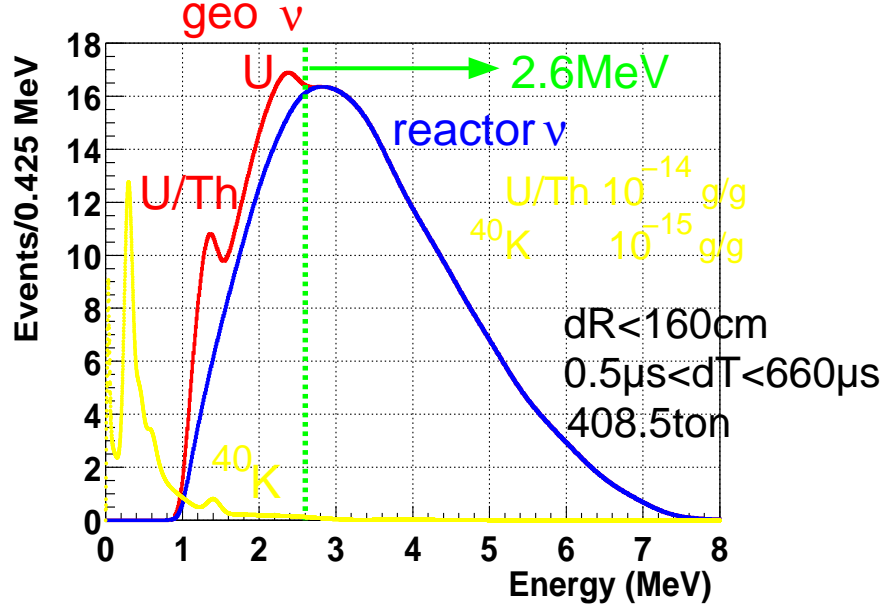


Figure 1.8: Expected energy spectrum of $\bar{\nu}_e$ at KamLAND. Expected geo- $\bar{\nu}_e$ and background spectrum are also shown.

total, 86.8 reactor $\bar{\nu}_e$ events are expected to detect at KamLAND during 145.1 day. 0.04 geo- $\bar{\nu}_e$ events are expected and this number is considered to be uncertainty for the reactor $\bar{\nu}_e$.

The mean $\bar{\nu}_e$ energy detected at KamLAND is about 4 MeV and KamLAND can achieve an unprecedented sensitivity down below $\Delta m^2 \leq 10^{-5} \text{ eV}^2$. The expected sensitivity of KamLAND is shown in Fig.1.9. This sensitivity exceeds that of today's most sensitive reactor experiments by more than two orders of magnitude. This sensitivity to Δm^2 is good enough for KamLAND to be the first direct test of the LMA MSW solution to the solar neutrino problem.

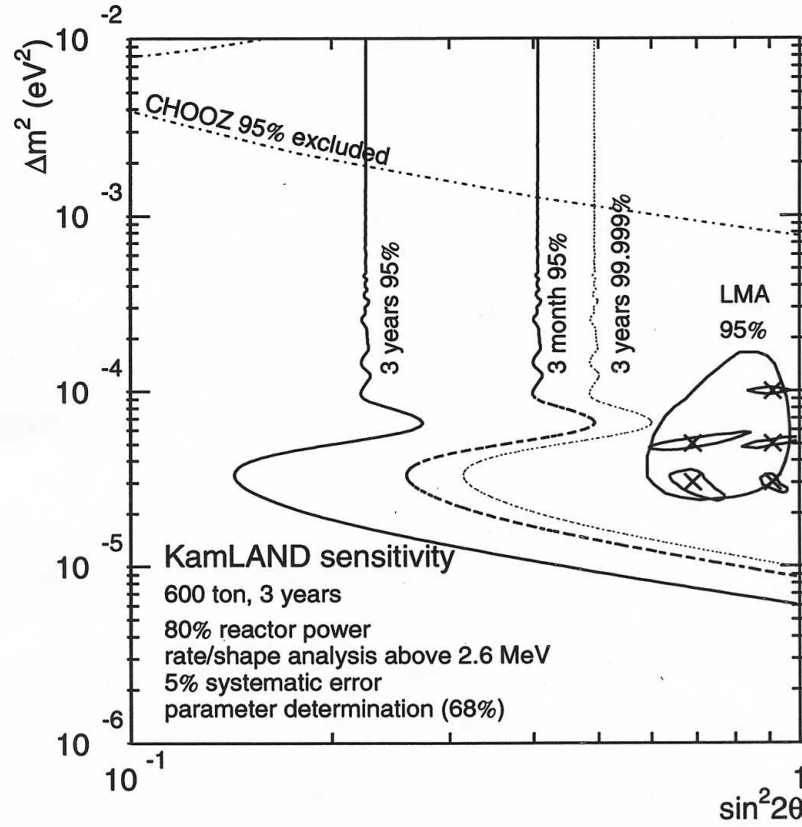


Figure 1.9: Sensitivity of KamLAND. The 3 vertical regions are expected exclusion limits in case there is no oscillation. The small islands in the LMA region are 1σ allowed regions if oscillation parameters are at the cross points.

Chapter 2

Detector

The detection method and each component of the KamLAND detector are described in detail in this chapter. The KamLAND detector uses liquid scintillator to detect anti-neutrino events with accurate energy resolution, and the total volume of the inner detector is 1200m³ optimized to detect reactor neutrinos from Japanese commercial reactors(~ 180 km) with high statistics.

2.1 Detection Method

The inverse β -decay reaction,

$$\bar{\nu}_e + p \rightarrow e^+ + n$$

is utilized to detect $\bar{\nu}_e$'s with energies above 1.8 MeV in liquid scintillator. The neutron emitted by that reaction is thermalized in the liquid scintillator repeatedly elastic scattering from protons and after about 200 μ seconds, is captured by proton. 2.2 MeV γ -ray is then emitted from the final state, deuteron. The detection of the e^+ and the 2.2 MeV γ -ray from neutron captured on a proton in delayed coincidence is a powerful tool for reducing background.

In the limit where the nucleon mass is taken to be infinite, i.e., the zeroth order in $1/M$, the positron energy is [36]

$$E_e^{(0)} = E_\nu - \Delta,$$

where $\Delta = M_n - M_p$. At each order in $1/M$, the positron momentum $p_e = \sqrt{E_e^2 - m_e^2}$ and the velocity $v_e = p_e/E_e$ are defined. The differential cross section at zeroth order is

$$\left(\frac{d\sigma}{d\cos\theta} \right)^{(0)} = \frac{\sigma_0}{2} [(f^2 + 3g^2) + (f^2 - g^2)v_e^{(0)}\cos\theta] E_e^{(0)} p_e^{(0)}.$$

where $f = 1.0$ is the vector coupling constant and $g = 1.267$ is the axial-vector coupling constant.

The normalizing constant σ_0 , including the energy-independent inner radiative correction, is

$$\sigma_0 = \frac{G_F^2 \cos^2 \theta_C}{\pi} (1 + \Delta_{inner}^R),$$

where $\Delta_{inner}^R \simeq 0.024$. This gives the standard result for the total cross section,

$$\begin{aligned} \sigma^{(0)tot} &= \sigma_0 (f^2 + 3g^2) E_e^{(0)} p_e^{(0)} \\ &= 0.0952 \left(\frac{E_e^{(0)} p_e^{(0)}}{1 \text{ MeV}^2} \right) \times 10^{-42} \text{ cm}^2. \end{aligned}$$

The energy-independent inner radiative corrections affect the neutron beta decay rate in the same way, and hence the total cross section can be written

$$\sigma_{tot}^{(0)} = \frac{2\pi^2 / m_e^5}{f_{p.s.}^R \tau_n} E_e^{(0)} p_e^{(0)},$$

where τ_n is the measured neutron lifetime and $f_{p.s.}^R = 1.7152$ is the phase space factor, including Coulomb weak magnetism, recoil, and outer radiative corrections, but not inner radiative corrections.

At first order in $1/M$, the positron energy depends on the scattering angle and is written

$$E_e^{(1)} = E_e^{(0)} \left[1 - \frac{E_\nu}{M} (1 - v_e^{(0)} \cos \theta) \right] - \frac{y^2}{M},$$

where $y^2 = (\Delta^2 - m_e^2) / 2$. In factors of the form $1/M$, the average nucleon mass is used; Using $1/M$ rather than $1/M_p$ leads to a negligible difference of $O(1/M^2)$. The differential cross section at that order is

$$\left(\frac{d\sigma}{d\cos\theta} \right)^{(1)} = \frac{\sigma_0}{2} [(f^2 + 3g^2 + (f^2 - g^2)v_e^{(1)} \cos \theta) E_e^{(1)} p_e^{(1)} - \frac{\sigma_0}{2} \left[\frac{\Gamma}{M} \right] E_e^{(0)} p_e^{(0)}],$$

where

$$\begin{aligned} \Gamma &= 2(f + f_2)g \left[(2E_e^{(0)} + \Delta)(1 - v_e^{(0)} \cos \theta) - \frac{m_e^2}{E_e^{(0)}} \right] \\ &+ (f^2 + g^2)g \left[\Delta(1 + v_e^{(0)} \cos \theta) + \frac{m_e^2}{E_e^{(0)}} \right] \\ &+ (f^2 + 3g^2) \left[(E_e^{(0)} + \Delta)(1 - \frac{1}{v_e^{(0)}} \cos \theta) - \Delta \right] \\ &+ (f^2 - g^2) \left[(E_e^{(0)} + \Delta)(1 - \frac{1}{v_e^{(0)}} \cos \theta) - \Delta \right] v_e^{(0)} \cos \theta. \end{aligned}$$

The small energy-dependent outer radiative corrections to $\langle \cos \theta \rangle$ are from Ref. [37].

The energy threshold of the $\bar{\nu}_e$ in this reaction is calculated in the laboratory frame (where the proton is at rest) ,

$$E_{\nu}^{thr.} = \frac{(M_n + m_e)^2 - M_p^2}{2M_p} = 1.806 MeV.$$

The total cross section result as a function of the neutrino energy is shown in Fig.2.1.

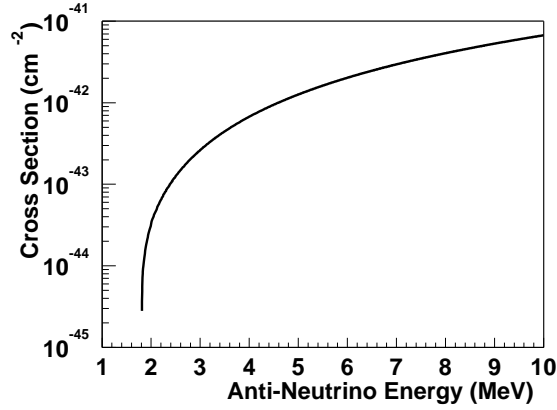


Figure 2.1: Total cross section of the reaction, $\bar{\nu}_e + p \rightarrow n + e^+$, as a function of the $\bar{\nu}_e$ energy.

2.2 Site

KamLAND is a liquid scintillator detector located at the former site of Kamiokande in the Kamioka mine in Gifu Prefecture, Japan. The average rock overburden above KamLAND is 2700 meter water equivalent. A schematic view of the detector is given in Fig.2.2.

2.3 Design

The detector consists of a series of concentric spherical shells, the detailed structure of which is shown in Fig2.3. The primary detector target consists of 1000 tons of ultra pure liquid scintillator located at the center of the detector. Surrounding the scintillator is ~ 2.5 m thick ultra pure paraffin oil buffer. Separating these two regions is a $135 \mu\text{m}$ thick transparent nylon/EVOH (Ethylene vinyl alcohol copolymer) plastic sphere(~ 6.5 m). The balloon can not, by itself, support the mass of the scintillator, but supports the small difference of densities of the two fluids. The balloon is supported and constrained by a network of kevlar ropes. The liquid scintillator is 80 % dodecane, 20 %

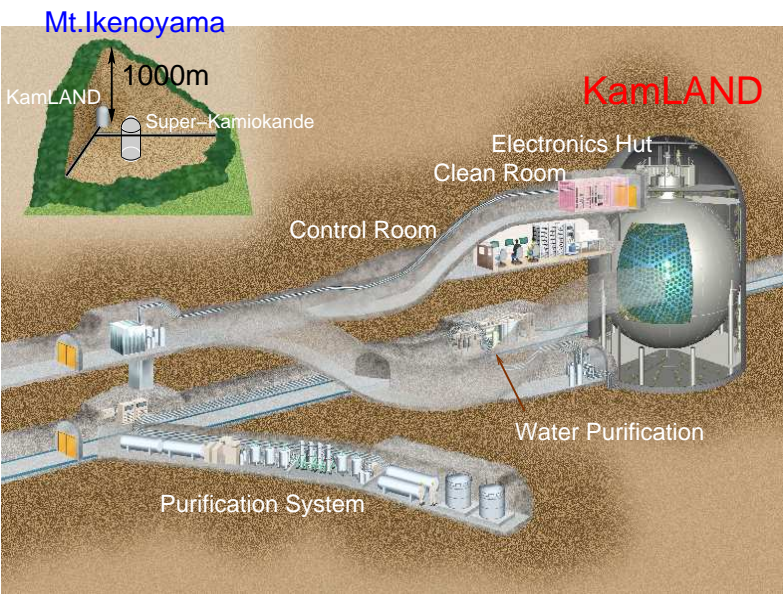


Figure 2.2: Schematic view of the KamLAND detector

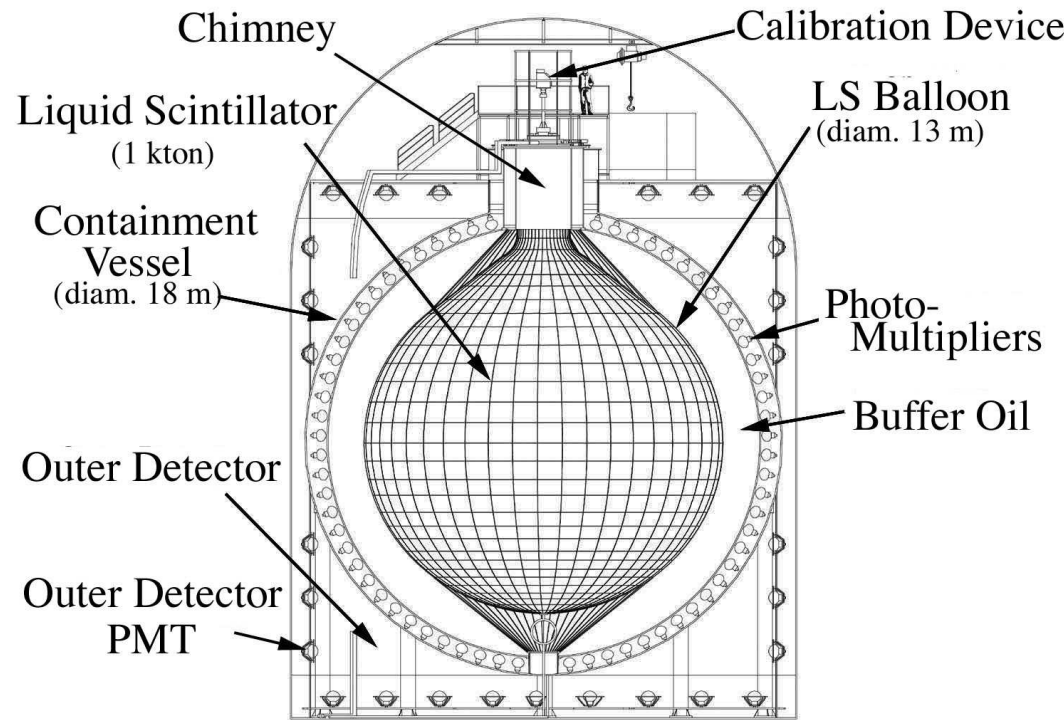


Figure 2.3: detail of the KamLAND detector

pseudocumene(1,2,4-Trimethylbenzene), and 1.52 g/little of PPO(2,5-Diphenyloxazole). A buffer oil of dodecane and isoparaffin oils shields the liquid scintillator from external radiation. The scintillator is viewed by an array of 1,879 photomultiplier tubes(PMTs) supported on a 9 m radius stainless steel spherical vessel. This array includes 1,325 specially developed fast PMTs with 17-inch diameter photocathodes, and 554 older Kamiokande 20-inch PMTs. While the total photo-cathode coverage is 34%, only 17-inch PMTs are used for this analysis, corresponding to 22 % coverage. A 3mm thick acrylic barrier at 16.6 m diameter helps to prevent radon emanating from the PMT glass from entering the LS. The containment vessel is surrounded by a 3.2 kton water-Cherenkov detector with 225 20-inch PMTs. This outer detector (OD) absorbs γ -rays and neutrons from surrounding rock and is a tagging device for cosmic-ray muons. Access to the central volume is provided by a concentric chimney structure from the upper experimental deck, which is used to install some calibration sources. The outer water shield is instrumented and serves as a cosmic-ray veto detector.

2.4 Balloon

The central balloon, a very thin flexible membrane, is a critical component of the detector that isolates the liquid scintillator from the external buffer oil. Its material must be selected to be low radio-activity, transparent to light in the 350 to 500 nm wavelength range, chemically compatible with both the buffer oil and liquid scintillator, impermeable to radon gas, and stable enough for its properties to remain adequate for the lifetime of the detector. The multi-layer sandwich structure, EVOH/Nylon/EVOH, is adopted to satisfy these requirements which thickness is 135 μm . The Nylon provides strength and the EVOH provides very low gas permeability.

The weight of the target volume balloon and its contents must be supported by the detector stainless steel vessel. The kevlar straps of the balloon net connected to the top of the detector fulfill this function. There are 44 load cells for each rope to balance and to monitor all tensions.

The transparency to light of the balloon is shown in the Fig.2.4.

That figure shows that our balloon has a transparency of more than 90 % in the 370 to 500 nm wavelength range and the typical transparency at wavelength 400 nm is 96%.

2.5 PMTs

To optimize the photon collection efficiency and physics reconstruction accuracy, KamLAND uses 1,325 specially developed photomultipliers (R7250) with 17-inch-diameter photocathodes and 554 20-inch PMTs (R3602) manufactured in large quantities for Super-Kamiokande experiment by Hamamatsu. The schematic views of the 17-inch and 20-inch PMTs are shown in Fig.2.5.

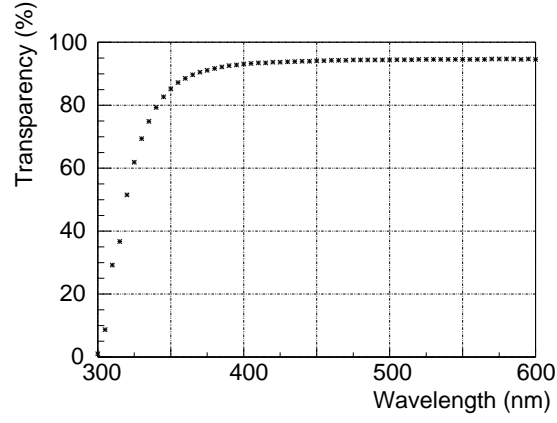


Figure 2.4: Transparency to light of the KamLAND balloon.

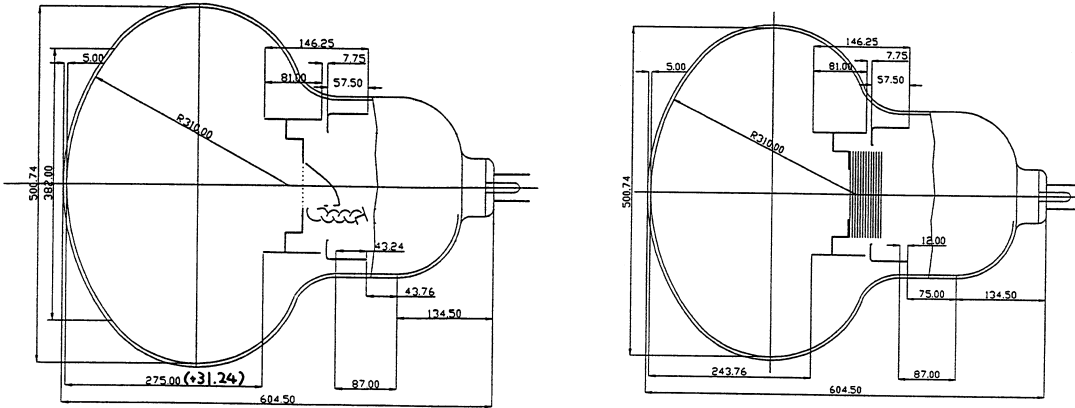


Figure 2.5: Schematic view of the 17-inch and 20-inch PMTs.

To significantly improve on the transit time spread (TTS) in the timing signals over the 20-inch tube, the photocathode is masked down to the equivalent acceptance of a 17-inch PMT. By reducing the photon acceptance to the central 17 inches of the front face and by introducing fast linear focusing in place of the older and intrinsically slower venetian-blind multiplier section, the TTS is reduced from ~ 10 ns to the order of 3ns. Transit time is typically about 110 ns for 17-inch PMT and about 90 ns for 20-inch PMT. The peak to valley (P/V) ratio of the PMT is also measured using the 1 photo-electron pulse height distribution. This value is defined by the peak height of 1 photo-electron divided by the minimum height where the noise level and the 1 photo-electron level cross. The measured P/V ratio is about 3.3. This performance is much improved compared with the 20-inch PMT. The P/V ratio is about 1.7, and additionally, 2 photo-electron peaks are identified by 17-inch PMT.

The quantum efficiency of the 17-inch PMT is shown in the Fig.2.6. The typical value of the quantum efficiency is about 22 % from approximately 350 nm to 400 nm. To improve photon statistics and the energy resolution, the maximum range of the quantum efficiency must be matched with the emission spectrum of the liquid scintillator.

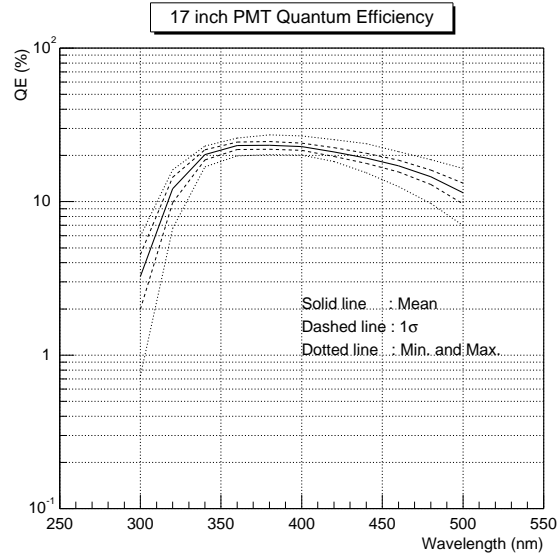


Figure 2.6: The quantum efficiency of KamLAND PMTs.

To improve the photon statistics and the energy resolution further, KamLAND also has 554 20-inch PMTs. While total photo-cathode coverage is 34%, only the 17-inch PMTs, corresponding to 22% coverage, are used in this analysis.

2.6 Liquid Scintillator and Buffer Oil

The liquid scintillator in the center of the detector is the main component of KamLAND. To detect reactor anti-neutrinos with energy as low as 1 MeV, the detector must have excellent light output, optical transparency, large volume (to improve statistics) and contain the low level of radio-active isotopes. Liquid scintillator suits these requirements and paraffin-oil based liquid scintillator with good optical transparency is used. KamLAND has chosen to use a scintillator of simple and well proven formulation consisting of pseudocumene as the primary solvent and with PPO as the primary fluor. The concentration of 80% dodecane, 20% pseudocumene, and 1.52 g/little PPO was chosen to optimize the light output and transparency.

The emission spectrum of the liquid scintillator is shown in the Fig.2.7. The peak

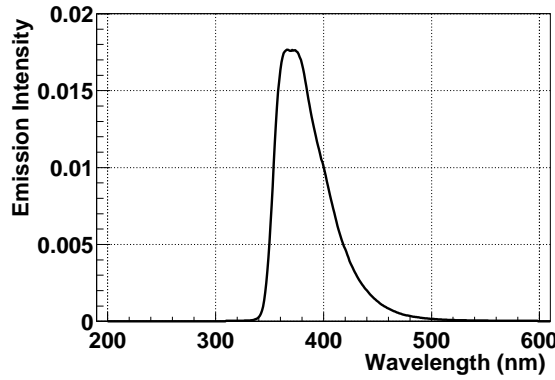


Figure 2.7: Emission spectrum of the liquid scintillator.

position is around 370 nm matching the maximum range of the PMT quantum efficiency. Accordingly, there is no need for a secondary fluor such as Bis-MSB as a wavelength shifter. The specific gravity of the liquid scintillator is 0.77754g/cm^3 at 15°C . The attenuation length of the liquid scintillator is about 10 m at 400 nm and the light output is 57% Anthracene.

The main purpose of the buffer oil surrounding the liquid scintillator is to reduce the background γ 's from the detector materials like stainless tank and PMTs or the rock surrounding the detector. Since the buffer oil doesn't contain such a fluor as PPO, few scintillation lights are emitted for the events occurred at the buffer region. And also, it is known by chemical compatibility measurements that the liquid scintillator, mainly pseudocumene, attacks the detector materials, PMT potting materials, PMT signal and high voltage cables and acrylic plate etc. Pure paraffin oils are used for the buffer oil to secure the detector materials. As the optical transparency is needed for this buffer oil, the mixture of dodecane and isoparaffin, both transparencies of which are 30 m at

400 nm wavelength, was used. To make the difference in specific gravity between liquid scintillator and buffer oil small and to reduce the load on the balloon, the specific gravity of the buffer oil was tuned to be 0.04% less than that of the LS.

The refractive index of each component as a function of the wavelength of incident photons was measured. Fig.2.8 shows the results of the refractive index measurement for the liquid scintillator, paraffin oil, nylon, and acrylic plate. Circles indicate the measured

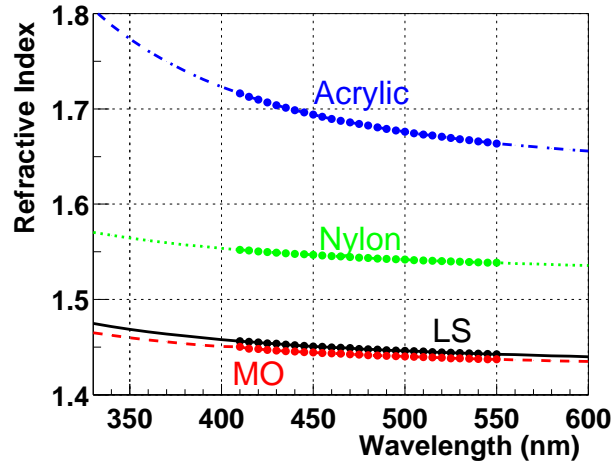


Figure 2.8: The refractive index of the detector components.

data and the lines indicate the fitted functions, which is defined as $F(\lambda) = a + b/\lambda^2 + c/\lambda^4$, where $F(\lambda)$ is a refractive index, λ is a wavelength of a photon, and a, b , and c are free parameters. At wavelength 400nm, the refractive indexes of LS, MO, Nylon, and Acrylic are 1.458, 1.450, 1.554, and 1.723, respectively.

To reduce the radio-active isotopes further, a purification system was developed. It is explained in the next section.

2.7 Purification System

The typical event rate of reactor anti-neutrinos is around 1 event/day. The KamLAND detector uses so-called “delayed coincidence” technique to identify $\bar{\nu}_e$ events. Accidental backgrounds from radioactive nuclei may become intolerable if sufficient rejection is not achieved. To reduce these background event rates < 0.1 event/day, the concentrations of ^{238}U , ^{232}Th in the liquid scintillator must be $< 10^{-14}$ g/g and that of ^{40}K must be $< 10^{-15}$ g/g. The intrinsic radioactive impurities of ^{238}U , ^{232}Th in the liquid scintillator was measured to be 10^{-13} g/g or less, and so, it was necessary to purify it further. Fig.2.9 shows a schematic view of the KamLAND purification system. To reduce radioactive

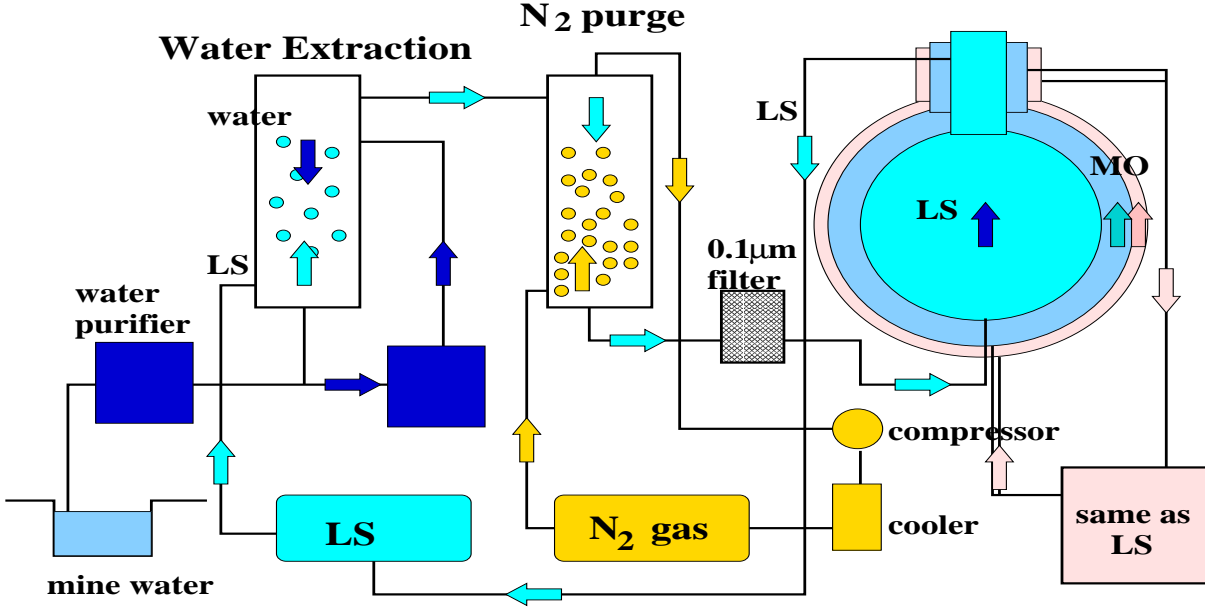


Figure 2.9: Schematic view of the KamLAND purification system.

contaminations to the required level, a water extraction technique combined with nitrogen gas purging are used. In water extraction, the liquid scintillator is mixed with purified water. Since ionic species of metal atoms have higher solubility in water a many orders of magnitude than that of hydrocarbon molecules, radioactive elements such as ^{238}U , ^{232}Th and ^{40}K are preferably removed. The N_2 gas purging removes the small amount of dissolved water in the liquid scintillator from the water extraction process as well as the radon (^{222}Rn), which is highly abundant in the mine environment and may constitute a serious background. It also removes the dissolved O_2 in the liquid scintillator which degrades the light output of the liquid scintillator through oxygen quenching. In addition, $0.1\text{ }\mu\text{m}$ filtration is used to remove dust and other macroscopic contaminants.

2.8 Front-End Electronics

Fig.2.10 shows a 12-channel KamLAND Front-End Electronics board, and Fig.2.11 is a schematic diagram.

In the KamLAND Front-End Electronics, a PMT signal is discriminated by a threshold of $1/3$ p.e. to provide the total number of hit tubes for event triggering. The threshold of the event trigger is ~ 0.75 MeV for the global (prompt) trigger, while the delayed trigger with ~ 0.4 MeV threshold is issued only in a period of 1 ms after each prompt trigger. Each PMT pulse is then amplified by three different gains, 20 times, 4 times and



Figure 2.10: 12-channel KamLAND Front-End Electronics board.

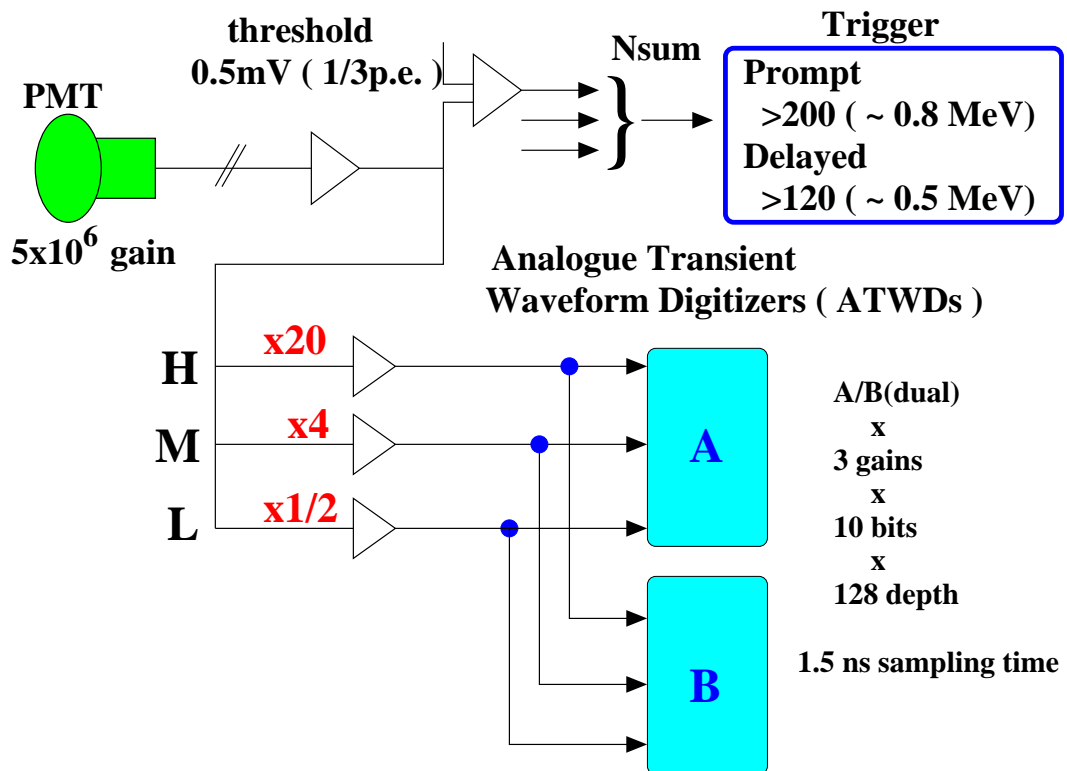


Figure 2.11: Schematic diagram of a KamLAND Front-End Electronics board.

0.5 times. As a result, the electronics have a large dynamic range, and can detect PMT pulses from a single photo-electron to thousands. This allow us to measure high energy muons as well as low energy neutrino candidates.

The pulse shapes are digitized by Analogue Transient Waveform Digitizers (ATWD) with 128 samples in 1.5 ns steps. Two identical ATWDs are available to each PMT channel to make the system practically deadtime-less.

The KamLAND electronics return at most 6 waveforms per each PMT, that is, high, middle and low gain data for both of two independent channel, A and B. The waveforms from the PMTs are digitized in a window of about 200 ns. Normally, the high gain channel is used. If the waveforms of high gain are saturated by large pulse, the AD conversion of middle gain waveforms are started and data are sent to the DAQ. If the middle gain is also saturated, the low gain data is sent. If channel A is filled with the waveform data and another hit occurs, channel B is used to reduce dead time.

2.9 Trigger

The trigger issues a 5 bit trigger command to the Front-End Electronics. All triggers are based on the 4 bit nsum received from each FEE board. Nsum is defined as the number of PMTs connected to that board whose signal level went above the discriminator level. The different triggers can be enabled or disabled for the various situations. The basic triggers for normal physics data taking are the ID prompt trigger and delayed trigger. The prompt trigger is based on the total ID nsum being above the ID prompt trigger threshold of 200. It issues a global acquisition trigger to the ID FEE boards and opens a 1 ms window for the delayed trigger. The delayed trigger is based on the total ID nsum being above the delayed trigger threshold 120 during this window. The ID prescale trigger only issues a global trigger to the ID FEE boards for a fraction of each second. This is useful for the high rate data acquisition mode such as source calibration. The OD is separated into four regions, top, upper side, lower side and bottom. These regions have nsum thresholds of 6, 5, 6 and 7, respectively. If there are 48 events with total ID nsum above 772 in 0.84 seconds, a supernova trigger is issued to the DAQ. It puts the trigger into a predefined data acquisition state for 3 minutes to prevent DAQ hang up because of high event rates from the supernova. The 1 pps trigger is based on the GPS 1 pps signal. A GPS trigger is issued at the start of run and every 32 seconds thereafter. The history trigger is based on the total ID nsum being above the ID history trigger threshold 120 and is issued every 25ns while above threshold up to a maximum of 200 ns. It doesn't issue any external triggers and these history data don't contain waveform information, only information about the number of hits.

2.10 Veto Counter

A 3.2 kton water-Cherenkov detector with 225 20-inch PMTs surrounds the stainless steel containment vessel. The purpose of this is to actively veto cosmic-ray muons, and to absorb γ -rays and neutrons from the surrounding rock. Reflective Tyvek sheets cover its surfaces and are used to divide the outer detector into 4 regions for increased light collection efficiency and for increased tracking capability with regional information.

2.11 Water Purification

There are two main purposes for the water purification. One is to provide pure water to the outer detector, and the other is to supply the water extraction tower of the purification system. Based on the experiences of the Kamiokande and Super-Kamiokande experiments, a system consisting of a reverse osmosis (RO) device, ion-exchanger, ultraviolet sterilization, vacuum degasser, cartridge polisher and ultra-fine membranes were constructed. The system can supply purified water with ^{238}U and ^{238}Th concentrations of 10^{-13} g/g level with a rate of a few thousand liters per hour.

2.12 Calibration System

A variety of radioactive, LED and LASER sources are deployed in KamLAND to calibrate the detector's response to different types of events. A Z-axis deployment system is currently utilized in KamLAND for detector calibration. It allows for the deployment of various sources along the z-axis of the detector by attaching a source to a cable which is then lowered into the detector via a remotely controlled motor. The position of the source inside the detector is given by the electronic readout of a shaft encoder positioned at the top pulley of the system assembly. The deployment assembly is encased within a sealed glovebox. It is accessible through gloveports which allow the attachment of sources, and through an airlock system used to load and remove sources. The glovebox is purged with Nitrogen gas prior to access to the detector region.

Chapter 3

Event Reconstruction

The event reconstruction algorithms used for the reactor anti-neutrino analysis are described in this chapter. The KamLAND data acquisition system returns the waveforms of all PMTs which detected photoelectrons. First, a waveform analysis method to extract charge and timing information is described in section 3.1. The second step is vertex reconstruction, which mainly makes use of the timing information of each PMT, described in section 3.2. The various source calibration data are used for vertex tuning. To estimate the total systematic uncertainty to determine fiducial volume, the spallation neutron samples with isotropic vertex distribution in the detector are used. After vertex reconstruction, effective charges are reconstructed using source calibration data. This effective charges are converted into visible energies by using 2.2 MeV γ -ray data from captured neutrons made by muon spallation reactions. The energy reconstruction and the systematic errors are discussed in section 3.3. The estimation of trigger efficiencies for both prompt and delayed trigger can be found in section 3.4. Muon track reconstruction is described in the last section.

3.1 Waveform Analysis

3.1.1 Raw Data

Fig.3.1 shows two different examples of raw waveforms. The left-hand side is a typical small signal example. High gain waveform is only sent to data acquisition system because middle and low gain waveforms are not obtained if the high gain waveform is not saturated. The right-hand side is a typical example with large pulse signal. It contains three waveforms from high, middle and low gain from bottom to up. Since the waveforms of high and middle gain are saturated, those of all three gains are sent. Most of all events contains only the waveform of high gain. Horizontal axis shows the timing information. One bucket corresponds to 1.5 ns and there are 128 buckets, that is, total sampling time for one signal per one channel is about 200 ns. Vertical axis shows the charge information

and one ATWD count corresponds to 0.00405 pico Coulomb. Each waveform has a different pedestal. After pedestal subtraction, hit timing and charge deposited in the PMT are extracted from the waveform information.

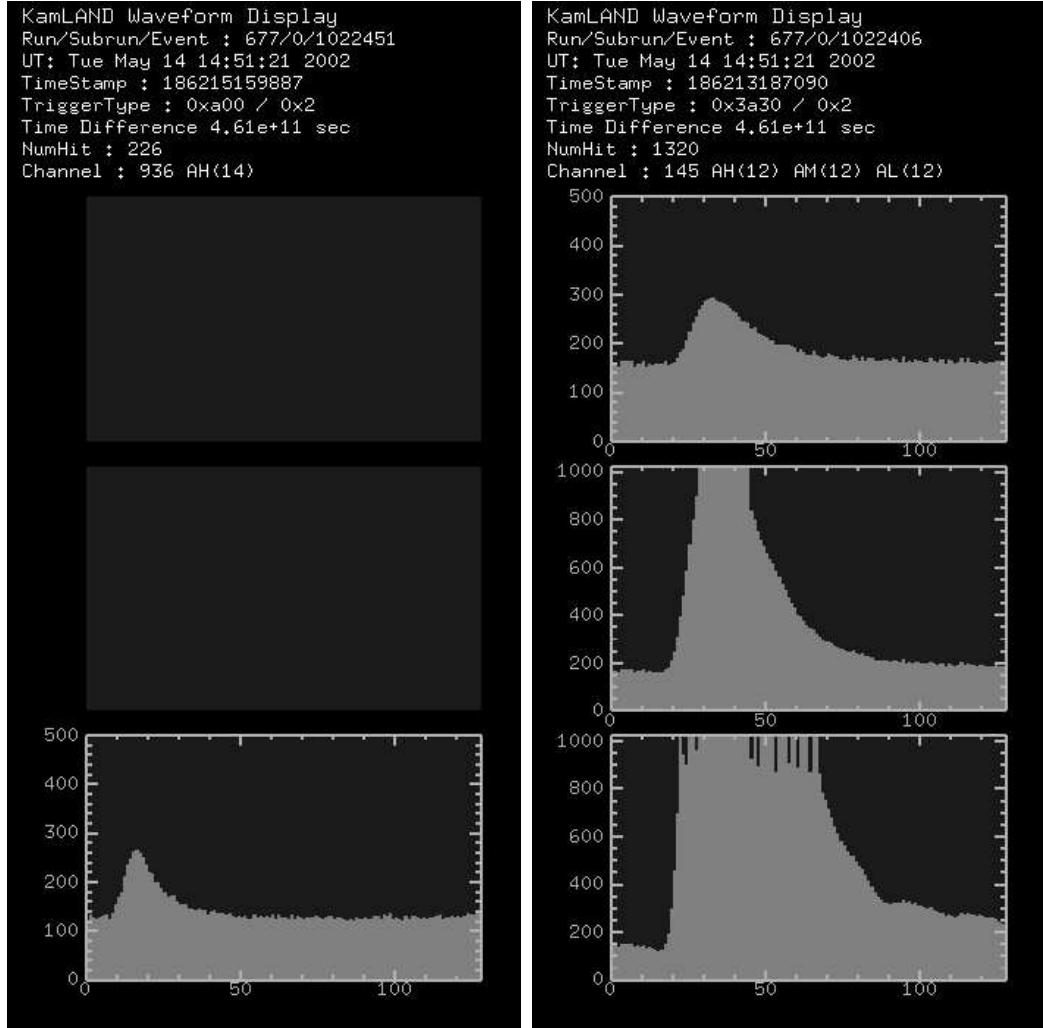


Figure 3.1: Two different examples of raw waveforms. The left side shows only waveforms with the high gain, and right side shows waveforms with high, middle and low gain from bottom to up.

3.1.2 Pedestal Subtraction

Each ATWD contains data even when there is no signal, which is called pedestal. To extract pure amplitude, the pedestal data must be subtracted. In ATWD, the charges

are stored by 128 capacitances first, and then, the corresponding voltages are converted to digital data. The capacities of 128 capacitances are not identical and have some fluctuations. The pedestal subtraction is needed also to correct these fluctuations. Pedestal data are taken at the beginning of each run. When pedestal data are taken, triggers are randomly acquire empty waveforms. These data contain a few accidental hits, and so, because the dark hit rate of each PMT is about 40 kHz, the average number of PMT hits in a 200 ns window is about 11. To estimate the pedestal value, 50 samples of the pedestal data except for the waveform which contains electronics noise or accidental hits are averaged.

Fig.3.2 shows examples of the mean pedestal values. The four histograms in each figure show the pedestal values for different runs, and the six figures show the pedestal values for different channels, A and B and at different gains, high, middle and low. After pedestal data are subtracted, the remaining constant baseline shift is fit event by event, and removed.

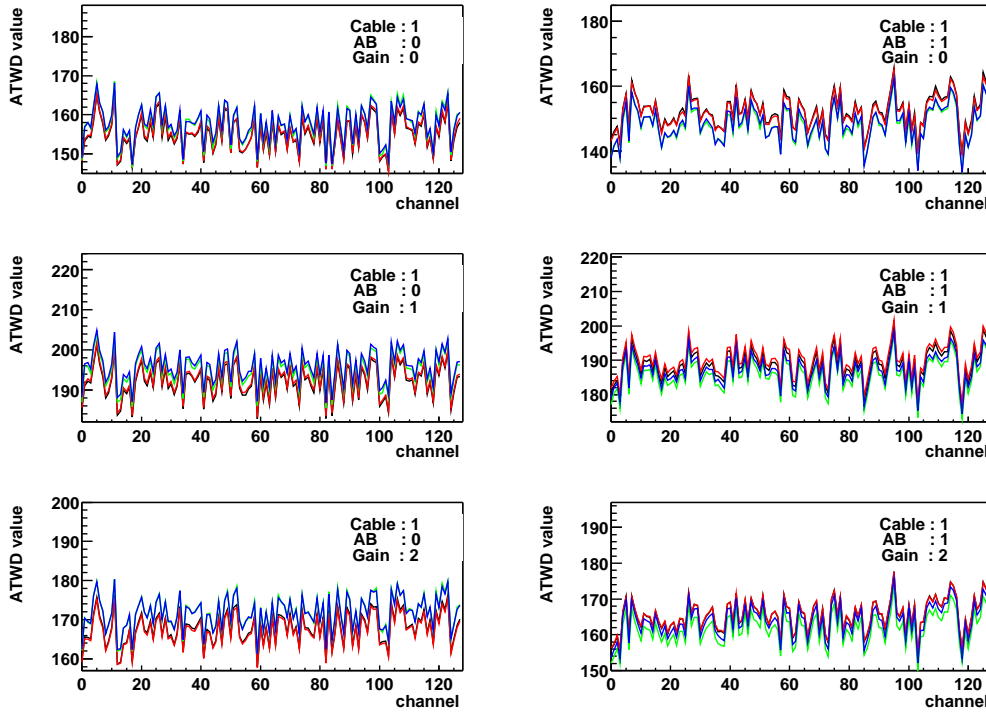


Figure 3.2: Examples of mean pedestal values of a PMT. $AB = 0,1$ means A,B channel, and $Gain = 0,1,2$ means high, middle or low gain. Each figure contains the pedestal values of four different runs.

3.1.3 TQ Fit

Fig.3.3 shows how to extract timing and charge information of the waveform. The left-hand figure shows a PMT waveform only with high gain, and right-hand figure shows waveforms with high, middle and low gain. The line at the peak position is the reconstructed peak position, the line before the peak position is the leading edge time, and the line after peak position is the trailing edge time. The timing information is defined as the leading edge time. The charge is obtained by the sum of the ATWD channel number from the leading edge to trailing edge. Multi-photon information is also fit by the same method and the time and the charge information are extracted similarly.

After all, KamLAND event display is shown in Fig.3.4. PMTs which detect photo-electrons is colored and the difference of colors corresponds to that of the fitted timing. Inner detector is shown in the center of the figure and outer detector in the right upper region. For example, this event doesn't contain OD data. Charge distribution is shown at the left bottom region, and timing distribution is at the right bottom region. These reconstructed timing and charge information is made use of by the vertex fit or the energy fit.

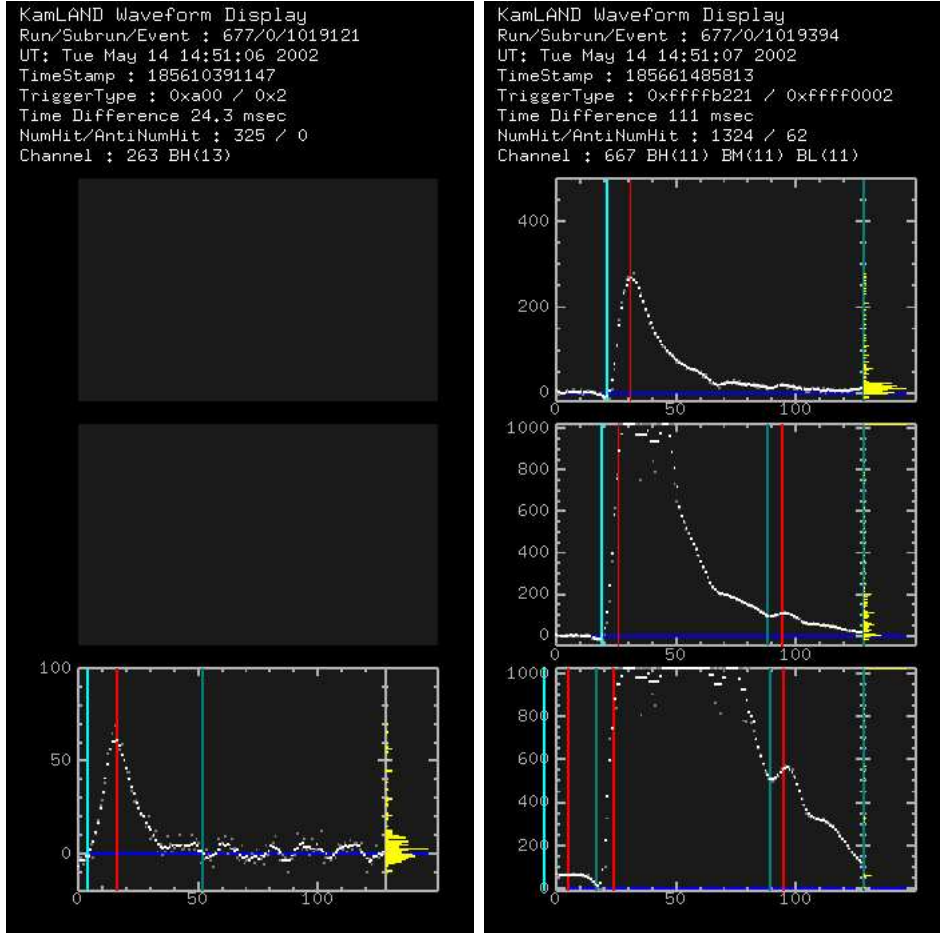


Figure 3.3: Two different examples of waveforms. Pedestal are already subtracted and the baseline is adjusted. Time and charge information are extracted from the fitting results. The left-hand side shows a small charge sample, and right-hand side shows a large charge sample. The line at the peak position is the reconstructed peak position and the line before peak position is the leading edge time and after peak position is the trailing edge time.

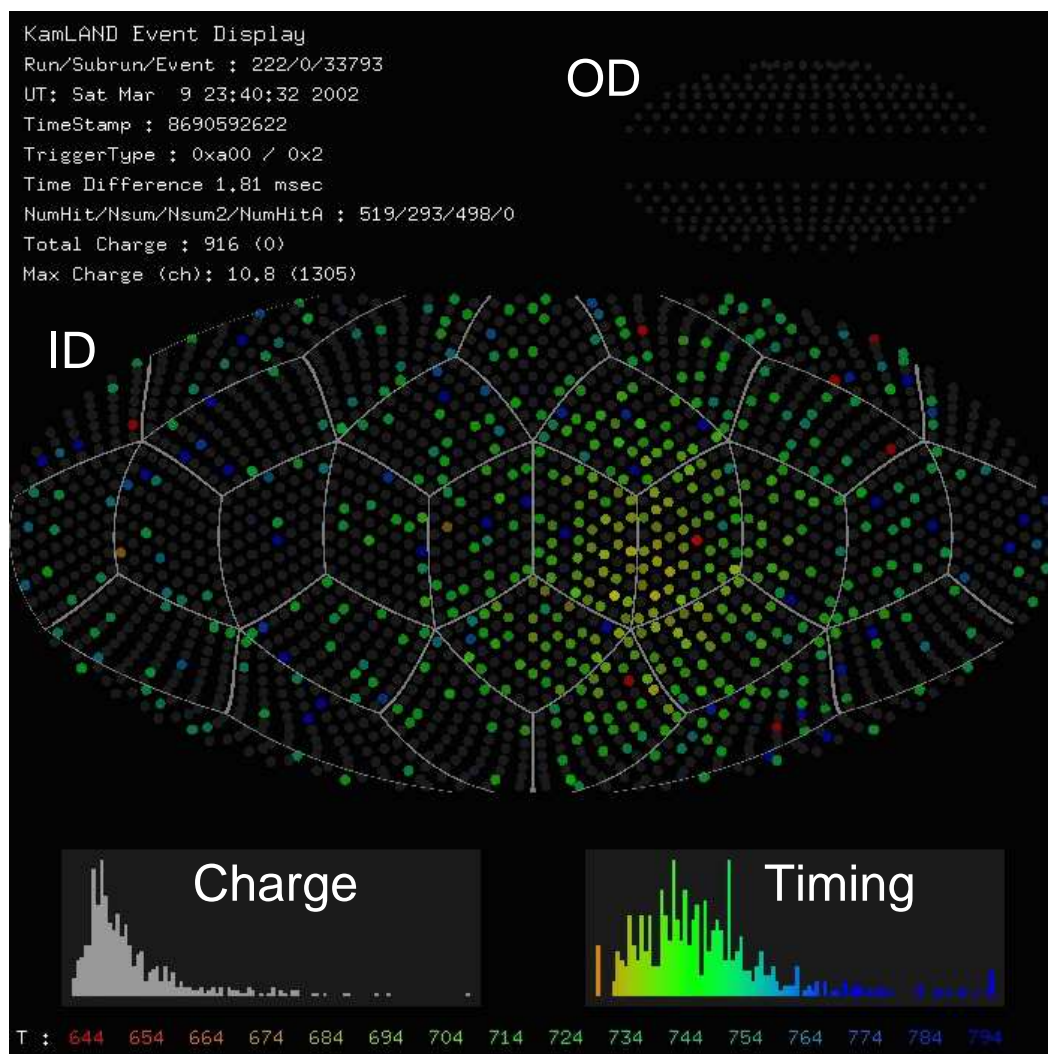


Figure 3.4: KamLAND event display.

3.2 Vertex Fitter

The vertex fitting program is essential to retrieve the correct vertex for each event. The algorithm makes use of time of flight of the scintillation light and absolute position is tuned by radioactive sources, deployed on various z position. The fitter incorporates the effect of the effective speed of lights as a function of the radius. Fig.3.5 shows the relationship between the effective speed of light and the source position along the Z coordinate. Effective speed of light for every Z coordinate is measured from the data of radioactive source calibration runs.

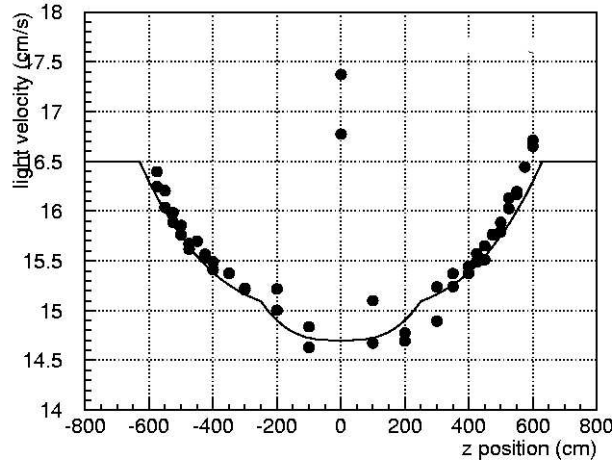


Figure 3.5: Measured effective speed of light as a function of z position.

This dependence is supposed to be caused by non uniformity of number of p.e. of each PMT. At the center of z axis, the effective speed of light can take any values because the distance from PMTs to the vertex position is identical. The line indicates parameters used in reconstructing the vertex which connect the measured points.

Using R dependent speed of light, the time of flight of each photon is subtracted at a supposed vertex. The vertex is moved little by little until the timing spectrum becomes sharp enough. The TOF subtracted timing spectrum is shown in Fig.3.6 for the starting vertex (the origin) and the reconstructed vertex.

The performance of the fitter is checked by the source calibration data along the z axis. Fig.3.7 shows the reconstructed vertex distribution at different z positions with ^{60}Co source. Reconstructed vertex resolution at each position is about 25 cm, and the discrepancy between the reconstruction position and the source deployed position is within ± 5 cm.

The performance of the fitter is shown in Fig.3.8. Data points represent all calibration data. Solid circles indicate ^{60}Co data, solid squares indicate ^{65}Zn , solid triangles are ^{68}Ge ,

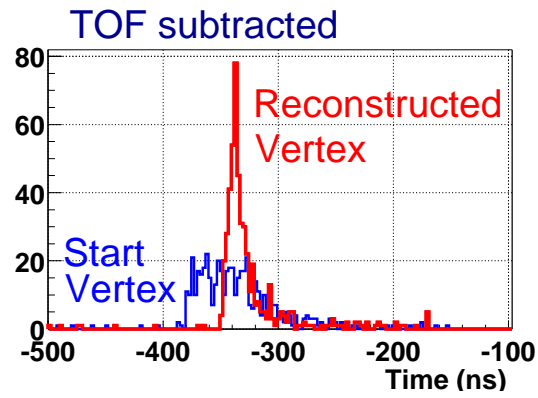


Figure 3.6: Timing histogram at the beginning and the final of the vertex reconstruction.

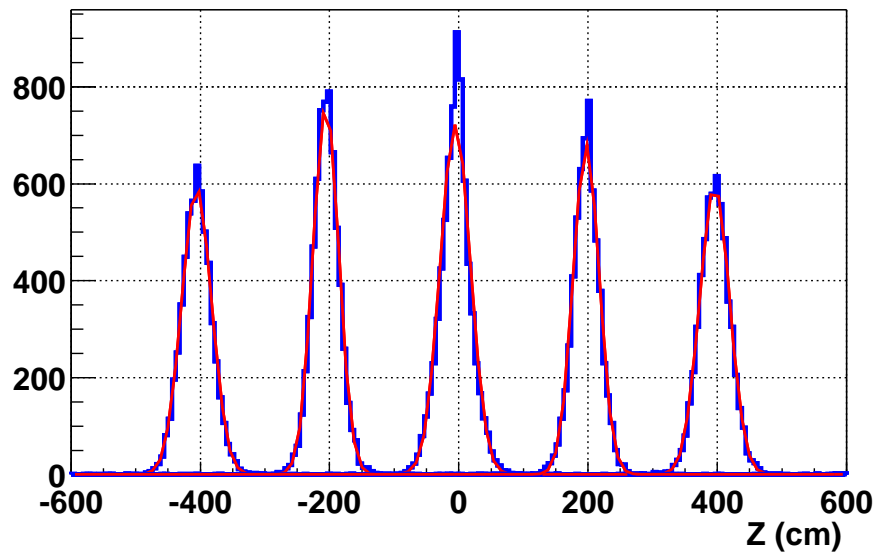


Figure 3.7: Vertex reconstructions at different positions along the z axis.

open circles Am/Be 2.2 MeV, open squares Am/Be 4.4 MeV, and open triangles represent Am/Be 7.6 MeV.

The fiducial volume is defined such that $R \leq 5$ m. At $R = 5$ m, the difference between the reconstructed position and deployed position is less than 5 cm, corresponding to a 3% systematic uncertainty on the fiducial volume for physics analysis.

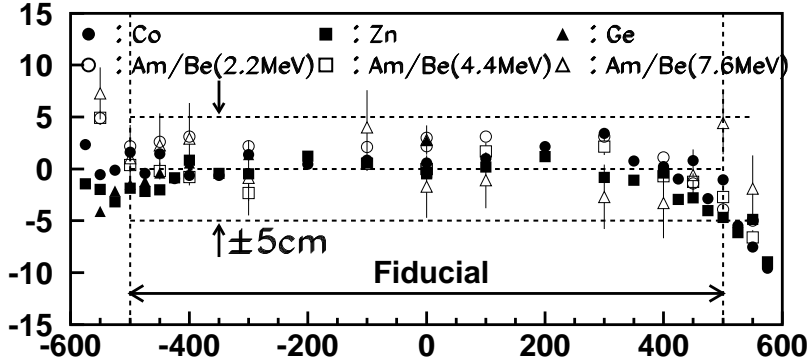


Figure 3.8: Vertex fitter performance along the z-axis. These points are obtained from calibration data. All reconstructed positions within the fiducial $R \leq 5$ m are within 5 cm of the deployed position.

This result is checked using the R^3 distribution of the spallation neutron events with the time window 0.8 ms to 2 ms after muons. Other selection criteria for spallation neutrons are that the energy must be between 1.8 MeV and 2.6 MeV, and the Hits/NsumMax quantity must be greater than one, where NsumMax indicates the maximum hit number of all PMTs from trigger, and Hits indicates the number of PMTs which contain the waveform data. Some of ATWD data just after muons are lost due to hardware issues, ATWD overshooting and undershooting after large pulses, which cause ATWD unstable baseline. Compared the number of ATWD waveforms (Hits) with the number of hit PMTs from trigger (NsumMax), it can be found that there are missing channels or not whether Hits are less than NsumMax. Setting this time window and Hits/NsumMax > 1, the effect of the missing channel is small. Accidental backgrounds are subtracted by using events from a different time window (2 ms to 3.2 ms).

Fig.3.9 shows the R distribution of the spallation neutron sample. The vertex position in R^3 is normalized to the balloon radius. The fiducial R position is also shown by the dotted line.

The total volume of the KamLAND liquid scintillator is measured to be 1171.12 ± 25.00 m³ and the fiducial volume is 523.6 m³. The expected volume ratio of fiducial to total is 0.447. On the other hand, the detected event ratio in the fiducial volume to the total volume is 4501 events / 10219 events = 0.4404 ± 0.0078 . The detected event ratio / volume ratio minus 1 is then -1.48 ± 2.58 %. This discrepancy is considered to

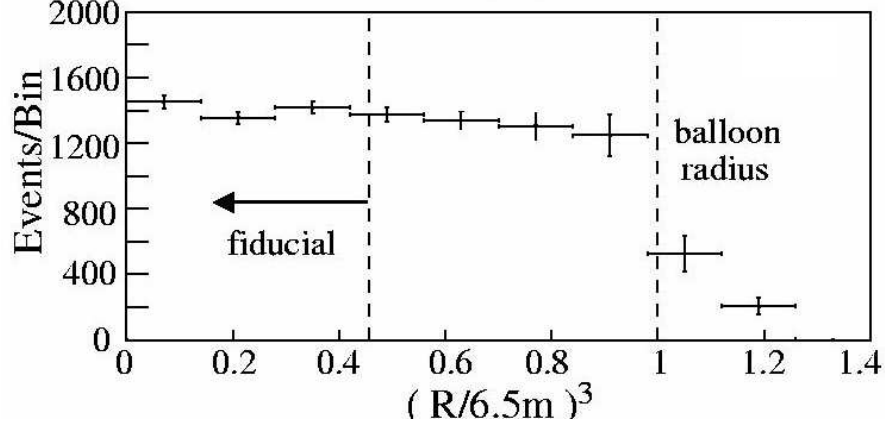


Figure 3.9: The vertex position of the spallation neutron samples as the function of R^3 . The positions of the fiducial volume and the balloon radius are also shown. The R^3 distribution becomes flat if there is not bias on the position reconstruction.

be systematic uncertainty and the error is estimated conservatively to be 4.06 %. Total volume uncertainty is 2.1 %, so the fiducial volume uncertainty is summarized to be 4.6 %.

To check unknown bias of the vertex fitter and to confirm applicability of position calibration along z axis to other axis, the vertex distribution of the spallation neutrons within the fiducial as a function of $\cos\theta$ was studied, where θ is zenith angle, which is defined as the angle between z axis and R. The result is shown in Fig.3.10.

$\cos\theta$ is defined to be the zenith angle, and data with $\cos\theta = \pm 1$ correspond to the z direction. These data points agree within $\pm 3\%$ and no systematic biases in $\cos\theta$ are found. As a result, calibration data along the z-axis are found to be applicable for the to the whole detector region.

3.3 Energy Fitter

3.3.1 Gain Correction

It is found from the time stability check of Co/Zn source calibration and normal data that the overall signal gain including PMT and electronics slightly changes with time. This variation is caused by ATWD hardware changes, high voltage changes, and temperature change in the electronics. This gain variation is corrected for run by run by using single photo-electron charge distributions from normal data. Single photo-electron events are selected with the following conditions.

- A 2ms post-muon cut (vetoed for 2 msec after muon)

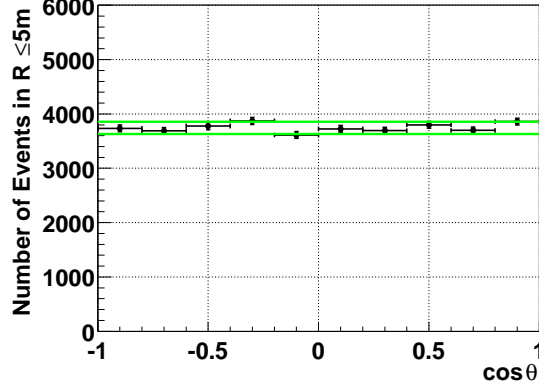


Figure 3.10: The vertex position of the spallation neutron samples as a function of the $\cos\theta$.

- Noise cut
- Nsum (the Number of PMT hits from trigger) is between 120 through 180
- Distance from the event position to the PMT > 600 cm
- one pulse per PMT

These cuts remove large pulse signals and noisy signals, and can select a clean single photo-electron signal from low energy background events.

Fig.3.11 shows the overall PMT gain stability as a function of run number. As seen in this figure, the gain increases by about 4% from run 200 to 1400 during ~ 6 month period.

The dip around run 1200 coincides with some electronics tests. For a long run, with a run time longer than 20,000 sec, the gain is corrected by that run's, and for short runs, the gain is corrected by data from the nearest long run.

3.3.2 Energy Fitter

The energy fitting algorithm is based on the charge distribution of an event. The absolute energy scale is calibrated by the source data. To get the stable energy scale over the entire run time, the gains are corrected run by run and bad PMTs are masked off. The number of bad PMTs as a function of run number is shown in Fig.3.12. The number of bad PMTs decreased after run number 800 because the incorrect PMT cable connections to the high voltage and ATWD boards were fixed. Currently the number of bad PMTs is stable at around 5.

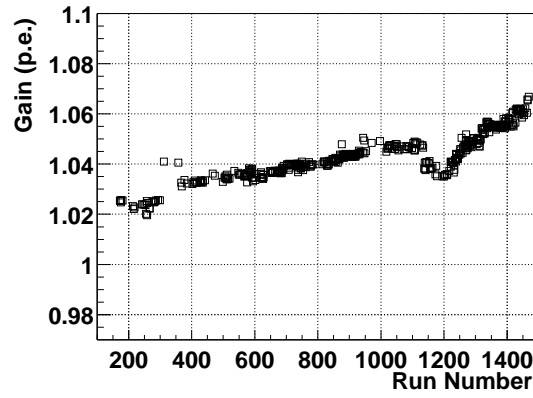


Figure 3.11: PMT gain stability dependence on run number. Gain is slightly increasing.

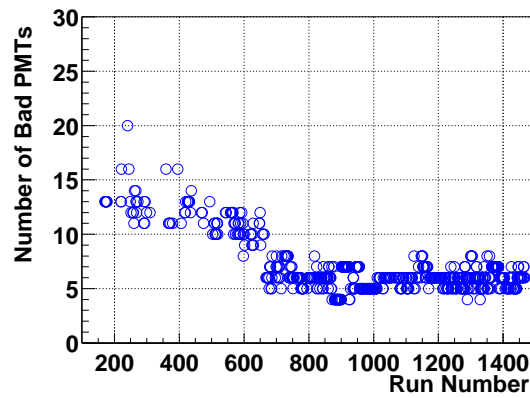


Figure 3.12: Number of bad PMTs as a function of the run number.

The PMT hits within a 150 nsec time window with a charge larger than 0.3 photo-electron are used for energy estimation to reduce accidental dark noise from PMTs, where 150 ns is maximum spread of the arrival time of scintillation light. PMT charges around chimney and bottom region are decreased due to shadowing by the balloon straps and this effect is also corrected for. Charge of masked channels is corrected using the mean charge of the neighboring PMTs.

After the basic corrections, the position dependence and asymmetry of the energy scale along z-axis still exist, and a further radius dependent correction is applied to compensate using the radial dependence of the charge of the spallation neutron sample. The remaining asymmetry comes from the missing PMTs around chimney(~ 20 PMTs) and bottom(~ 5 PMTs). The effect of these missing PMTs are corrected with a solid angle dependent function, and a time dependent correction is done using the 1.46 MeV ^{40}K peak.

After all corrections, the position dependence of the charge is less than 0.8% for all calibration runs, as shown in the Fig.3.13. Circles show the ^{65}Zn calibration and triangles show the ^{60}Co calibration points. The horizontal axis indicates the true vertex position along z-axis, and the vertical axis indicates the overall corrected charge relative to the mean charge.

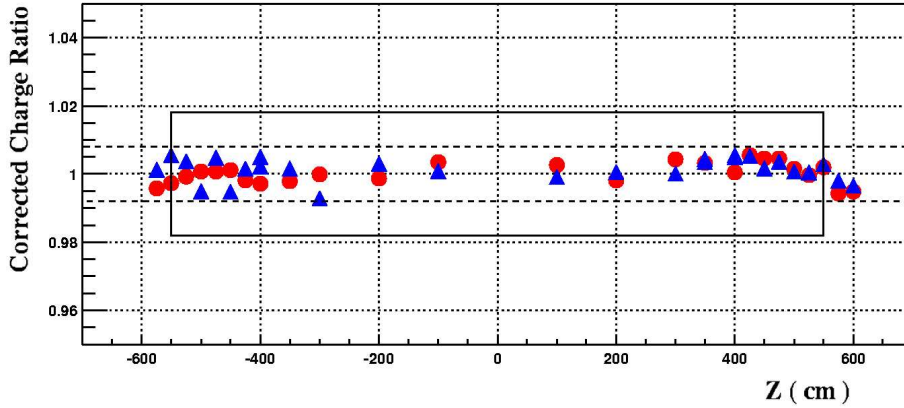


Figure 3.13: Corrected charge as a function of the vertex position z . Charge dependence on the vertex position along the z -axis is less than 0.8% for all calibration data.

Time dependence on charges is also measured by the source calibration data and is found to be 0.6% in the entire data taking periods.

The neutron events induced by muon spallation are found to have a 1.44% position dependence for the entire data sample as seen in Fig.3.14. The left-hand and right-hand figures indicate the radial and z -axis distributions of the neutron events, respectively. The radial distribution indicates a less than 0.5 % position dependence and the z -axis

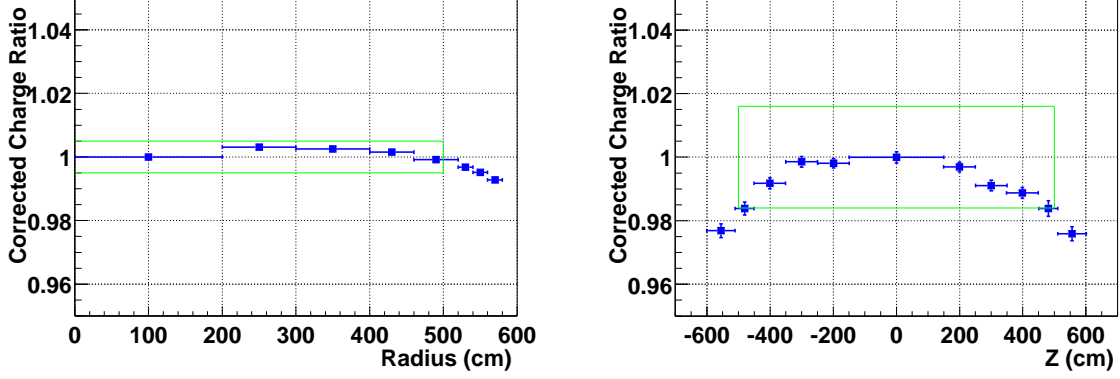


Figure 3.14: Charge dependence of the vertex position using the spallation neutron sample. Two figures indicate the charge dependences of the vertex position as a function of the radius and z position. Boxes indicate the uncertainties of the energy fitter in the fiducial volume region.

distribution indicates a 1.44 % position dependence. This systematic uncertainty contains not only the position dependence but also the time dependence. However the position dependent systematic uncertainty alone is conservatively estimated to be 1.44%. Including time (0.6%) and position (1.44%) dependent uncertainties, the uncertainty from the global energy scale is estimated to be 1.56%.

There is a deviation from the linear relationship between the source energy and reconstructed energy of $^{65}\text{Zn}(\gamma\ 1.116\text{MeV})$, $^{60}\text{Co}(\ 2\ \gamma\text{s}\ 1.173\text{ and }1.332\text{MeV})$ and neutron captured $\gamma(2.225\text{MeV})$. Studies of the energy nonlinearity are described in the next chapter. The energy fitter returns the visible energy at present, which doesn't correspond to the real source energy. The visible energy is defined as a linear relation to the corrected charge, which is overall corrected charge discussed above, and 2.22457 MeV spallation neutron peak is used for the normalization of the slope. The charge distribution of the neutron capture signal within a 200 cm radius of the detector center is shown in Fig.3.15.

The mean value of the charge distribution of the neutron sample is reconstructed to be 710 p.e., corresponding to 2.225 MeV. The definition of the visible energy is written down by

$$(\text{Visible Energy}(\text{MeV})) = \frac{2.225\text{MeV}}{710\text{p.e.}} \times (\text{Corrected Charge}(\text{p.e.})).$$

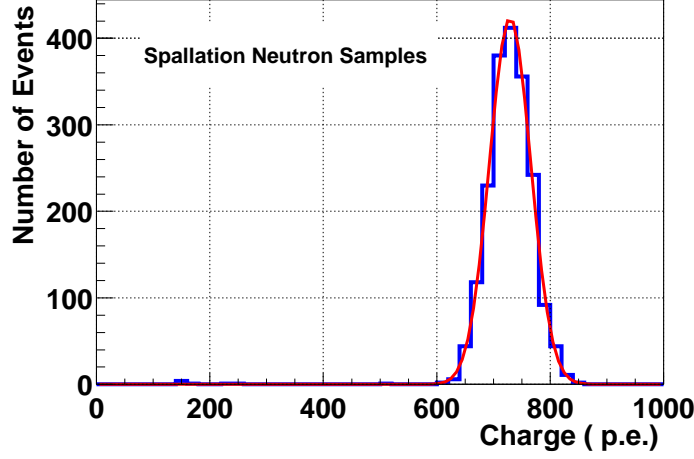


Figure 3.15: The charge distribution of neutrons induced by muon spallation near the detector center.

3.4 Trigger Efficiency

The KamLAND electronics has two different kinds of the triggers for physics data, which are prompt and delayed triggers. The Nsum threshold of the prompt trigger is defined to be 200 PMT hits which corresponds to about 0.75 MeV, and that of the delayed one is 120 hits which corresponds to about 0.4 MeV. The reactor $\bar{\nu}_e$ signal is taken by the prompt trigger. The trigger efficiency of the prompt trigger is estimated using delayed trigger data. That is, the number of delayed events for which nsum is more than that of the prompt threshold versus the total number of delayed events at energy E. That is, the prompt trigger efficiency is written down as following,

$$\epsilon_{\text{prompt trigger}} = \frac{N_{\text{PMT Hits} \geq 200}}{N_{\text{PMT Hits} \geq 120}}$$

Fig.3.16 shows the efficiency of the prompt trigger using the delayed trigger events within a 5 m fiducial volume. The left-hand figure indicates the energy spectrum of the delayed trigger events, upper spectrum indicates total delayed trigger events and lower one indicates the events which PMT hits are above 200. The right-hand figure indicates the prompt trigger efficiency as a function of energy calculated from the left figure.

The detection efficiency of reactor anti-neutrinos is estimated to be 99.98% with a 0.9 MeV threshold by convolving the efficiency curve and the expected reactor anti-neutrino spectrum. The total trigger-related systematic uncertainty is estimated to be 0.02% including energy resolution and scale errors.

The efficiency for the delayed trigger is estimated by a similar method. To estimate

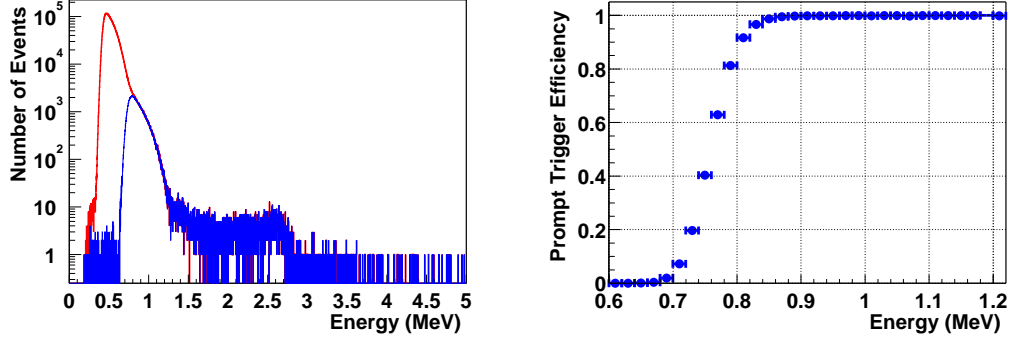


Figure 3.16: Left figure shows the energy spectrum of the delayed trigger events. Upper histogram is the total delayed trigger events and the lower histogram is the delayed trigger events with NsumMax larger than 200. Right figure shows the efficiency curve of the prompt trigger. This histogram is obtained by calculating delayed trigger events above prompt threshold divided by total delayed trigger events.

the efficiency of the delayed trigger, the data for a trigger threshold of less than 120 is needed. In June 2002, we took special data for about an hour to study the background rates of the low energy regions with a trigger threshold of 50. Fig.3.17 shows the efficiency curve of the delayed trigger events as a function of the energy. The detection efficiency is almost 100 % down to 0.5 MeV. This result will be used when U, Th contents in the liquid scintillator are measured.

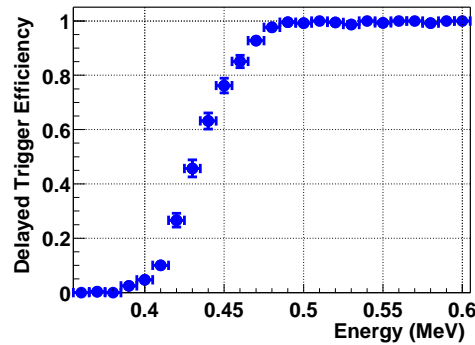


Figure 3.17: Delayed trigger efficiency as a function of the energy. This data is taken by the special low threshold run (Number of hits > 50).

3.5 Muon Fitter

The KamLAND detector is located in an area at an average rock overburden of 2,700 m.w.e. resulting in 0.34 Hz of cosmic-ray muons in the detector volume. Some of these muons interact with nuclei in liquid scintillator and produce radioactive elements. These are called spallation nuclei. Most of these elements emit electrons, gammas or positrons with at most 20 MeV via β^\pm decay, and are a significant background source. As some of these isotopes emit neutrons at the same time, they can be a correlated background for the delayed coincidence signal. It is crucial for the reactor anti-neutrino analysis to identify muon tracks and to remove such correlated backgrounds.

Muon events are selected based on the following conditions,

- Total charge of inner detector $\geq 10,000$ p.e. (~ 30 MeV)

or

- Total charge of inner detector ≥ 500 p.e. and the number of PMT hits in outer detector ≥ 5

The events selected by the above conditions are shown in Fig.3.18. The charge distribution of muon events is shown on the right. The peak with larger charge corresponds to the muons which go through scintillator regions and emit scintillation light, and that with smaller charge corresponds to the muons which go only through the inner buffer region and emit Cherenkov light. As the charge threshold for the muon selection is 500 p.e. or 10,000 p.e., it is found that the whole regions around peaks are covered by this threshold. The time difference from muon to muon is shown in the right-hand figure. The event rate is 0.34Hz.

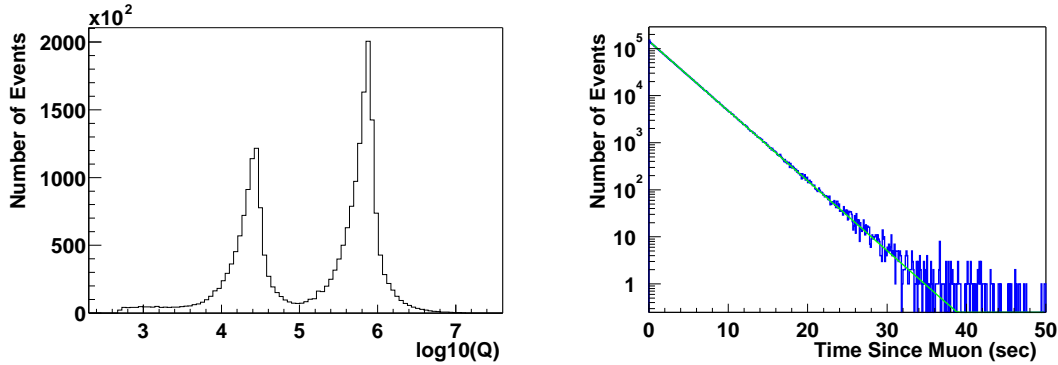


Figure 3.18: The left-hand figure shows the charge distribution of events selected by the muon selection criteria. The lower peak is from muons emitting Cherenkov photons and higher peak is from those emitting scintillation photons. The right-hand figure shows the time difference from muon to muon for events selected by the muon selection criteria. The event rate is 0.34 Hz.

The method for the muon track reconstruction is as follows. First, the “entrance” PMT, which is defined to have earliest timing of the hit and not to be isolated, is identified. Next, the “exit” PMT is identified, which is defined to have largest charge of all PMTs, not to be isolated, and the PMT timing later than that of the entrance PMT. Finally, a badness value for each reconstruction result is calculated using the consistency of the timing between entrance and exit PMT for both the ID and OD. Fig.3.19 shows an example of an event display for a selected muon event. Total charge of inner detector of this event is 1.14×10^6 p.e. and the PMT hits of outer detector is 85. The left figure

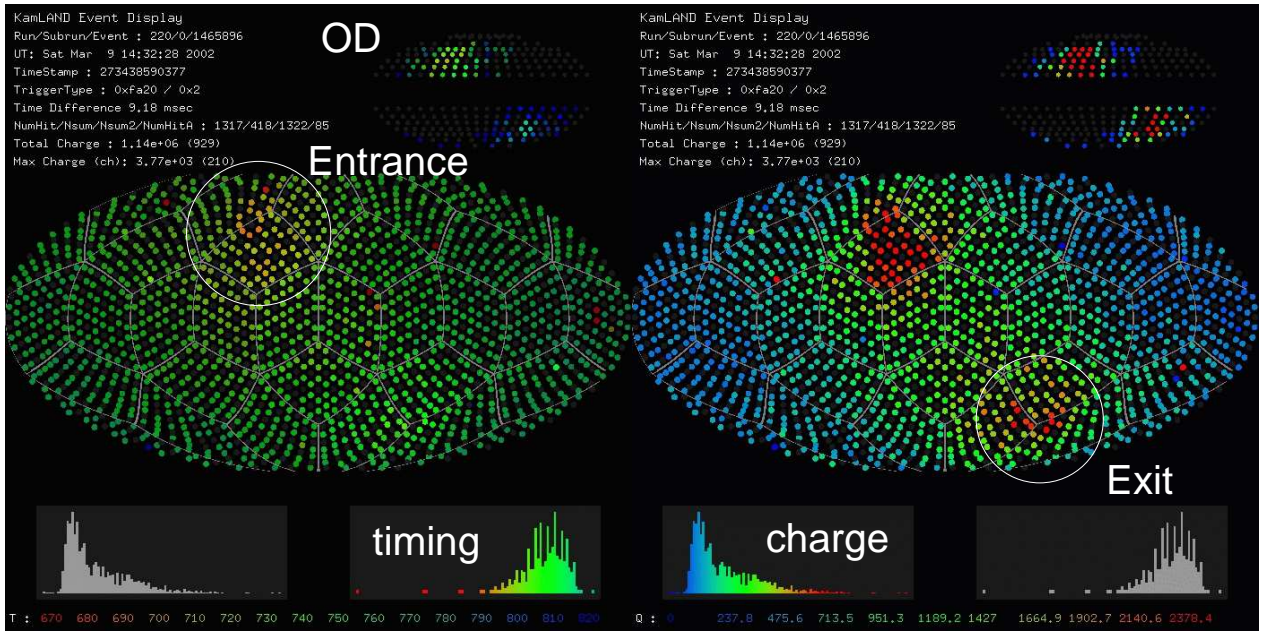


Figure 3.19: KamLAND event display for the muon event.

indicates the timing information and the right figure indicates the charge information. White circle of the left figure indicates the earliest PMT timing and reconstructed as a entrance of the muon. White circle of the right figure indicates the largest PMT charge and the position different from the entrance and reconstructed as a exit. The consistency of this track is checked by the timing information of outer detector.

Using this track reconstruction algorithm, the relation with track length versus charge is measured for both scintillation and cherenkov light. The left-hand plot in Fig.3.20 indicates the reconstructed muon track length in the buffer oil versus total charge of the muons. The minimum light emission in the buffer region per cm (which corresponds to Cherenkov radiation) is measured to be 32.45p.e. The right-hand plot in Fig.3.20 shows the reconstructed muon track length in the scintillator versus total charges of the muons. The cherenkov corresponding charges are already subtracted using above relation.

The minimum light emission at the scintillator region per cm (which corresponds to scintillation radiation) is measured to be 738.4p.e.

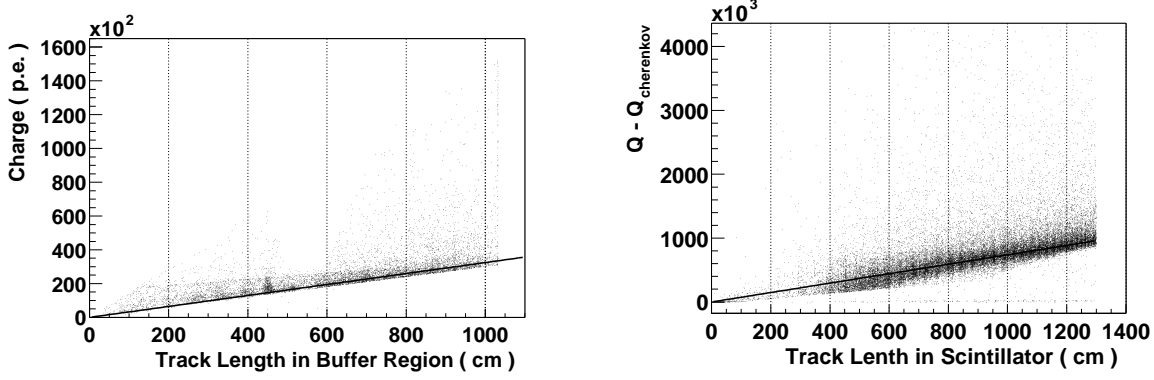


Figure 3.20: Left-hand plot shows the total charge vs. track length in the buffer region. Right-hand plot shows the total charge minus Cherenkov charge vs. track length in scintillator region.

Chapter 4

Calibration

Various calibration methods for the KamLAND detector are described in this chapter. We used LED for PMT gain, laser for PMT timing, and various kinds of radioactive sources for energy and vertex calibration.

4.1 PMT gain

Gain calibration has been performed at 1 p.e. level using 30 LEDs which are installed at peripheral positions in the stainless steel tank. Adjusted gain was $4.7 \times 10^6 \pm 6\%$. 17 inch PMT for the KamLAND experiment has a high performance about the single photo-electron peak. Fig.4.1 shows the single photo-electron distribution of a typical PMT.

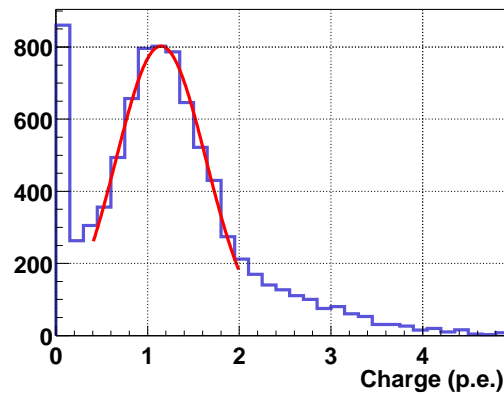


Figure 4.1: The single photo-electron distribution of a typical 17 inch PMT. 17 inch PMT has a high performance about the single photo-electron peak.

A clear peak of the single photo-electron is seen in the figure. Using the single photo-electron peak, the absolute gain correction was done.

Fig.4.2 shows the result of peripheral LED calibration data taken at 4th and 9th March 2002. The left figure shows the 1 p.e. outputs of all PMTs before gain correction and the right one shows those after gain correction. The horizontal axis shows the mean value of the single photo-electron peak of each PMT and the unit is ATWD count. The peak value of the single photo-electron after gain correction is reconstructed to be 184 ATWD counts. 1 pC corresponds to ~ 245 ATWD count, so the absolute gain is corrected to be 4.7×10^6 . The deviation of the single photo-electron peaks for all PMTs is about 6 %. This deviation after gain correction is much improved compared with that before gain correction, which is about 16 %.

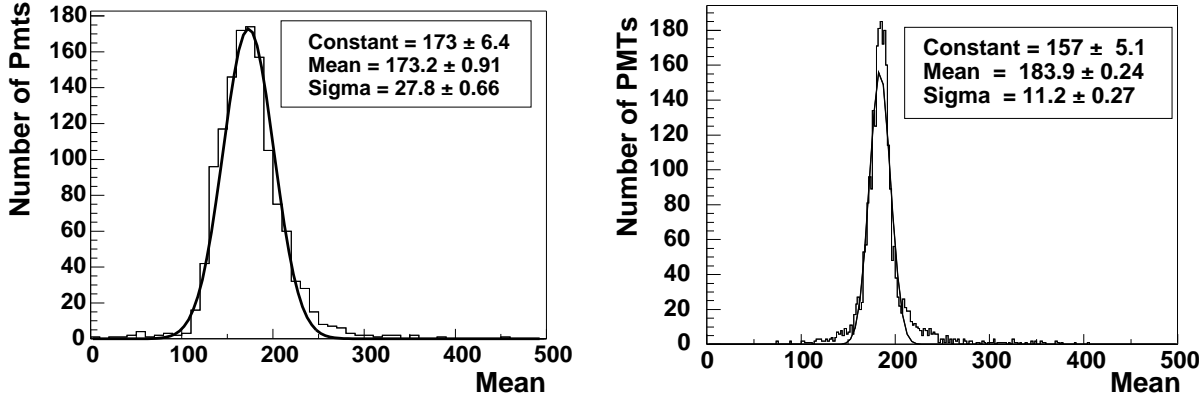


Figure 4.2: The mean single photo-electron peaks of all PMTs before and after gain calibration. The left figure indicates the ATWD counts of the single photo-electron peaks of all PMTs before gain calibration and the right figure indicates that after gain calibration.

4.2 PMT timing

It is essential to obtain accurate relative timing of PMT signals for precise reconstruction of the vertex position. Each PMT has its own time offset because of the differences of the cable length, transit time and slewing behavior and so on. A 500 nm dye laser flasher with a diffuser ball was used to adjust timing to ~ 1 ns precision and to measure charge dependence. Fig.4.3 shows the laser system used for this timing study.

Light pulses from a 500 nm dye laser are injected into a diffusion ball in the detector center through the 230 m optical fiber cable, and the isotropic lights are emitted by the diffusion ball. These lights are detected by all 17-inch PMTs and the time differences between the reference PMT are measured. The intensity can be changed by adjusting

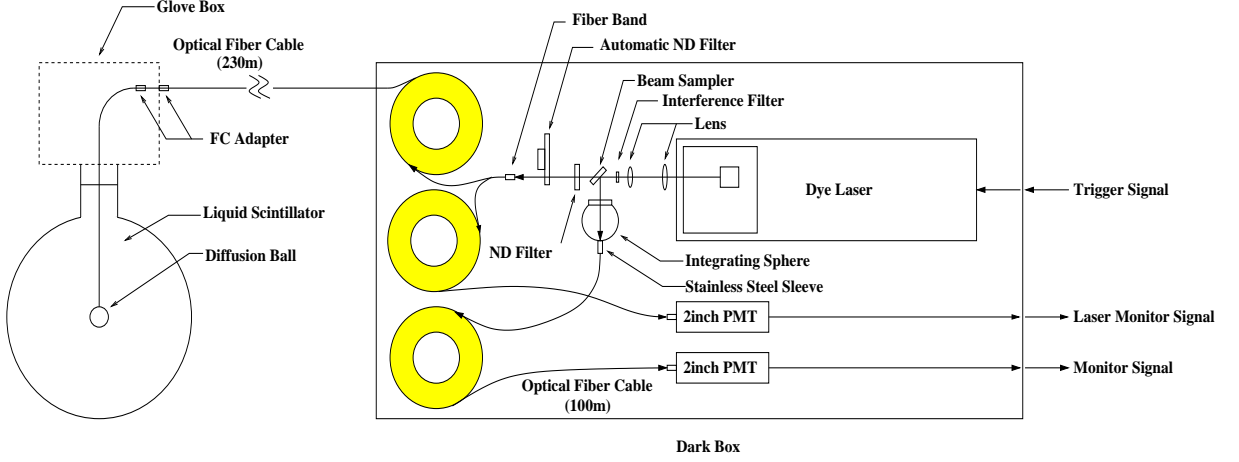


Figure 4.3: Laser calibration system set up.

neutral density filters and is monitored by 2-inch PMT. Other 2-inch PMTs are used for the trigger signal for the ATWD and the reference signal into the ATWD board. The data taking rate is from 8 Hz to 10 Hz.

Fig.4.4 is a plot of the timing response of a PMT as a function of charge (TQ-map). Open circle points show the high gain signal from PMT, plus points show the middle gain signal and star points show the low gain signal. Horizontal axis shows the charge and vertical axis shows the timing by the unit of ATWD count. The slewing effect can be seen in the figure that the larger the charge is, the faster the timing is. The high, middle and low gain TQ map show the different characteristics, and these are treated independently.

The fitting function for the TQ map is described by

$$t(q) = P_0 + P_1(\log_{10}q) + P_2(\log_{10}q)^2,$$

where $t(q)$ is a charge dependent leading edge timing (ATWD count ~ 1.5 ns/count), q is a charge (ATWD count ~ 0.004 pC/count), P_0 , P_1 , and P_2 are free parameters. Typical value for the fitting is $P_0 = 16.19$, $P_1 = -4.15$ and $P_2 = 0.60$. These TQ maps are made for all PMTs and three different gains and two different ATWD channel and used in the event reconstruction.

After all, the timing calibration results are shown in Fig.4.5. The left figure indicates the leading edge timing distribution of the single photo-electron for all PMTs in the laser calibration run before timing calibration, and the right figure indicates that after timing calibration. The timing resolution is improved from 6.7 ns to 2.0 ns.

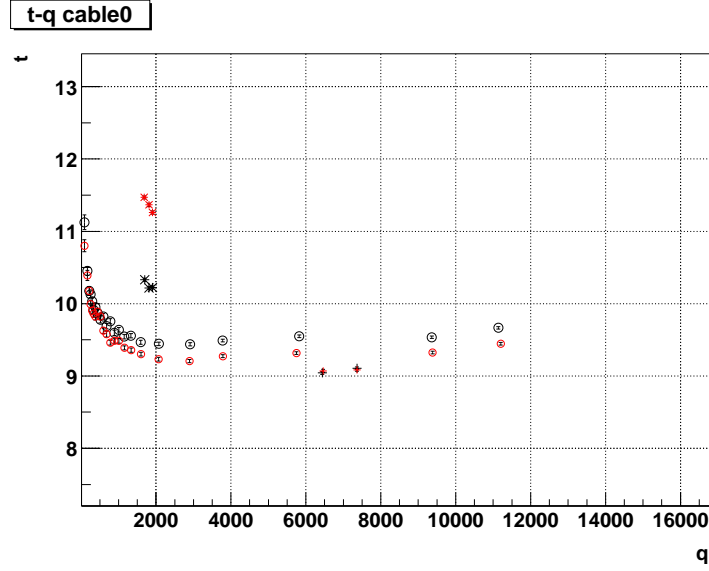


Figure 4.4: Example of a TQ map for one PMT. Circles indicate high gain signals, plus marks indicate middle gain's and stars indicate the low gain's. Black marks indicate ATWD A channel and red indicates ATWD B channel.

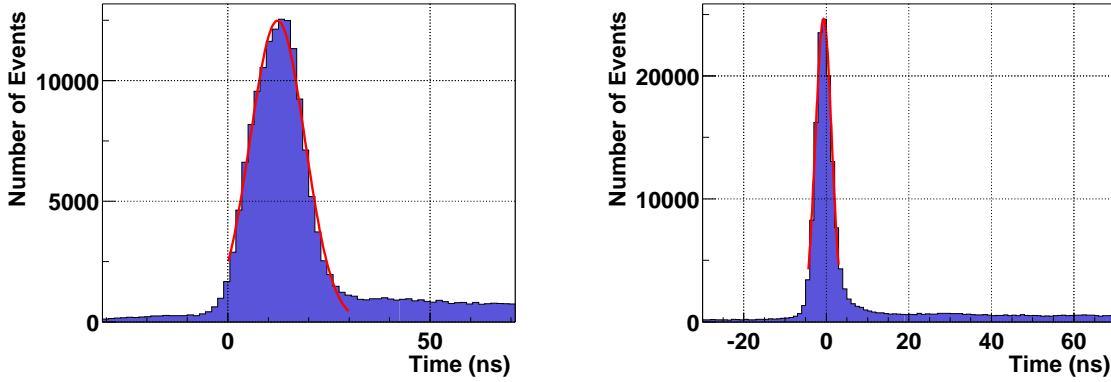


Figure 4.5: Timing calibration effect. The left figure indicates the single photo-electron timing distribution of all PMTs before timing correction. The right figure shows that after timing correction.

4.3 Energy Scale

As mentioned before, there is a non-linearity about the energy response. Fig.4.10 shows the non-linearity of the energy scale in the various energy regions. This figure contains 6 data points which are 0.511MeV ^{68}Ge , 1.116MeV ^{65}Zn , 1.173+1.332MeV ^{60}Co , 2.2246MeV neutron captured by proton, 4.947MeV neutron captured by ^{12}C and 7.652MeV AmBe gamma.

Fig.4.6 shows the ^{60}Co energy calibration results. 1.173 MeV and 1.332 MeV γ are emitted from the ^{60}Co source at the same time, so the summed energy of two γ s are detected. To know the energy non-linearity, mean energy of these two γ s, 1.2525 MeV, is considered for the real energy of this source.

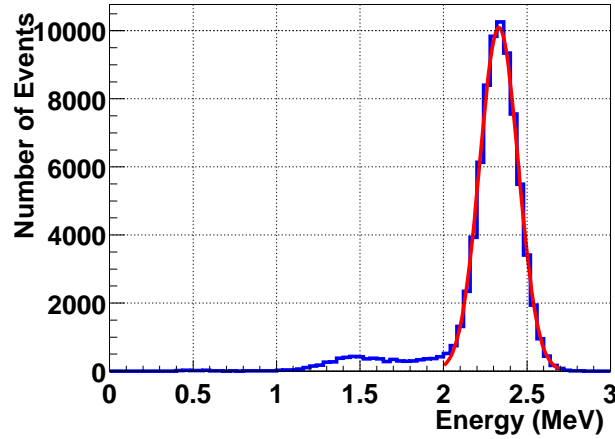


Figure 4.6: ^{60}Co energy calibration results. 1.173 MeV and 1.332 MeV γ are emitted at the same time from the ^{60}Co sources. The summed energy of two γ are detected.

The peak position was reconstructed to be 2.332 MeV. This means the visible energy from this source at the mean energy 1.2525 MeV is 1.166 MeV. So the ratio of the visible energy to the real energy at 1.253 MeV is 0.931. The tail of the low energy region below peak is considered as the Compton scattering of the γ with the source material. As the recoiled electron is absorbed in the source material, the corresponding scintillation photons are not emitted.

Fig.4.7 shows the ^{65}Zn energy calibration results. 1.116 MeV γ are emitted from the source. The peak position was reconstructed to be 1.034 MeV. Energy non-linearity of this energy 1.116 MeV was 0.927. The tail of the low energy region below peak is the same energy loss as the case of ^{60}Co .

Fig.4.8 shows the ^{68}Ge energy calibration results. ^{68}Ge becomes ^{68}Ga after electron capture. Positron with maximum energy 1.9 MeV is emitted from this and two γ s with

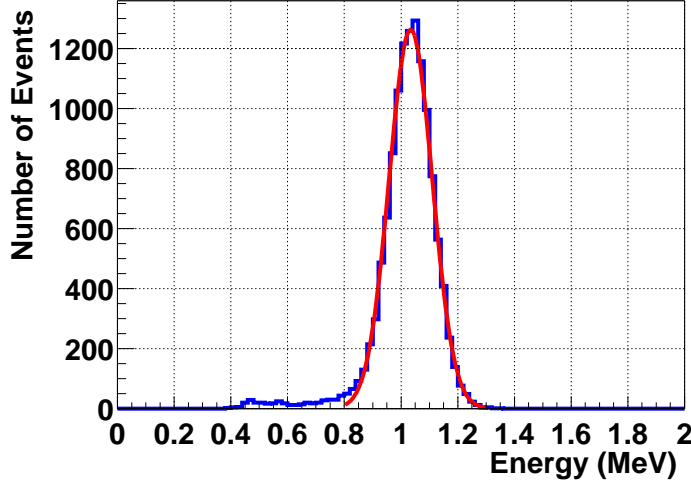


Figure 4.7: ^{65}Zn energy calibration results. 1.116 MeV γ are emitted from the source.

0.511 MeV energy are emitted from the positron annihilation in the source material.

We use the mean energy of 2 γ s, 0.511 MeV for the real energy of this source. The reconstructed energy was 0.8771 MeV. The ratio of the visible energy to the real energy is 0.858. This is the same energy as the threshold of the $\bar{\nu}_e p \rightarrow n e^+$ reactions, so the energy calibration of this energy region is very important for the understand of the uncertainty of the energy threshold. The lower energy events below peak is also the energy loss of the γ by Compton scatterings.

The left figure in the Fig.4.9 shows the 2.22 MeV γ energy spectrum which comes from the muon induced neutron captured by ^1H . This γ source is used for determination of the visible energy scale.

The right figure in the Fig.4.9 indicates the 4.947 MeV γ energy spectrum which comes from the muon induced neutron captured by ^{12}C . This can be also good energy calibration sources because this captured γ energy is larger than those of normal radioactive sources. The cross section of the neutron capture is 0.33 barn at ^1H and 0.0034 at ^{12}C . The natural abundance of ^1H is 99.985 % and that of ^{12}C is 98.893 %. The ratio of Hydrogen/Carbon number is 1.969 for KamLAND liquid scintillator. So, neutron captured by ^{12}C is estimated to occurs 0.5 % relative to that captured by ^1H . The measured neutron captured events by ^{12}C was 0.7% relative to that by ^1H , and this was in good agreement with the expected ratio.

The peak position is reconstructed to be 5.129 MeV. The ratio of visible energy to real energy is then 1.04, that is, there is 4 % energy non-linearity at 5 MeV.

Energy non-linearity is caused by Cherenkov threshold effect, quenching (Birks constant), dark hit and 1 p.e. inefficiency etc. Scintillation light yield doesn't respond

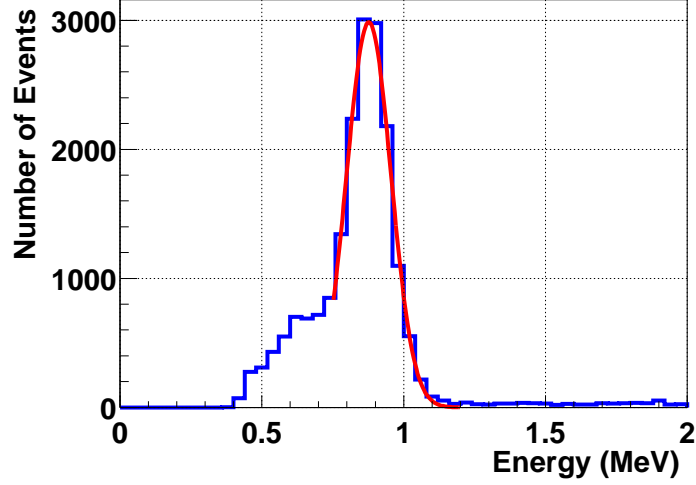


Figure 4.8: ^{68}Ge energy calibration results. 0.511 MeV 2 γ s are emitted from the positron annihilation.

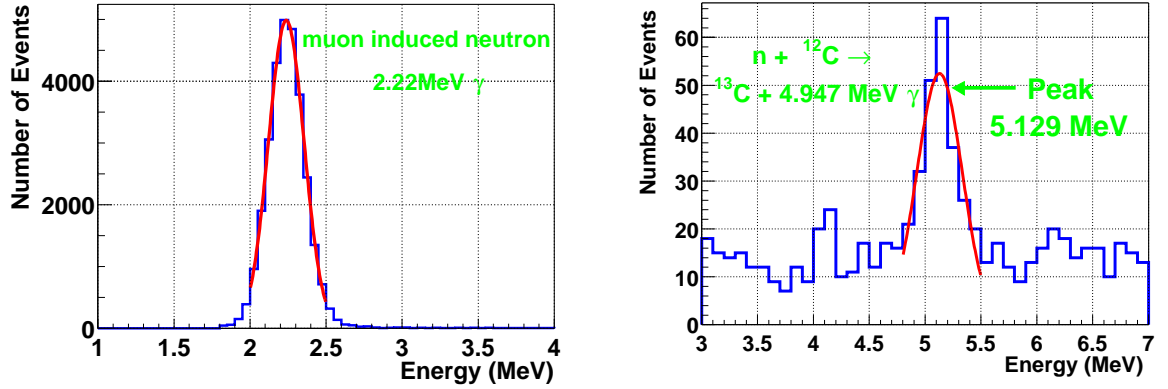


Figure 4.9: The left figure shows that 2.225 MeV γ energy spectrum which comes from the muon induced neutron captured by ^1H . The right figure shows that 4.947 MeV γ energy spectrum which comes from the muon induced neutron captured by ^{12}C .

linearly to the energy deposit, but depends on ionizing density. Very dense ionization particles emit less light than minimum-ionizing particles. A widely used semi-empirical model proposed by Birks posits that recombination and quenching effects between the excited molecules reduce the light yield [40]. These effects are more pronounced when the density of the excited molecules is greater. Birks formula is expressed as

$$\frac{dL}{dx} = L_0 \frac{dE/dx}{1 + k_B dE/dx},$$

where L is the luminescence, L_0 is the luminescence at low specific ionization density, and k_B is Birks constant, which must be determined for each scintillator by measurement.

Dark hit rate is obtained from the 1 pps trigger information. 1 pps trigger is issued at each one second interval and this trigger data contains the accidental random hit rate, that is, dark hit rate. Because dark hit rate is 40 kHz, 10 PMT's on an average are hitting for 125 ns window, while in the energy fitter, 150 ns window is taken for charges to be summed, so 12.0 PMTs are the expected dark hit contribution in the visible energy. As scintillation photon yield is 300 p.e. / MeV, this dark hit corresponds to 0.04 MeV if the mean charge of the dark hit is 1 p.e. If the mean charge of the dark hit is 1/3 p.e., which is trigger threshold, this is the minimum case, the dark energy will be 0.013 MeV. Compiling those considerations, we assume dark energy as $E_{dark} = 0.013$ to 0.04 MeV.

Single photo-electron inefficiency can also cause the energy non-linearity. Probability of 1 p.e. detection if there is no threshold effect, is

$$p(1) = ue^{-u},$$

where u is the mean number of photoelectrons, $u = 1/1325 \times E \times (300 \text{ p.e./MeV})$. Assuming single photo-electron efficiency $\text{Eff} = 90 \%$, the probabilities are

$$\begin{aligned} p(0) &= e^{-u} + (1 - \text{Eff}) \times ue^{-u}, \\ p(1) &= \text{Eff} \times ue^{-u}, \\ p(N) &= \frac{u^N e^{-u}}{N!} \quad (N \geq 2). \end{aligned}$$

The visible energy E_{vis} is calculated by adding up charges, so

$$E_{vis} = Q(1) \times p(1) + \sum_{N \geq 2} (Q(N) \times p(N)).$$

If there is no threshold effect,

$$\sum_{N \geq 1} (Q(N) \times p(N)) = uQ_1 \equiv E_{vis_no_thr},$$

where Q_1 is the mean charge of the single photo-electron events with no threshold effect. Then, considering that only single photo-electron events are affected by the threshold

effect, E_{vis} is converted to

$$\begin{aligned} E_{\text{vis}} &= uQ_1 - ue^{-u} \times Q_1 + Q(1) \times \text{Eff} \times ue^{-u} \\ &= E_{\text{vis_no_thr}}(1 - e^{-u}(1 - \frac{Q(1)}{Q_1}\text{Eff})), \end{aligned}$$

where $Q(1)$ is determined from the following relation,

$$Q_1 = Q(1) \times \text{Eff} + Q_{\text{loss}}(1 - \text{Eff}),$$

where Q_{loss} is the mean charge of the events under threshold, it should be less than 1/3 p.e. After all,

$$E_{\text{vis}} = E_{\text{vis_no_thr}}(1 - \delta e^{-u})$$

relation is extracted, where $\delta = Q_{\text{loss}}/Q_1(1-\text{Eff})$. Q_{loss}/Q_1 should be less than 0.33 as described above, then, $\delta = 0.33 \times (1-0.9) = 0.033$ can be the safe maximum value for single photo-electron inefficiency.

All of these effects are included into the Monte Carlo simulation and those 6 γ data are fitted by three free parameters (Birks constant, Cherenkov intensity and global normalization factor). Calibration data points from ^{60}Co , ^{65}Zn , ^{68}Ge , AmBe, neutron capture γ s and the fitting result are shown in Fig.4.10.

The uncertainty from the energy non-linearity is estimated to be 1.1 %. Including all systematic errors of the energy scale estimation, total systematic error becomes 1.91% at 2.6MeV threshold, this corresponds to be 2.1% systematic error for the anti neutrino detection.

Fig.4.11 indicates the fractional deviation of the reconstructed energies from the source energies, and the systematic errors are also plotted by the dashed line.

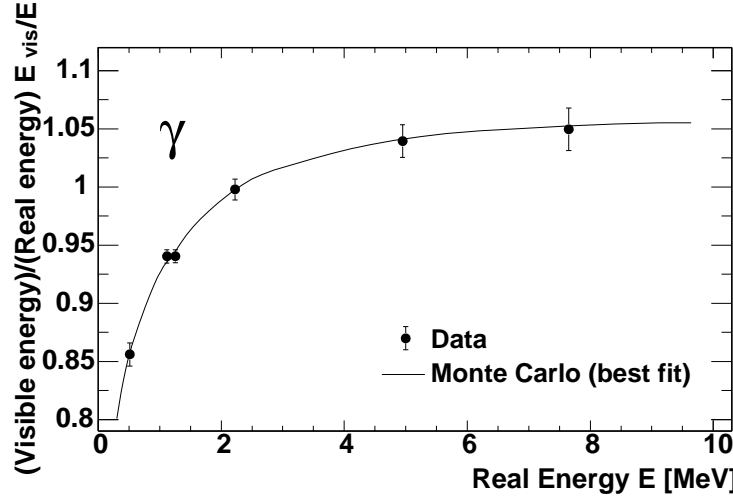


Figure 4.10: The calibration data points from ^{60}Co , ^{65}Zn , ^{68}Ge , AmBe and neutron capture γ s. The horizontal axis indicates the real energy of the source and the vertical axis indicates the ratio of the visible energy to the real energy at each energy. Circles indicate the source calibration data. The best fit result of the Monte Carlo simulation is also shown by the smooth line.

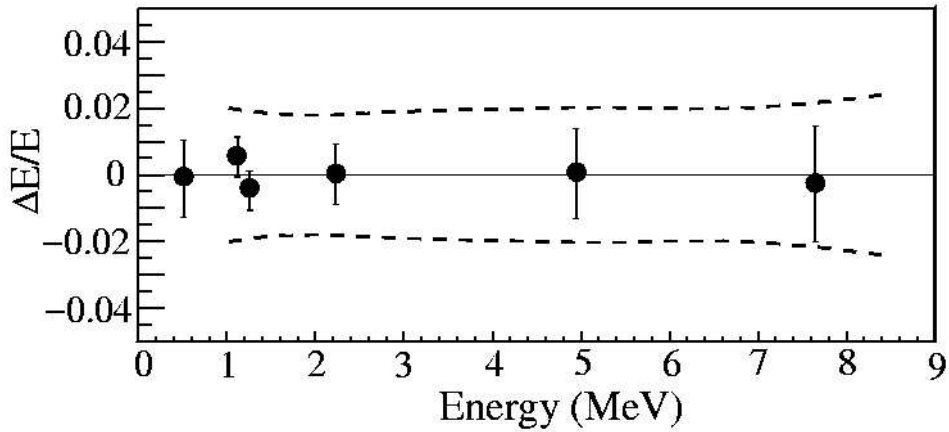


Figure 4.11: The fractional difference of the reconstructed average γ energies and average source energies. The dashed line shows the systematic error.

Chapter 5

Event Selection

Event selections for the reactor neutrino analysis are described in this chapter. The various selection criteria are applied for the data set to improve the quality of data samples. Total data set consists of physics runs taken during March 4 2002 to October 6 2002. The condition of the KamLAND detector livetime during those period is described in Sec.5.1. Bad run and bad period selections are explained in Sec.5.2, cosmic ray muon selection is in Sec.5.3, electric noise in Sec.5.4, fiducial in Sec.5.6, delayed coincidence in Sec.5.7, energy in Sec.5.8 and muon spallation cut in Sec.5.9. The final sample for the reactor neutrino analysis are described in Sec.5.10.

5.1 Detector livetime

Total data set used for this reactor neutrino analysis consist of physics runs taken during March 4 2002 to October 6 2002, 217 actual elapsed days. The run is a basic unit of the KamLAND data set and is updated once a day in case of normal condition. Physics run is taken all day long except for the detector calibration, hardware and software maintenances, etc. Fig.5.1 shows the KamLAND detector operation conditions during the whole data sample. Integrated time taking physics data was 173.1 days, which corresponded to roughly 80% of actual elapsed time (217 days). At the beginning of the data taking, the hardware and software maintenances were performed frequently. Now the detector calibration is the main reason for the time not taking physics data. Bad run and bad period selections reduce this 173.1 days samples to 163.8 days, as will be described in the next section. Furthermore, the spallation cut reduces this to 145.1 days, as will be described in Sec.5.9. After all, 145.1 days samples are used for the reactor $\bar{\nu}_e$ analysis.

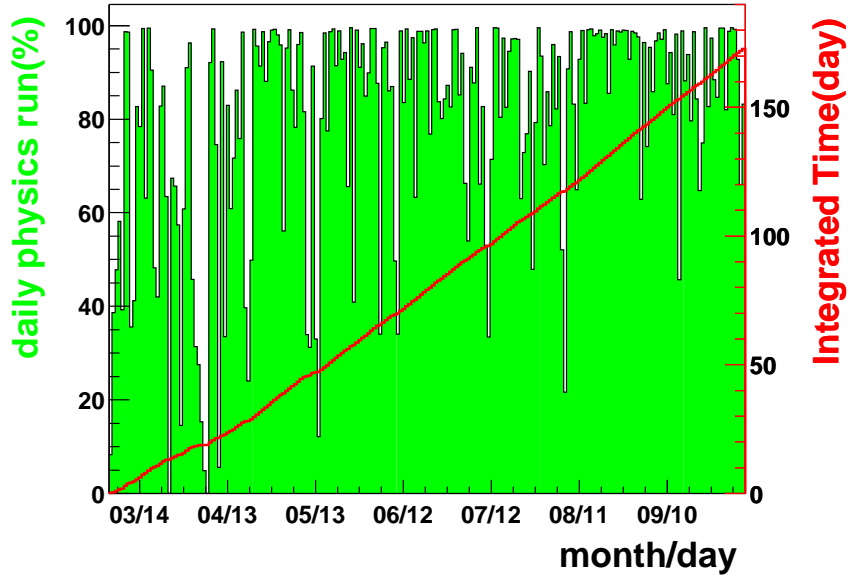


Figure 5.1: KamLAND detector operation conditions. Filled histogram indicates the daily time portion taking the physics runs. Line indicates the integrated physics data taking time.

5.2 Bad Run Selection

The basic unit of the dataset is a run and each run continues at most 24 hours long. Before event selections are done, the qualities of the data are checked run by run. The check items are following.

- The number of bad channels are too many or all channels in ATWD board unit are bad.
- Trigger rate is abnormal.
- The ratio of deadtime to run time is too high.
- Run time is less than 6 minutes.
- The number of hits in outer detector is abnormal.
- Muon rate is abnormal.
- Event rate between 1.5 and 10 MeV is abnormal.

If a run satisfies such bad run criteria, the run is removed from our analysis. Furthermore, the number of bad channels and the muon rate are checked in each 30 minutes in each run, and if the data of some period is quite different with the normal data, the bad period is removed at a unit of 30 minutes.

The physics data taking time from March 4th to October 6th was 173.1 days, that is, the physics data taking efficiency was $\sim 80\%$. After bad run and bad period selection, the remained run time was 163.8 days, so the bad run and bad period were 9.3 days, 5.4 % of total run time. The main reason of the bad run was that the number of bad channel was too many. About 5.5 days data was rejected by this reason. The other reasons were abnormal trigger rate, muon rate and too short run time, etc.

5.3 Charge Selection

First of all, muon selection is applied for all dataset. The selection criteria are following.

- Total charge of inner detector $\geq 10,000\text{p.e.}$ ($\sim 30\text{MeV}$)
or
Total charge of inner detector $\geq 500\text{p.e.}$, the number of PMT hits in outer detector ≥ 5
- Not-noise data ($N_{100} > 0.5 \times (N_{\text{hitID}} + 50)$)

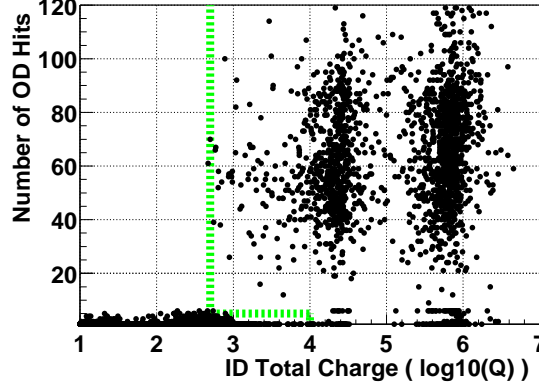


Figure 5.2: The 2 dimensional plot of the number of OD hits versus the total charge of inner detector. Dot line indicates the selection criteria for the muons. Events with right-upper regions divided from the line are selected as muons.

Fig.5.2 shows the two dimensional plot of the number of OD hits versus the total charge of inner detector.

The clusters around 10,000 and 1,000,000 of ID total charge are muons which emit Cherenkov, scintillation photons, respectively. The low energy events with the ID total charge less than 500 p.e. don't have OD PMT hits larger than five. This indicates the probability of the accidental muon selection is low and the rate of accidental muon selection is estimated to be 10^{-5} Hz as will be discussed below.

The distribution of the number of OD PMT hits are shown in Fig.5.3. The solid histogram shows the number of OD PMT hits of the total events, and the dashed histogram shows the number of OD PMT hits selected by the muon selection criteria.

Noise data will be explained in the next section. Fig.5.4 shows the total inner charge distribution of all events. Unshaded histogram indicates the charge distribution of total events. Hatched histogram indicates the charge distribution of the low energy events and the events in the hatched area larger than the charge 10,000 p.e. are the noise events. The events in the white area, which are the upper histogram minus hatched histogram, are selected as muons. Two dot lines indicate the muon charge selection lines, 500 p.e. and 10,000 p.e., respectively.

The detection inefficiency for the reactor $\bar{\nu}_e$ by this muon selection with total charge larger than 10,000 p.e. is 0% because 10,000 p.e. corresponds to around 30 MeV. The event rate of the total charge larger than 500 p.e. is about 19 Hz, and that of the number of hits of OD larger than 5 is about 4 Hz. As trigger waiting time for one event is about 125 ns, accidental muon selection rate is $19 \text{ Hz} \times 4 \text{ Hz} \times 125 \text{ ns}$, that is, 10^{-5} Hz. This means the inefficiency of the 2nd cut is 5×10^{-7} for the reactor anti-neutrino.

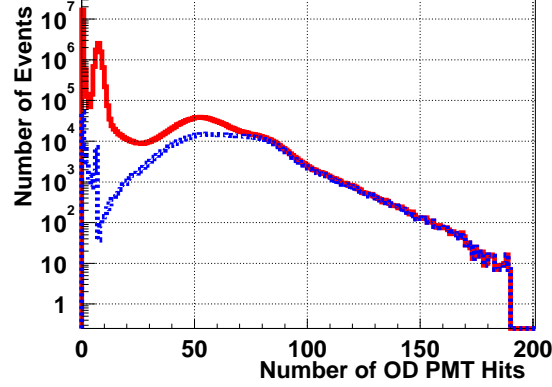


Figure 5.3: The distribution of the number of OD PMT hits. The solid histogram shows the number of OD PMT hits of the total events. The dashed histogram shows the number of OD PMT hits selected by the muon selection criteria.

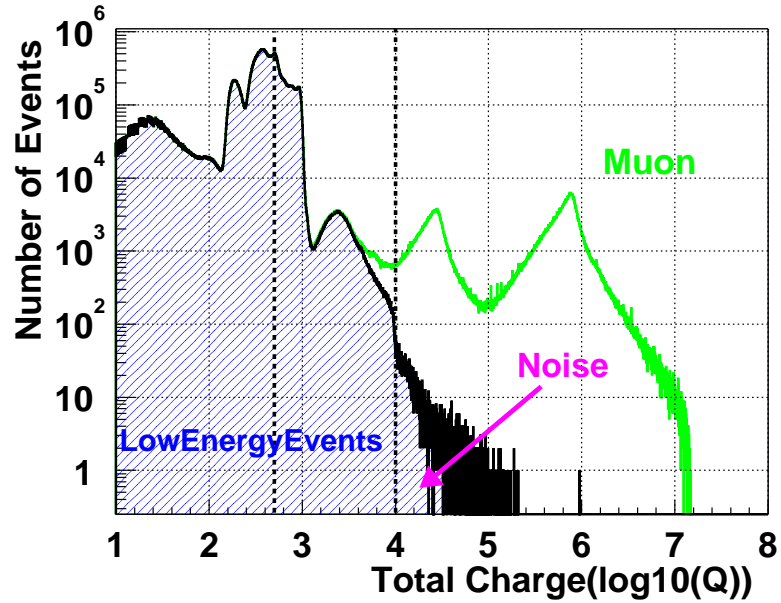


Figure 5.4: The total charge distribution of the inner detector. Unshaded histogram indicates the charge distribution of total events. Hatched histogram indicates the low energy events remained by muon selection. Low energy events larger than 10,000 p.e. are noise events which are not selected as muons. The region shown by upper histogram minus hatched histogram corresponds to the selected muon samples.

5.4 Noise Cut

5.4.1 Noise Event

KamLAND electronics goes in busy status just after high energy events, such as muon and several noise events follow these events. Noise events occur by the following reasons. If an ATWD gets a large amount of charges from the PMT, the overshoot and undershoot waveforms follow the large pulse. At that time, the baseline of the ATWD becomes unstable. If the dark hits are accidentally occurred at the higher baseline than normal, it can easily get over PMT threshold. If the number of those PMTs get over the trigger threshold, trigger issues the prompt trigger. But these ATWD waveforms have no real signals. So, these events are not the physics data but the electronics noise events. Typical feature of these events is a broken PMT timing information. Fig.5.5 shows the timing distribution of a normal low energy event and a noise event.

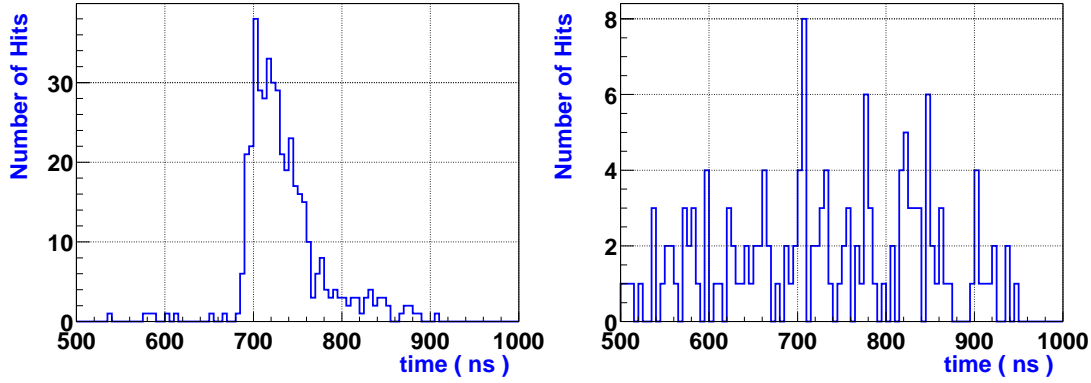


Figure 5.5: The time distribution of the normal low energy event and of the noise event. Left figure indicates a normal event and right figure indicates a noise.

As clearly shown, the time distribution of the noise event spreads flat in the time window. On the other hand for the real event, most of the timing comes within 100 ns. So we use the N100 parameter which is defined as the maximum number of hit PMTs within 100 ns in an event. Fig.5.6 shows a 2-dimensional plot of the N100 versus the number of hit PMTs. The solid line shows the function, $N100 = 0.5 \times (N_{hitID} + 50)$.

Normal data are distributed at the upper side of the solid line in Fig.5.6 because the timings of most hit PMTs are within 100ns. On the contrary, noise events are distributed at the lower side of that. These noise events are rejected by the solid line.

Most of these events occur just after muon events. For anti-neutrino analysis, the events for 2 milliseconds after muon are vetoed to remove spallation neutron background as will be explained in the section 5.5. The event rate rejected by this noise cut whose number of hits is above 200 is less than 5×10^{-6} Hz, which is less than 0.0002% of all

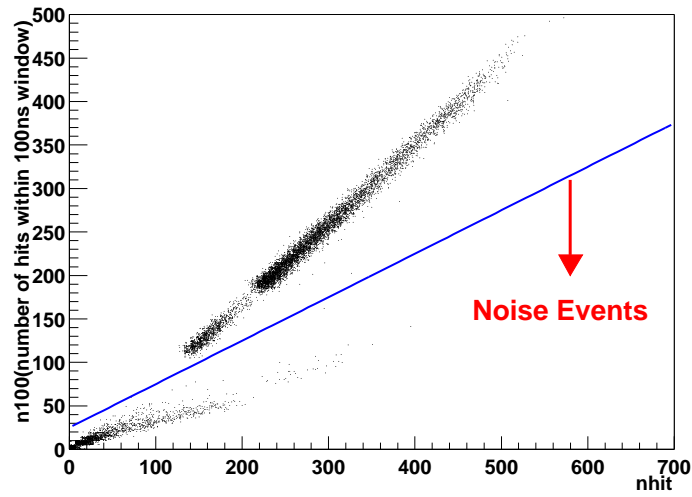


Figure 5.6: Noise event selection criteria. Horizontal axis indicates the number of PMT hits and the vertical axis indicates the N100 which is defined as the number of PMT hits within 100 ns time window in an event. The timing distribution is almost flat for the noise events, so N100 of the noise events is smaller than that of normal events. The solid line shows the noise selection criteria.

events. Therefore inefficiency of this noise cut for the reactor anti-neutrino analysis is less than 0.0002%.

5.4.2 Flasher Event

Some PMTs emit lights presumably due to discharge in dynodes. These PMTs are called Flasher PMT. Typical features of the flasher events are that the charge of a PMT is very high (\sim several 1000 photoelectrons), and the surrounding 20 \sim 30 PMTs also detect photons. But the trigger is not issued by only these flasher events because trigger threshold is based on 200 PMT hits, not on charge. If very low energy event and the flasher event occur at the same time and PMT hits becomes larger than trigger threshold, these events are detected. We remove these events in our analysis because the vertex and energy reconstructions are difficult for these events and original energy of almost all events are below threshold. The selection criteria for the flasher events are following.

- Total charge of inner detector ≥ 2500 p.e.
- Max PMT charge divided by total charge of inner detector ≥ 0.6
- Mean neighbor charge ≥ 20
- Not noise event

Max PMT charge means the charge of the PMT which has a maximum charge in all hit PMTs and neighbor charge means the mean charge of the neighbor PMTs surrounding flasher PMT.

Fig.5.7 shows 2-dimensional plot of these cut conditions. The left figure shows the scatter plot of the max PMT charge / total charge versus total charge. The solid line shows the cut condition for the flasher candidate events. Events in the right and upper region of the solid line are rejected as flasher candidates. Right figure shows that of the max PMT charge / total charge versus neighbor charge. The solid line is same as that of left figure.

The flasher event rate in our whole data samples is 3×10^{-3} Hz which corresponds to 0.01% of total low energy events. As most of these flasher events can not be the normal low energy events, inefficiency of the flasher cut for the reactor anti-neutrino analysis is expected to be less than 0.01 %.

5.5 Muon 2ms Cut

There are neutrons which are emitted directly from the liquid scintillator nuclei by interaction with muons. These neutrons are thermalized and captured by protons after ~ 210 μ sec, and then emit 2.2 MeV γ . If two or more neutrons are emitted at the same time,

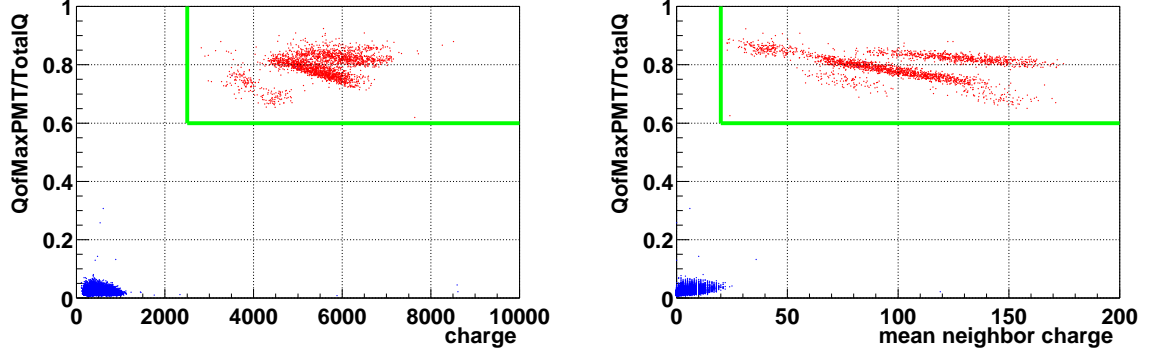


Figure 5.7: Flasher cut conditions. Left figure indicates the scatter plot of the MaxPMTCharge / TotalCharge versus total charge. Solid line indicates the cut condition for the flasher. The events at the right and the upper side of the line are rejected as flasher candidates. Right figure indicates the MaxPMTCharge/TotalCharge versus neighbor charge. The events at the upper-right side of the line is rejected as flasher candidates.

these events mimic a delayed coincidence signal. So, we set all volume cut after muons for 2 milliseconds. Fig.5.8 shows the energy spectrum before and after the muon 2ms cut with fiducial 5 m.

Before applying the muon 2ms cut, a clear peak around 2.2 MeV are seen in the figure. After applying the cut, the peak disappears and a peak around 2.6 MeV γ by ^{208}Tl from the surrounding rock etc. are only remained. As the muon rate of inner detector is 0.34 Hz, the total dead time from muon 2ms cut is $0.34 \text{ Hz} \times 0.002 \text{ sec.} \sim 0.07 \%$.

Fig.5.9 shows the summary of the muon, noise and flasher event selections. Low energy events and muon events are same as Fig.5.4. The cuts of noise and 2 millisecond after muon are found to be very powerful cuts. The range of the $\bar{\nu}_e$ events is also shown.

5.6 Fiducial Selection

Fig.5.10 shows the energy spectrum at various fiducial volume conditions. From the top, no cut, $R < 6\text{m}$, 5.5m, 5m and 4m fiducial cuts are plotted. The lowest histogram shows the histogram of the 4m cut and the central cylindrical cut with 1.2m radius. A bump around 0.8 MeV indicates the prompt(or global) trigger threshold and that around 0.5 MeV indicates the delayed trigger threshold. Peaks around 1.5 MeV correspond to the γ of ^{40}K from balloon surfaces, ropes or outside the balloon. Peaks around 2.6 MeV is the γ of ^{208}Tl from balloon surfaces or the surrounding rock. γ -rays from ^{208}Tl , which is originally $\simeq 3 \text{ Hz}$, are strongly suppressed by the fiducial volume cut, and the single

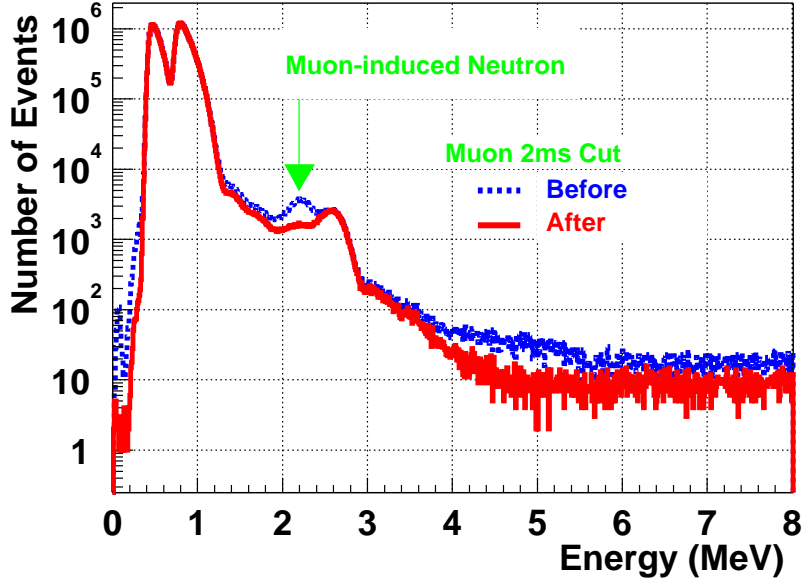


Figure 5.8: Energy spectrum before and after muon 2ms cut with fiducial 5 m.

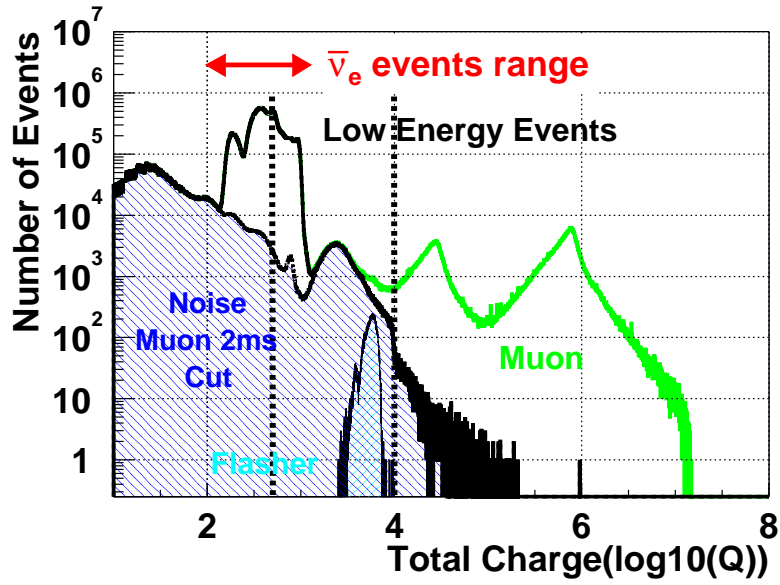


Figure 5.9: Summary of the charge selection. Muon, flasher, noise and muon 2 msec cut and remained low energy event samples are shown.

rate becomes $\simeq 0.01$ Hz. The dominant sources above 5 MeV are the spallation products from muon. The histogram of 4 m fiducial show the similar event rates as that of 5 m fiducial at the energy region larger than 3 MeV. This is why the dominant background sources are concentrated in the center. There are three thermometers and their cables along the z-axis. Furthermore, some radon can be contaminated and emanated from the top of the detector into these regions when calibration device is put on along the z-axis. The bottom histogram labeled '4 m + cylinder 1.2 m cut' means the cylindrical region with radius 1.2 m along z-axis is cut to remove events of these regions. This histogram shows the dominant sources from 3 MeV to 4 MeV is coming from the center regions. We apply cylindrical cut with 1.2 m only for delayed events. This will be explained in the section 5.7.

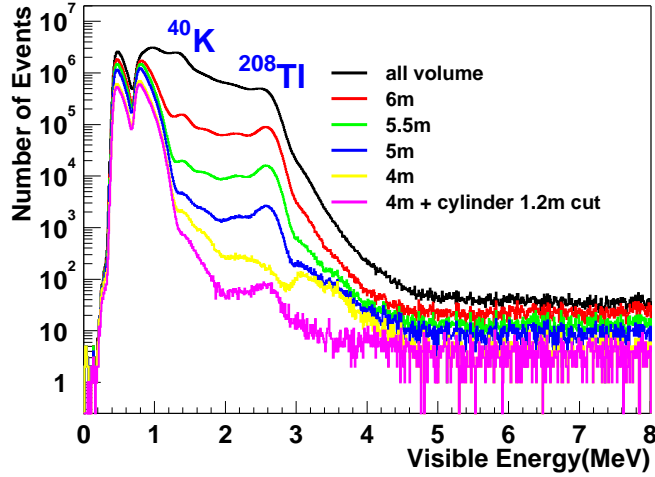


Figure 5.10: Energy spectrum at various fiducial volume conditions, all, 6m, 5.5m, 5m and 4m from the top. The lowest histogram shows the 4m fiducial plus 1.2m central cylinder cut.

Fig.5.11 shows the vertex distributions of the delayed coincidence events without the fiducial volume cut. The space correlation within 160 cm and the time correlation between 0.5μ sec and 660μ sec and the prompt energy larger than 2.6 MeV and delayed energy between 1.8 MeV and 2.6 MeV are applied. Horizontal axis indicates the X^2+Y^2 (m^2) vertex position of the delayed events, and vertical axis indicates the Z (m) vertex positions. The event rates at the positions around $Z \sim \pm 6.5$ m are higher than other regions. And the event rates around balloon surfaces, $R \sim 6.5$ m indicated by dot line, are also higher than other regions. So we need to apply the fiducial volume cut and need to reduce these environmental background, mainly accidental background. These areas with the event rates higher than other regions contain extra environmental γ s, and these will be

explained later.

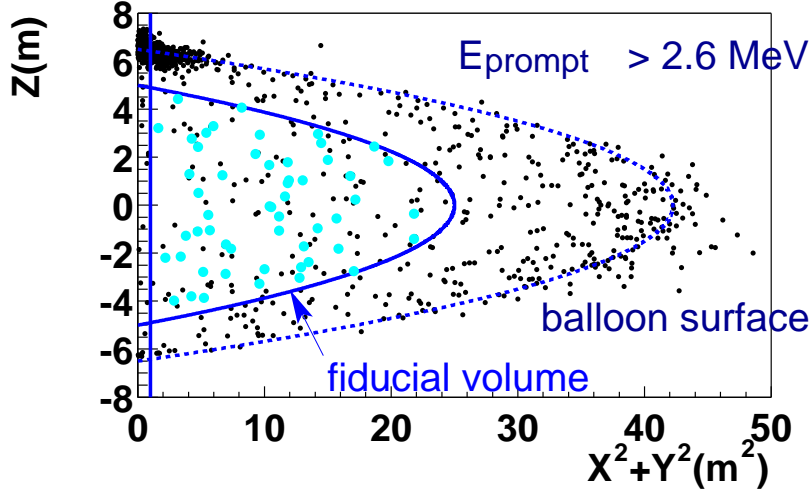


Figure 5.11: The vertex distribution of the delayed coincidence events without the fiducial volume cut. The regions with event rates higher than other regions are seen at around $Z \sim \pm 6.5$ m and at around balloon surfaces, $R \sim 6.5$ m. Dashed line indicates the balloon surface and smooth line indicates the fiducial volume. The line with $X^2+Y^2=1.44$ m² indicates the cylinder cut for the delayed events. Large circle data indicates the final samples after all cuts.

To reduce external backgrounds from the surrounding rock and the detector materials and systematic uncertainties associated with event reconstruction near balloon edge, fiducial volume is defined to be within 5 m from the detector center. This fiducial volume corresponds to 523.6 m³ or 408.5 ton.

Fig.5.12 shows the vertex distribution of low energy real events. Left figure indicates the vertex distribution as a function of radius. The peak around 650 cm indicates a balloon surface and there are many background events around balloon surface. Hatched histogram indicates the events after fiducial volume cut. The contaminations of these surface events are low enough at fiducial 5 m. Right figure indicates the vertex distribution as a function of z . The peaks around $Z \sim \pm 650$ cm indicate the chimney and bottom regions. Chimney region has an extra liquid scintillator part connected to the top of the detector. The low energy γ s coming from the top of the detector or the balloon surfaces are contaminated into these regions. The bottom region has a flange which connects the balloon and the pipes which is used for oil circulation. The effect of the backgrounds from this flange is seen in that figure. Once we select the 5 m fiducial, these contaminations from chimney and bottom regions can be removed, and the contribution from balloon surfaces is also reduced.

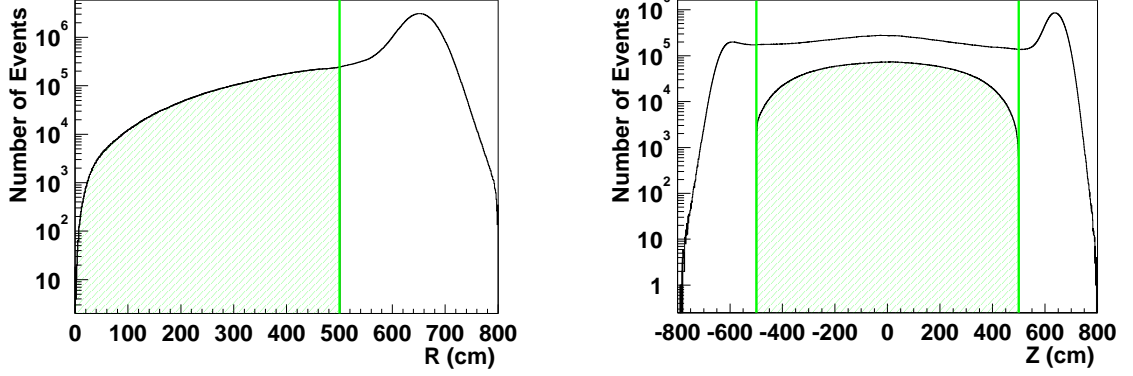


Figure 5.12: The vertex distributions of the low energy real events. Left and right figures indicate the vertex distributions as functions of event radius and z , respectively. Hatched histogram indicates the events within the fiducial volume.

Fig.5.13 shows the energy spectrum of the events within the fiducial volume and outside the 1.2 m central cylinder along the z -axis. Background contaminations of ^{40}K , ^{238}U and ^{232}Th are measured to be $< 2.7 \times 10^{-16}$ g/g, 3.5×10^{-18} g/g and 5.2×10^{-17} g/g explained in the chapter 6. The expected theoretical lines for the ^{40}K , ^{238}U , ^{232}Th and the spallation products such as ^{12}B (64 events/day/kton measured), ^9C , ^8Li , ^8B , ^8He , ^9Li , ^6He , ^{11}C and ^{10}C from [46] are also shown in the figure. Delayed trigger signals are normalized to the prompt trigger time. ^{210}Pb is dominant below 1.3 MeV, and ^{85}Kr is dominant below 0.8 MeV. The theoretical line is well explained by these measured or expected data except for the ^{208}Tl . ^{208}Tl is coming from the balloon surfaces or the surrounding rock, the single rate from the ^{208}Tl is measured to be ~ 0.01 Hz.

5.7 Space, Time Correlation

Space and time correlations between prompt and delayed signal in KamLAND scintillator are studied with Geant4 simulation. Input parameters of the liquid scintillator are following. Temperature of the liquid scintillator is 11.5 °C, density is 0.780 g/cm³, the ratio of dodecane to pseudocumene is 80.2 to 19.8, and PPO concentration is 1.52 g/cm³.

Prompt events, 3 MeV positron and 0.511 MeV γ events of annihilation are generated, and the positron mean path range is simulated to be 0.63cm. So the positron diffusion can be almost negligible within the vertex fitter resolution. For delayed events, 2.22457 MeV γ and neutron with the energy around 10 ~ 20 keV are generated independently. The neutron recoil energy at the reactor anti-neutrino energy is an order of 10 keV, and the diffusion length of recoiled neutron is simulated to be around 9 cm, and the capture

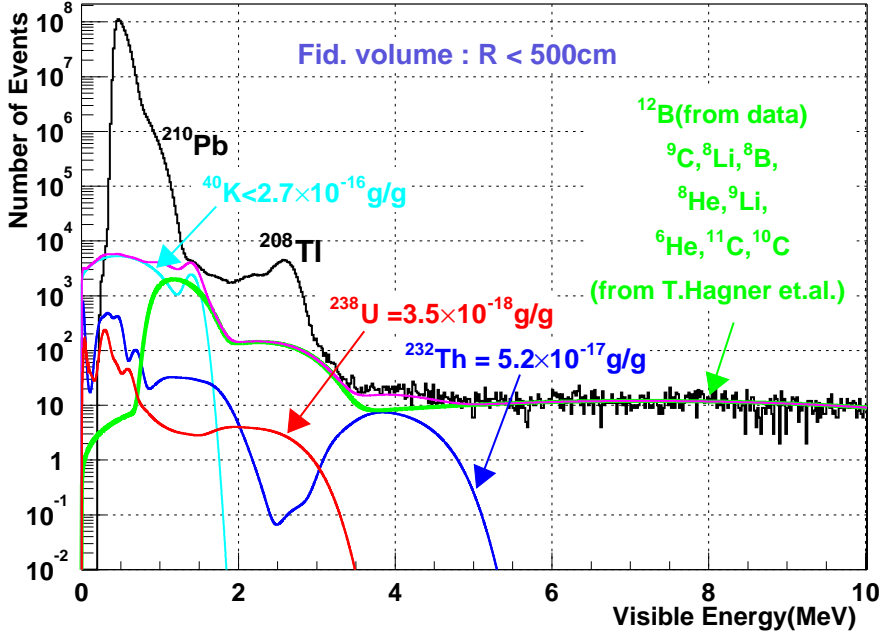


Figure 5.13: Energy spectrum with the fiducial volume 5 m and 1.2 m central cylinder cut along the z-axis.

time is simulated as $\sim 212.5 \mu\text{seconds}$. Convoluting a resolution of the vertex fitter as 25 cm, diffusion length and the inefficiency of the delayed signal related to the space cut conditions are shown in Fig.5.14. As the selection criteria for the space correlation of reactor $\bar{\nu}_e$ analysis is determined to be 160 cm, the detection efficiency for coincidence events is found to be 99.0 % from the right figure. The detection efficiency near the edge of the fiducial volume is reduced because fiducial volume cut is applied for both prompt and delayed events, while the central cylinder cut with radius 1.2 m is applied for only delayed events to simplify the calculation of the detection efficiency. Simple calculation for these effects are performed using monte carlo simulation and the total detection efficiency for the space correlation cut is estimated. Fig.5.15 shows the detection efficiency dependence on radius of vertex position. For uniformly distributed events, the histogram shows flat distribution. The deviation from constant is caused by the fiducial edge effect and the central cylinder cut.

From this result, the total detection efficiency of the space correlation is calculated to be 83.61% by integrating all radial dependences in Fig.5.15. Because this result can be varied by changing some input parameters, 2.0% is assigned to the uncertainty for the detection efficiency from the space correlation.

Simulation result for the neutron capture time is compared with the spallation neutron capture time after muon. This spallation neutron is produced by this reaction, $\mu + {}^{12}\text{C} \rightarrow \text{neutron(s)} + \text{nuclei}$. The distribution of capture time is shown in Fig.5.17 and the

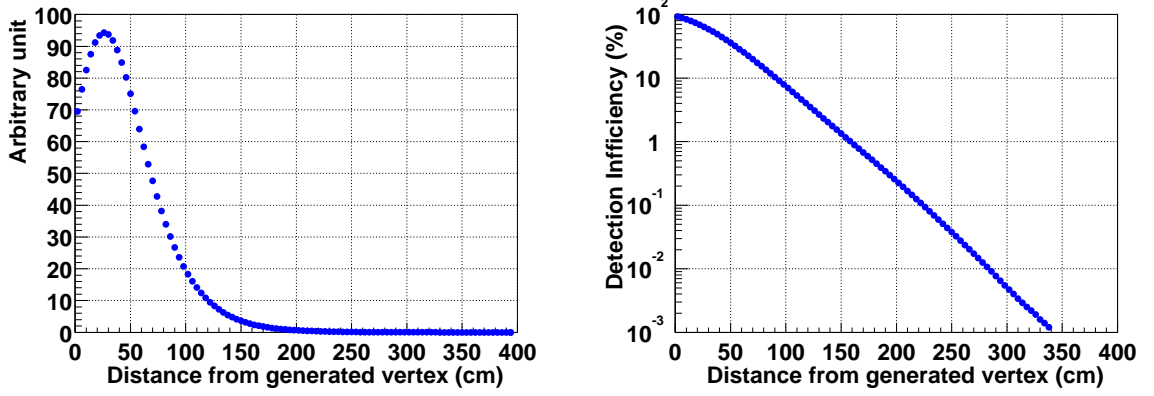


Figure 5.14: The left of the figure indicates the convoluted vertex position of a resolution of the vertex fitter as 25 cm and the mean diffusion length of the 2.22457 MeV γ . The right figure indicates the detection inefficiency curve at each vertex correlation cut.

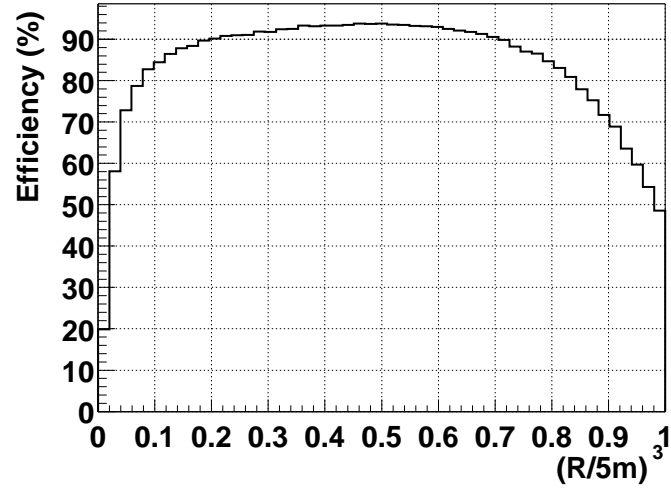


Figure 5.15: The detection efficiency as a function of the event vertex R . The deviation around $(R/5m)^3 \sim 1$ is caused by the fiducial edge effect, and that around $(R/5m)^3 \sim 0$ is caused by the central cylinder cut.

result is $213 \pm 3 \mu\text{seconds}$. This result is in good agreement with the simulation result.

This analysis uses the events with timing correlation being within $0.5 \sim 660 \mu\text{seconds}$. The 0.5μ seconds cut is applied because too close coincidence events ($\sim 200 \text{ ns}$) are detected as one event by KamLAND electronics shown in Fig.5.16. The detection efficiency

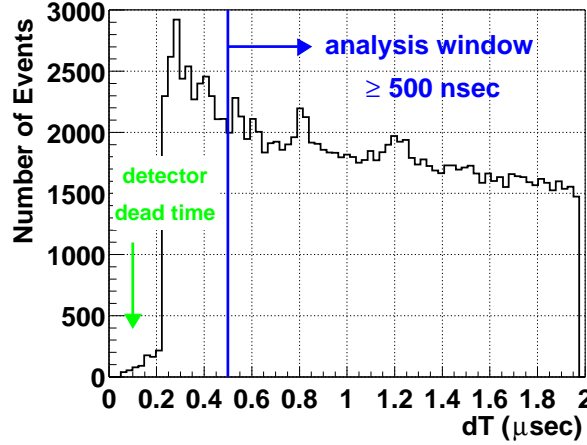


Figure 5.16: The coincidence events from 0μ seconds to 2μ seconds. The events in the time window less than 0.2μ seconds are detected as one events by electronics. So the events after 0.5μ seconds from the prompt event are used for the delayed coincidence events.

of the time window can be calculated to be 95.3 % using $212.5 \mu\text{sec}$ capture time from the simulation. The discrepancy of the capture time between the simulation, spallation neutron data and the AmBe source data is less than 8μ seconds. The uncertainty of the detection efficiency is determined to be 0.2% from the discrepancy.

5.8 Energy Cut

Prompt energy threshold for the reactor $\bar{\nu}_e$ is applied. As described in the trigger efficiency section, the detection efficiency at the 0.9 MeV threshold is 99.98% and the uncertainty is 0.002%, on the other hand, the detection efficiency at the 2.6MeV threshold is 100% and the uncertainty can be negligible. In this thesis, the rate analysis for the reactor $\bar{\nu}_e$ is done. There are geo $\bar{\nu}_e$ events below 2.6 MeV whose flux has not been measured yet. To remove the flux uncertainty of geo $\bar{\nu}_e$, 2.6 MeV energy threshold is applied. Delayed energy window from 1.8 MeV to 2.6 MeV is determined to obtain $\sim 99\%$ detection efficiency and sufficiently low background rate. The detection efficiency of this cut is calculated to be 98.85% considering the resolution of $7.5\%/\sqrt{E(\text{MeV})}$.

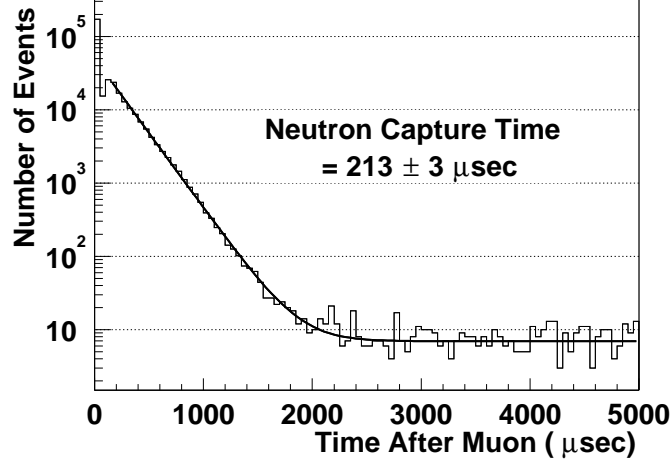


Figure 5.17: The neutron capture time using the muon induced spallation neutron samples. This result is in good agreement with our simulation result.

5.9 Spallation Cut

A cut for the spallation products are applied to the data set after delayed coincidence dependent on the muon charge and the track correlation. Especially, ^8He and ^9Li can be critical backgrounds for the reactor anti-neutrino analysis because these nuclei emit neutron accompanying β decay. These β signal and the following neutron captured γ mimic delayed coincidence $\bar{\nu}_e$ signal.

Total volume is vetoed for 2 seconds for showering muons defined by that the residual charge is larger than ~ 3 GeV (10^6 p.e.), where the residual charge is defined as the difference between the visible energy and expected minimum ionizing energy calculated from path length. Fig.5.18 shows the distribution of the residual charge.

The rate of the showering muons is 0.02 Hz. The dead time due to the all volume cut of showering muons for 2 seconds is calculated to be 4 %. For non-showering muons, tracking cut is applied for 2 seconds. Non-showering muons are defined as the residual charge is less than ~ 3 GeV (10^6 p.e.). The muon tracking cut is defined as the cylinder with radius 3 m around the muon track. This tracking cut is only applied for the delayed events to simplify the calculation of the efficiency of this cut. The corresponding dead volume is calculated for each muon dependent on the distance from detector center to the muon track. Fig.5.19 shows the dead volume dependence on the muon track from the muon tracking cut. For example, if a muon goes through the detector center, ~ 250 m³, corresponding to that the muon distance from center is zero, is vetoed by the tracking cut.

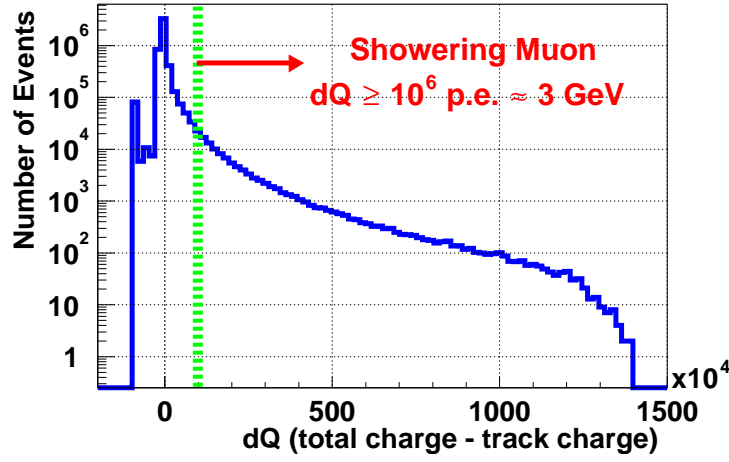


Figure 5.18: The definition of showering muon. Horizontal axis indicates the difference (dQ) between the visible energy and expected minimum ionizing energy calculated from path length. The showering muons are defined as $dQ \geq 10^6$ p.e., corresponding to ~ 3 GeV.

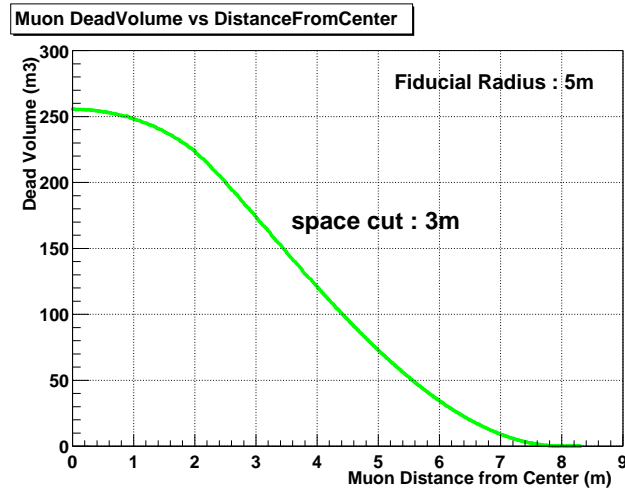


Figure 5.19: The dead volume by the 3 m cylinder cut as a function of the distance from the detector center to the muon track. This dead volume is calculated at each non-showering muon.

Some muons like stopping muons can be reconstructed to the different tracks from real ones. Muon fitter returns the indicator of the validity of muon fitting, called badness. If the values of badness are larger than 100, the tracks reconstructed by the muon fitter can not be used. For this case, we veto all volume for 2 seconds if the charge of muons is larger than 40000 p.e., which almost corresponds to the scintillation muons. There are some muons which are not detected by the detector, for example, the beginning of the run, the electronics dead time during data taking and so on. There are two kinds of electronics dead time. One is known dead time, and the other is unknown dead time. If the trigger becomes the conditions that it cannot collect and send the data, it issues the trigger disable flag, and if recovered, it issues the trigger enable flag. The existence of the electronics dead time can be known by this disable/enable flag. Even though there are no these flags, there can be the case that the time interval between event and event is larger than usual. The history trigger data ($\sim 200\text{Hz}$) is used to know such an unknown dead time. If the time interval is larger than 100 msec, it is supposed there is an unknown dead time. The possibility that such time interval occurs accidentally is negligible. As already explained, KamLAND electronics goes in busy status just after high energy events, such as muons, and several noise events follow these events. These noise events are positively used to search the unknown dead time. If there are at least two noise events for 1 msec and there is no muon before these events, it is supposed that there is an electronics dead time and that the muon is failed to detect. So, the events after these dead times are vetoed for 2 seconds in the whole volume. Including all spallation cut discussed above, the final livetime after spallation cut is obtained to be 145.1 days. Considering the total run time is 163.8 days, 11.4 % of the livetime is vetoed by this spallation cut.

5.10 Final Sample

Table.5.1 summarizes the number of events remaining after each reduction step for low energy events.

Finally, 86 neutrino candidate events at 0.9 MeV threshold and 54 events at 2.6 MeV are remained in our whole data samples of 145.1 days. The various profiles of these events are shown in Fig.5.20 and in Fig.5.21. The prompt energy corresponds to the positron and the delayed energy to the captured neutron. One event at the delayed energy 5 MeV is observed. This event is assumed to be the 4.947 MeV γ event from the neutron captured by ^{12}C . The probability of the ^{12}C captured events is estimated to be 0.5 % relative to that of ^1H captured events. So the expected events of ^{12}C are 0.4 in the whole data samples and are consistent with one event. Lines are the selection criteria and all the cuts except for the cut shown below each figure are applied. A clear cluster of events at each selection is observed, and these $\bar{\nu}_e$ candidate events are well separated from the accidental background events.

Reduction step	Number of remained events
Total events	440765362
Total low energy events	435925737
Noise and Flasher cut	319399135
muon 2ms cut	317591160
fiducial cut	45581117
space and timing cut	343
energy cut	173
spallation cut(0.9MeV)	86
spallation cut(2.6MeV)	54

Table 5.1: The summary of the event selection. The number of events at each step are shown in the table.

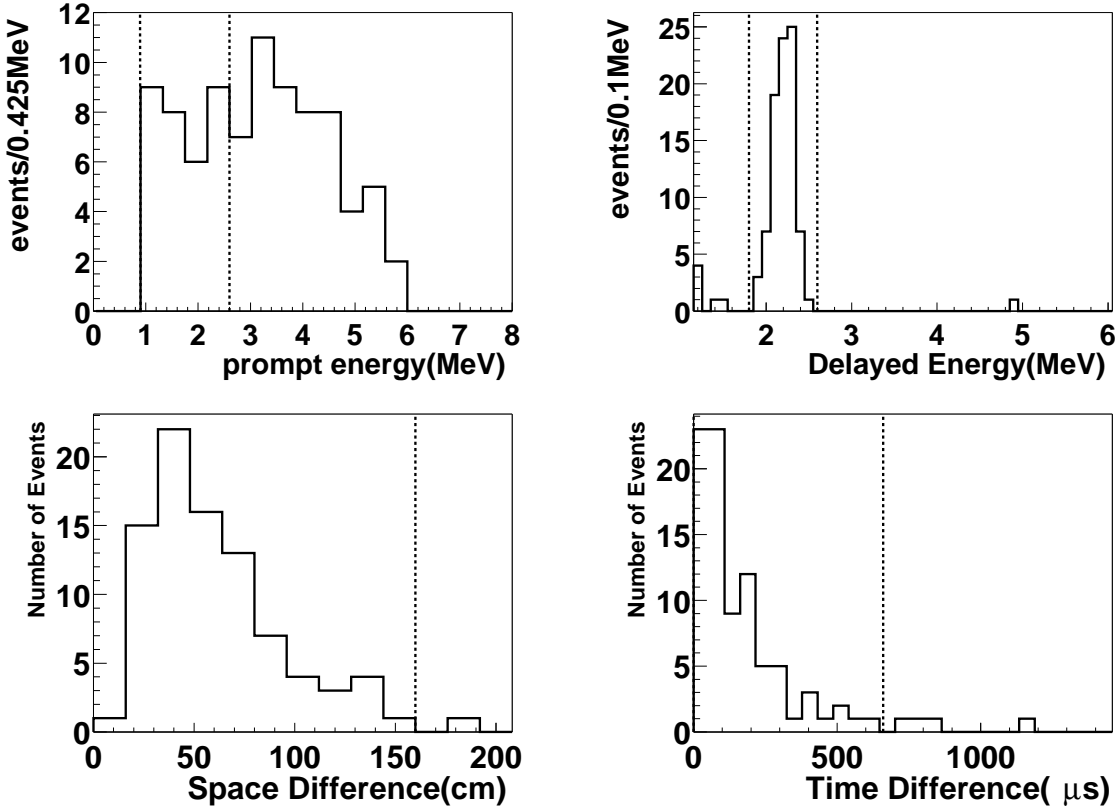


Figure 5.20: The various profiles of $\bar{\nu}_e$ events. Prompt, delayed energy, space and time correlation histograms are shown. Lines are the selection criteria and all the cut except one for each figures are applied.

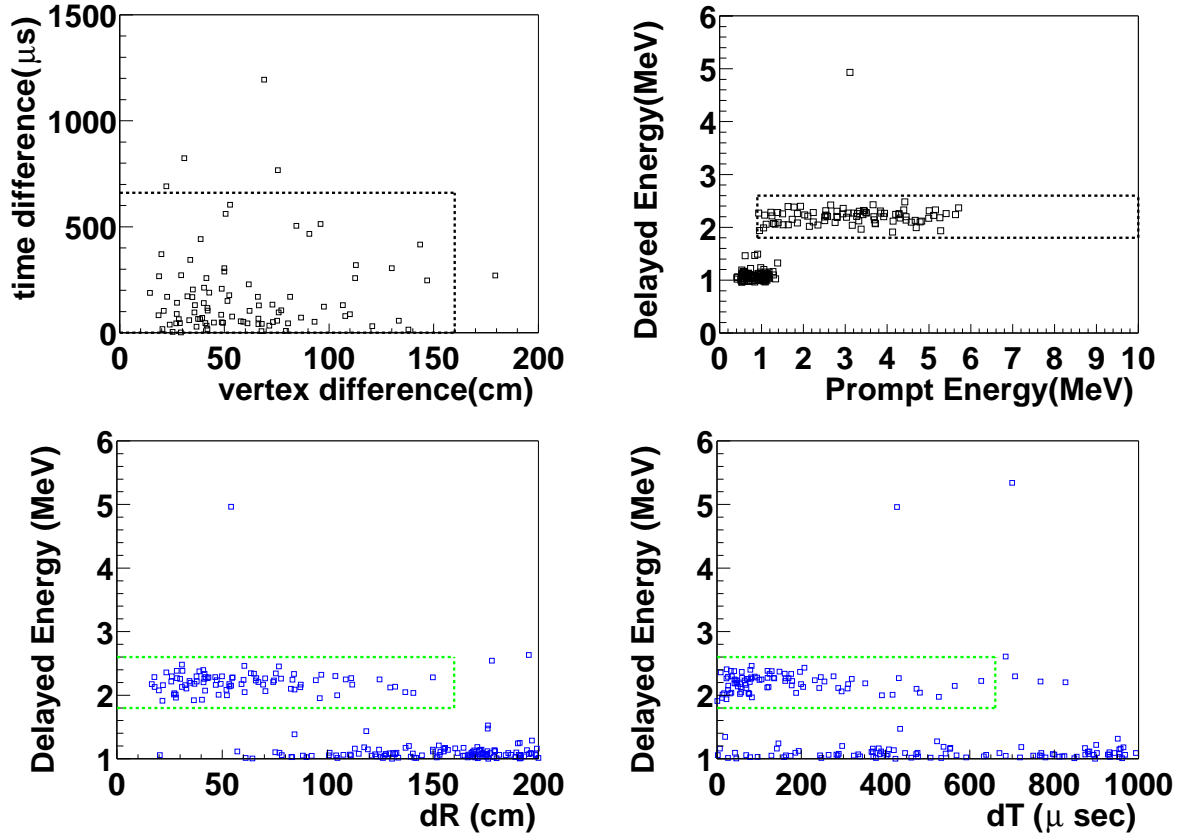


Figure 5.21: Time vs vertex, prompt vs delayed energy, delayed energy vs space correlation and delayed energy vs time correlation are shown. Lines are the selection criteria and all the cut except one for each figures are applied.

Chapter 6

Background Estimation

It is critical issue to estimate the background rates in the disappearance experiment which compares the observed ones. with expected event rates. The flux of the geo neutrino coming from the earth is unknown. The flux measurement of geo $\bar{\nu}_e$ itself, is an important issue for geo physics and neutrino physics. However it has not been measured yet and there is no reliable earth model which predict the flux. The visible energy spectrum from the geo neutrino spreads up to 2.6 MeV. To remove this ambiguity, the energy threshold for the rate analysis are applied at 2.6 MeV.

As the delayed coincidence is used to detect anti-neutrino, there are two different kinds of backgrounds, which are accidental and correlated backgrounds.

In this chapter, the estimation of the background rates for the reactor anti-neutrino analysis in KamLAND at the prompt energy threshold 2.6 MeV are described and the total backgrounds of the reactor anti-neutrino are summarized.

6.1 Accidental Background

The rate of accidental background contamination is estimated by the same cut as the anti-neutrino selection except for the different time window. To reduce the statistical error from the accidental background estimation, a wider time window is used. The used time window for delayed events is between 10 msec to 20 sec after prompt events. The time window later than 10 ms is determined to to remove the neutron capture events which capture time is $\sim 210 \mu\text{sec}$.

Fig.6.1 shows the off-time distribution and energy spectrum of the accidental events. This time distribution is almost flat in the whole region as expected for random coincidence and this rate is extrapolated into the reactor analysis time region of $0.5\mu\text{sec}\sim 660\mu\text{sec}$.

As the result, total accidental events were estimated to be 261 ± 16 events at 2.6MeV threshold in the whole data samples of livetime 145.1 days in time window between 10ms and 20sec. This corresponds to 0.0086 ± 0.0005 events in the reactor anti-neutrino whole data samples. This means that the rate of the accidental background events is (5.9 ± 0.3)

$\times 10^{-5}$ events/day. This accidental background rate is small enough compared with the reactor $\bar{\nu}_e$ event rate (~ 0.6 events/day).

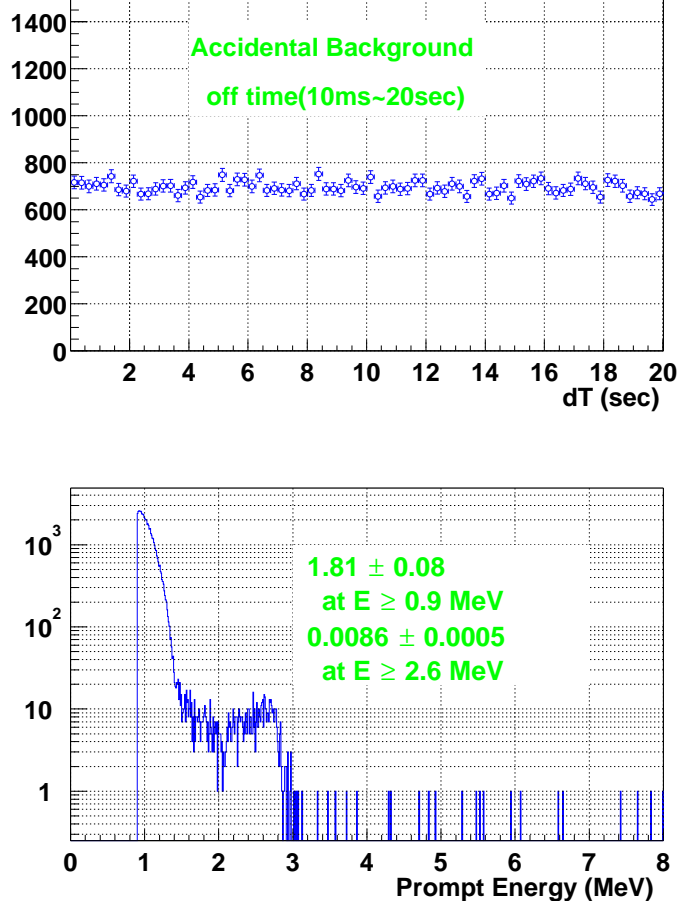


Figure 6.1: Accidental time and energy spectrum at KamLAND detector for reactor neutrino analysis. Time spectrum is flat in the whole time window of 10 ms and 20 sec. This indicates the selected events are surely accidental backgrounds, not correlated backgrounds. Total accidental background rate is 0.0086 ± 0.0005 events at 2.6MeV threshold.

6.2 Correlated Background

6.2.1 Natural Radioactivity

Some kinds of radioactive elements are contaminated in the detector composition. The most critical background sources among them are ^{238}U , ^{232}Th and ^{40}K in the liquid scin-

tillator. From the point of view of the correlated background, ^{238}U and ^{232}Th are more critical because these nuclei have correlated decays in their decay chains.

The requirements for these contamination level in the liquid scintillator are $< 10^{-14}\text{g/g}$ for ^{238}U , ^{232}Th and $< 10^{-15}\text{g/g}$ for ^{40}K for the reactor anti-neutrino analysis.

The concentration of ^{238}U in the KamLAND detector were measured through the decay of its daughters, $^{214}\text{Bi}(\beta) - ^{214}\text{Po}(\alpha)$. That of ^{232}Th were measured through $^{212}\text{Bi}(\beta) - ^{212}\text{Po}(\alpha)$. The decay schemes of these chains are summarized in Table.6.1.

^{214}Bi - ^{214}Po decay chain				^{212}Bi - ^{212}Po decay chain			
Nuclei	decay mode	Energy(Q value) (MeV)	$T_{1/2}$	Nuclei	decay mode	Energy(Q) (MeV)	$T_{1/2}$
^{214}Bi	β^-	3.272	19.9 min.	^{212}Bi	β^-	2.254	61 min.
\Downarrow				\Downarrow			
^{214}Po	α	7.687	164 μ s.	^{212}Po	α	8.784	299 ns
\Downarrow				\Downarrow			
^{210}Pb			22 year	^{208}Pb			stable

Table 6.1: The decay schemes of $^{214}\text{Bi} - ^{214}\text{Po}$ and $^{212}\text{Bi} - ^{212}\text{Po}$ decay chains. β and α delayed coincidences are used for the identifications of both of them.

In order to estimate the background rates for the reactor anti-neutrino analysis, the 5m fiducial cut and 1.2m cylindrical cut which are same as the anti-neutrino ones are applied.

For the estimation of the ^{238}U , ^{232}Th concentration in the liquid scintillator, severer cuts which are 4m fiducial and 2m cylindrical cut, were applied. That is to remove those Rn diffused from outside when calibration devices are deployed or internal materials except for liquid scintillator thoroughly.

Event Selection and Efficiency

The selection criteria for the ^{214}Bi - ^{214}Po and ^{212}Bi - ^{212}Po delayed coincidence events are shown in Table.6.2.

To measure the ^{238}U and ^{232}Th concentrations in the liquid scintillator itself, the 4 m fiducial volume cut for prompt events and the 2 m cylindrical cut (thermometer cut) for delayed events were applied. The R_{xy} in the Table.6.2 means $\sqrt{x^2 + y^2}$, which is the distance of the vertex point from the z-axis. Fig.6.2 shows the selected ^{214}Bi - ^{214}Po events by the above selection criteria. The left figure shows the energy spectrum of prompt ^{214}Bi β and the right one shows delayed ^{214}Po α decays.

The Q value of ^{214}Bi β decay is 3.272MeV and there are many different kinds of levels in ^{214}Po . So the energy spectrum from ^{214}Bi β decays consists of β decay plus several γ s. X-axis shows the visible energy in this analysis. Smooth line shows the expected

Selection criteria	^{214}Bi - ^{214}Po	^{212}Bi - ^{212}Po
Fiducial		
LS contami. (prompt only)	4m	4m
Reactor background(both)	5m	5m
Vertex correlation(dR)	<1m	<1m
Time correlation(dT)	$5 \sim 1000\mu\text{sec}$	$0.4 \sim 1\mu\text{sec}$
Prompt energy	$\geq 1.3\text{MeV}$	$\geq 1.0\text{MeV}$
Delayed energy	$0.3 \sim 1.0\text{MeV}$	$0.3 \sim 1.0\text{MeV}$
thermometer cut (R_{xy})		
LS contami.	>2m	>2m
Reactor background	>1.2m	>1.2m

Table 6.2: Selection criteria for the ^{214}Bi - ^{214}Po and ^{212}Bi - ^{212}Po delayed coincidence events.

visible energy spectrum calculated from all β 's and γ 's summing considering energy scale [44]. The Fermi function of the β decay is also considered [45]. The data points with error bars show the total events within 4 m fiducial volume which is consistent with the expected distribution from ^{214}Bi β decay. The histogram shows the events within 4 m fiducial volume plus 2 m cylinder cut. It is found that most of all events within 4 m fiducial volume are removed by this 2 m cylinder cut, compared with the data points and the histogram. That is, most events are concentrated in the central regions along the z-axis.

The trigger efficiency for the delayed signals is also shown in the right figure. Trigger efficiency for the delayed signal is estimated by pre-scaled data with 50 hits threshold already explained in the section 3.4. The same method is used to estimate prompt trigger efficiency, by dividing NsumMax larger than 120 with total number of events. The efficiency is almost 100% at whole energy region for α spectrum and the total efficiency of α detection was found to be 99.74% by convoluting efficiency curve and α spectra. The α peak was reconstructed to be 587 keV. α Quenching factor at 7687keV was calculated to be 13.1. The resolution of this energy range is $6.7\%/\sqrt{E(\text{MeV})}$.

Fig.6.3 shows the energy spectrum of selected ^{212}Bi - ^{212}Po events by the above selection criteria without the fiducial volume. ^{212}Bi - ^{212}Po events are very few, so events in all volume are shown by the data with error bars. The events with fiducial and cylinder cut are also shown by the histogram in that figure. The left figure shows the energy spectrum of prompt ^{212}Bi β decay and the right one shows that of delayed ^{212}Po α decay. The Q value of ^{212}Bi β decay is 2.254 MeV and there are many different kinds of levels in ^{212}Po . Smooth line shows the expected visible energy spectrum. The total detection efficiency of this α spectra was found to be 100 % by convoluting efficiency curve and α spectra. The α peak was reconstructed to be 751 keV. α quenching factor at 8784 keV was calculated to be 11.7. It is shown that α quenching factor depends on the energy losses of incident

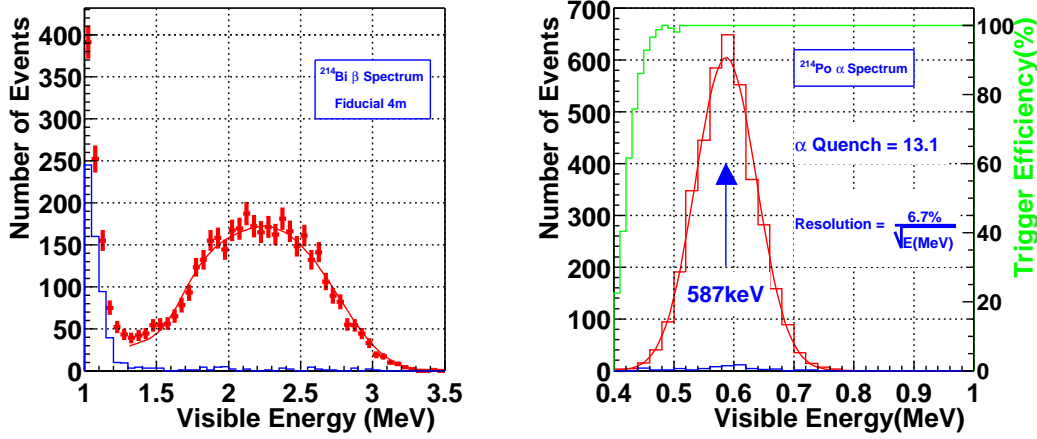


Figure 6.2: Energy spectrum of ^{214}Bi - ^{214}Po coincidence events. Left figure indicates prompt ^{214}Bi β decay. Data points indicate the events within 4 m fiducial volume and blue histogram indicates the events within 4 m fiducial volume plus 2 m cylinder cut. Right figure indicates delayed ^{214}Po α decay. X-axes of both figures indicate the visible energy. The green histogram of the right figure indicates the trigger efficiency curve of delayed signal.

particles. As the events with higher energy have smaller energy loss per unit length, the quenching factor becomes smaller. Birks formula is expressed as

$$\frac{dL}{dx} = L_0 \frac{dE/dx}{1 + k_B dE/dx},$$

where L is the luminescence, L_0 is the luminescence at low specific ionization density, and k_B is Birks constant. As the energy loss is inversely proportional to the momentum square, that of the particle with small energy is larger than that with large energy. Scintillation light from the large energy loss particle, corresponding to the small momentum particle, is much suppressed. These quenching results of 13.1 at 7.687 MeV and of 11.7 at 8.784 MeV are consistent with this energy loss relation.

Fig.6.4 shows the decay time spectrum and the vertex distribution of ^{214}Bi - ^{214}Po events. True lifetime of ^{214}Po is 237 μsec and the fitted value is $223 \pm 7 \mu\text{sec}$. From this result, the systematic error for the detection efficiency is estimated as 0.3%. The vertex distribution indicates that the concentration of Radon is high near the balloon surface and along z-axis. As already explained, three thermometers and their cables along the z-axis are installed into the detector. Furthermore, there are some calibration runs along z-axis. Due to those reasons, the radon concentration along the z-axis becomes high.

Fig.6.5 shows the decay time spectrum and the vertex distribution of ^{212}Bi - ^{212}Po

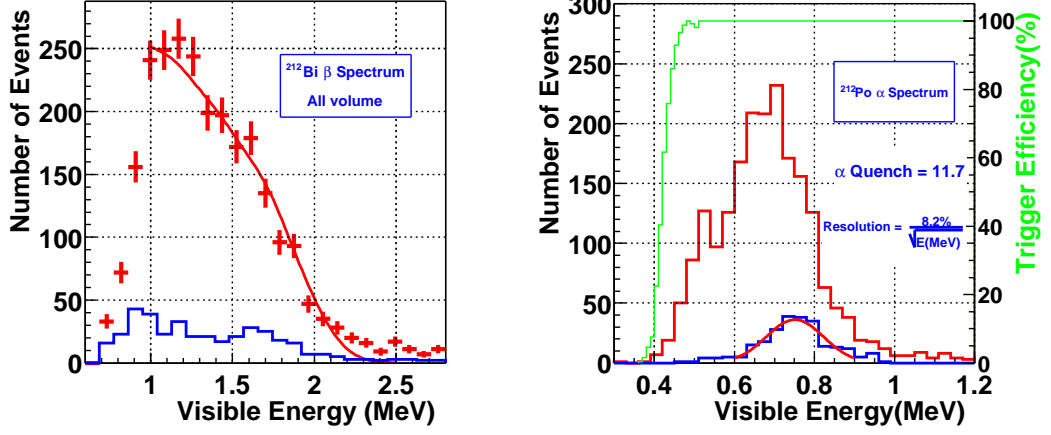


Figure 6.3: Energy spectrum of ^{212}Bi - ^{212}Po coincidence events. Left figure indicates the prompt ^{212}Bi β decay and right figure indicates the delayed ^{212}Po α decay. X-axes of both figures indicate the visible energy. The green histogram of the right figure shows the trigger efficiency of delayed signal.

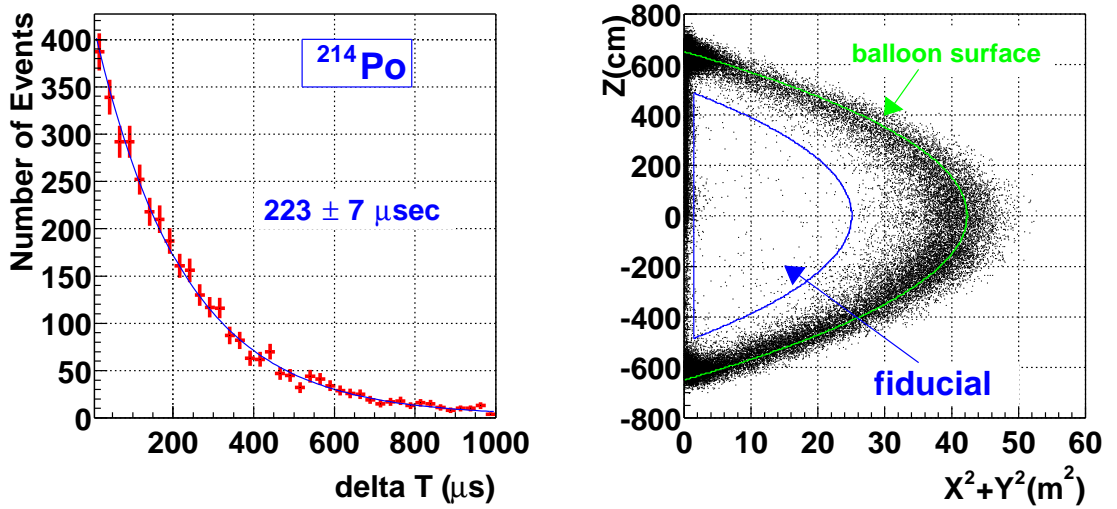


Figure 6.4: Time distribution and the vertex distribution of the ^{214}Bi - ^{214}Po coincidence events. Left figure indicates the time difference of this coincidence events which corresponds to the ^{214}Po decay time. Right figure indicates the vertex position of prompt ^{214}Bi β decay. Horizontal axis indicates the $X^2 + Y^2$ (m^2) and vertical axis indicates the Z (m). As can be seen, the top, bottom, balloon surface and z-axis has higher radon content.

events. True lifetime of ^{212}Po is 431 ns and the fit value is 426 ± 18 ns. From this result, the systematic error for the detection efficiency is estimated as 0.7 %. The vertex distribution indicates the concentration of thorium is high near the balloon surface and top, bottom of the detector. The event rate from thorium along the z-axis is less than those from radon.

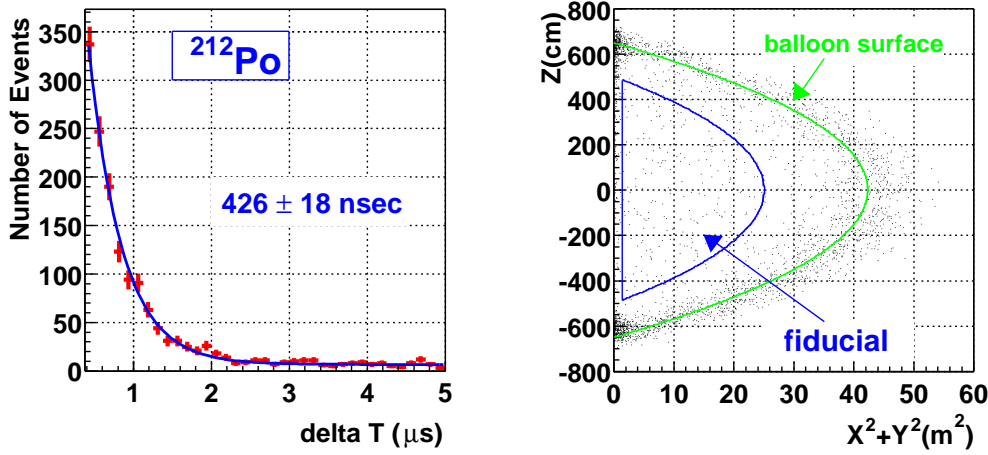


Figure 6.5: Time and vertex distribution of the ^{212}Bi - ^{212}Po coincidence events. Left figure indicates the time difference of this coincidence events and corresponds to the ^{212}Po decay time. Right figure indicates the vertex position of prompt ^{212}Bi β decay. As can be seen, the top, bottom and balloon surface have higher thorium contents.

Fig.6.6 shows the distribution of the distance between ^{214}Bi - ^{214}Po events. The events in the region from about 1.5m to 3m are accidental backgrounds. From this figure, the detection efficiency of the vertex correlation $dR \leq 100\text{cm}$ is estimated to be 84 ± 3 % (statistical error). Because the distance distribution between ^{212}Bi - ^{212}Po events are expected to be same as that of ^{214}Bi - ^{214}Po , the same detection efficiency of $84 \pm 3\%$ is used for the ^{212}Bi - ^{212}Po , too.

The detection efficiency of ^{214}Bi - ^{214}Po events is summarized in the Table 6.3 and that of ^{212}Bi - ^{212}Po is summarized in the Table 6.4.

radioactivity in the liquid scintillator

In this section, the radioactivity measurements of ^{238}U , ^{232}Th contaminated in the liquid scintillator are explained. As already described, the $^{214}\text{Bi}(\beta)$ - $^{214}\text{Po}(\alpha)$ and $^{212}\text{Bi}(\beta)$ - $^{212}\text{Po}(\alpha)$ decay chains are used for the estimations of these radioactivity.

The detector sealing was not perfect during filling the liquid scintillator into KamLAND detector and the liquid scintillator circulation just after that, and some amount of

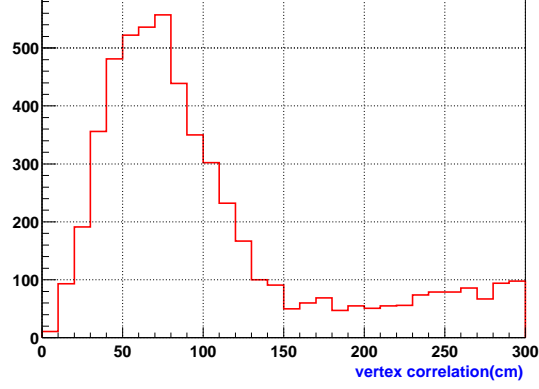


Figure 6.6: The vertex correlation of ^{214}Bi - ^{214}Po events. The events in the region from 1.5 to 3 m are accidental backgrounds. To estimate the detection efficiency of the vertex correlation cut ($dR < 100 \text{ cm}$), the rate of the background is subtracted.

^{214}Bi - ^{214}Po	Efficiency	Systematic
$dR \leq 1\text{m}$	0.84	0.03
$5\mu\text{sec} \leq dT \leq 1000\mu\text{sec}$	0.964	0.003
prompt energy $\geq 1.3\text{MeV}$	0.90	0.015
$0.3\text{MeV} \leq \text{delayed energy} \leq 1.0\text{MeV}$	0.9974	—
summary	0.727	0.034

Table 6.3: Summary of the detection efficiency and the systematic error of the ^{214}Bi - ^{214}Po events.

^{212}Bi - ^{212}Po	Efficiency	Systematic
$dR \leq 1\text{m}$	0.84	0.03
$0.4\mu\text{sec} \leq dT \leq 1\mu\text{sec}$	0.297	0.007
prompt energy $\geq 1.0\text{MeV}$	0.449	0.012
$0.3\text{MeV} \leq \text{delayed energy} \leq 1.0\text{MeV}$	1.0	—
summary	0.112	0.033

Table 6.4: Summary of the detection efficiency and the systematic error of the ^{212}Bi - ^{212}Po events.

radon came into the detector. The circulation process was stopped at the end of November 2001 and the detector was sealed. Data set for the reactor $\bar{\nu}_e$ analysis is from March 4th to Oct 6th in 2002. There were 4 months between the detector sealing and the beginning of the data analyzed. During that period, the Radon decayed and became $e^{-4\text{months}/5.5\text{days}} \sim 10^{-10}$ levels. Once the concentration of ^{214}Bi - ^{214}Po events are measured, the ^{238}U concentration in the liquid scintillator are calculated from it, assuming radio-equilibrium.

Fig.6.7 shows the results of the coincidence rate of the $^{214}\text{Bi}(\beta)$ - $^{214}\text{Po}(\alpha)$ and $^{212}\text{Bi}(\beta)$ - $^{212}\text{Po}(\alpha)$ as a function of time of whole run period. It was found that these sequential events were stable at the whole period of this data taking. As the total number of selected events is 57 in whole data sample, statistical error was 13%. So the total concentration of ^{238}U in the liquid scintillator itself is measured to be $0.035\mu\text{Bq}/\text{m}^3 = (3.5\pm 0.5)\times 10^{-18}\text{g}/\text{g}$ taking into account the efficiency, statistical and systematic errors. Total concentration of ^{232}Th in liquid scintillator is measured to be $0.17\mu\text{Bq}/\text{m}^3 = (5.2\pm 0.8)\times 10^{-17}\text{g}/\text{g}$.

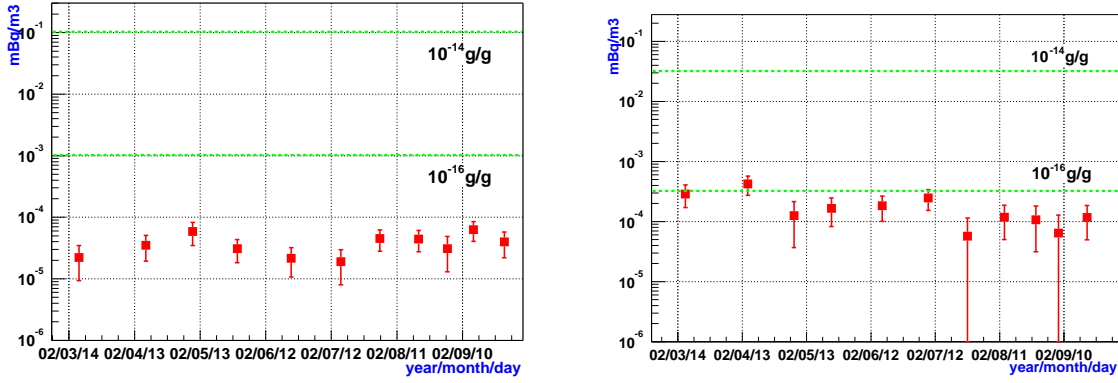


Figure 6.7: Left figure indicates the ^{214}Bi - ^{214}Po event rate dependence on time. Time duration is between March and October, and vertical axis indicates the concentration in unit mBq/m^3 . The content of ^{238}U in the liquid scintillator was determined to be $3.5\times 10^{-18}\text{g}/\text{g}$. Right figure indicates the ^{212}Bi - ^{212}Po event rate dependence on time. Time duration and vertical axis is the same. The content of the ^{232}Th in the liquid scintillator was determined to be $5.2\times 10^{-17}\text{g}/\text{g}$.

These results show that the KamLAND liquid scintillator has the lowest proven U, Th contents in the world.

On the contrary, the central cylindrical region is sometimes contaminated by the diffused radon during some calibration runs. Fig.6.8 shows the radon concentration in the center cylindrical region with radius 1 m as a function of time. The radon concentration is sometimes grown up and decayed by the 5.5 day's decay time which is consistent with that of the ^{222}Rn . The background events from these contaminations can be easily removed by the central cylindrical cut, and these events were very helpful for the calibration of α

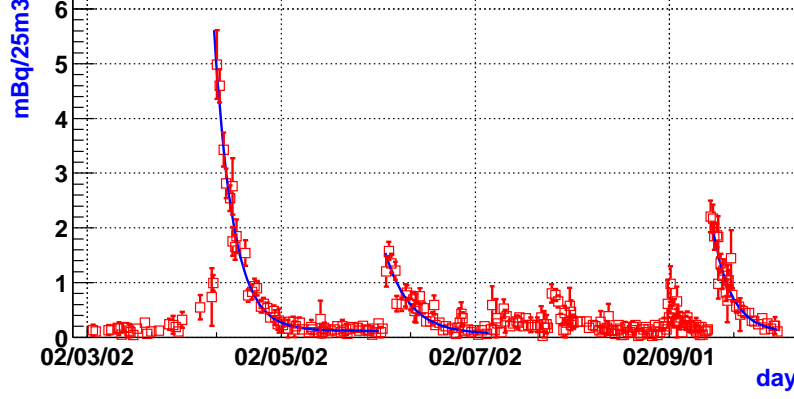


Figure 6.8: Radon concentration in the center cylindrical region with radius 1 m as a function of time.

detection efficiency. As the KamLAND liquid scintillator has few U, Th contents, it would be difficult to demonstrate the identification of α peaks without these contaminations.

Reactor anti-neutrino background

The correlated decay chains in the U, Th decays are possible sources to get into the reactor anti-neutrino selection. The total concentration of radon is $0.09\mu\text{Bq}/\text{m}^3$ in the fiducial volume for reactor anti-neutrino analysis and that of thorium is $0.17\mu\text{Bq}/\text{m}^3$.

First of all, the background contribution from ^{214}Bi - ^{214}Po events are estimated. From Fig.6.2, α peak of ^{214}Po decay which real energy is 7.687MeV are quenched to 586 ± 51 keV. This peak is 24σ apart from our reactor analysis threshold (1.8MeV), and the background rate from this is negligible.

There is another level in ^{214}Po α decay which is 6.9MeV α decay followed by 0.8MeV γ . The branching ratio is 0.01%. As α quenching factor is larger than 13.1 because of the lower energy than 7.687 MeV, total visible energy from $\alpha + \gamma$ decay is estimated to be less than 1327 ± 79 keV. The energy is 6σ apart from the threshold and the reduction factor is estimated to be 10^{-9} . This contribution is negligible, too.

There is another decay chains in ^{238}U decays which is possible source to get into the reactor anti-neutrino samples, that is, ^{214}Pb - ^{214}Bi decay chain. However, the Q value of ^{214}Pb β decay is 1.023MeV and the detection efficiency at the energy threshold ≥ 2.6 MeV is zero. So, for the 2.6 MeV threshold, the background contributions from the ^{238}U are negligible.

Secondary, the background rates from the ^{232}Th contribution are estimated. ^{212}Bi - ^{212}Po events from ^{232}Th can be the background source for $\bar{\nu}_e$. From Fig.6.3 , α peak of ^{212}Po decay whose real energy is 8.784 MeV are quenched as 738 ± 61 keV and this peak

is 17.4σ apart from delayed threshold 1.8MeV . So, the background from ^{232}Th is also negligible.

6.2.2 Spallation Background

KamLAND is shielded from cosmic ray radiation by 2700 meter water equivalence of rock. The total muon rate measured by KamLAND is 0.34 Hz in inner detector, 0.21 Hz in scintillator region, 0.13 Hz in reactor neutrino fiducial volume.

There are mainly 3 kinds of coincidence backgrounds generated by the cosmic ray muons. One is from “knock-off” neutrons which are emitted from liquid scintillator nuclei after being hit by muons. The second one is from radioactive elements made by muon spallation. Some of them such as ^8He , ^9Li emit neutron just after β decay and these sequential events mimic delayed coincidence. The lifetimes of those nuclei are several ten to hundred millisecond. A study of the production cross-section of these nuclei was performed using SPS muon beam at CERN[46]. The energy dependence of the cross section was measured at two muon energies 100 and 190GeV. Based on the measured cross-sections, the muon-induced background rates for the Borexino and KamLAND were calculated. From that, the total production rates of $^8\text{He} + ^9\text{Li}$ are estimated to be $2.4 \pm 0.5/\text{day/kton}$ in KamLAND detector. The half lifetime of ^8He is 119ms and that of ^9Li is 178ms and the branching ratio that emits neutron of ^8He is 16% and that of ^9Li is 48%. Suppose all isotopes are ^9Li (this isotope is more dangerous for the reactor anti-neutrino analysis because this has a longer lifetime and higher branching ratio of neutron emission). The event rate of correlated background from this isotope is calculated to be 0.5/day in our fiducial volume without any cut. This correlated background rate is not small compared with the event rates of reactor anti-neutrino of 1.1/day, so this event must be rejected by some cuts. Mainly two cuts are used, one is all volume cut for the showering muons and the other one is 3 m cylindrical cut along the muon track for non-showering muons. Both cuts are applied for 2 seconds. The background rates after these cuts are described in this chapter.

The last one is the fast neutron produced by cosmic-ray muon going through anti counter or the rock surrounding the detector. Fast neutrons mimic delayed coincidence because it interacts proton and the recoiled proton emits scintillation light and the neutron are finally captured by proton and emits $2.22\text{MeV } \gamma$. This correlated event rates are estimated in the next section.

Spallation neutron

As already shown in Fig.5.17, the neutron capture time is about $213 \mu\text{sec}$. The total production rate of those neutrons in KamLAND is estimated to be $3060 \pm 150 \text{ events / day / kton}$ from the fitting result of Fig.5.17. We veto the total volume of KamLAND detector for 2 msec after muon going through inner detector. This cut reduces these

neutrons by 8.0×10^{-5} in our whole data sample and the single rate of these neutrons after this cut becomes 0.1/d/408.5ton. So the rate of the background events that the two neutrons are accidentally captured at more than 2msec later than muon are negligible. The dead time by this cut is about 0.07%.

^8He and ^9Li

There are several nuclei from ^{12}C in the liquid scintillator produced by interaction with cosmic ray muons which emit neutron after β decays as shown in Table.6.5.

isotope	production reaction	half-life (msec)	decay mode	energy (MeV)	fraction of decays
^8He	$^{12}\text{C}(\gamma, 4p), ^{12}\text{C}(\pi^-, n3p)$	119	β^-	10.7	0.84
			$\beta^- + n$		0.16
^9Li	$^{12}\text{C}(\gamma, 3p), ^{12}\text{C}(\pi^-, n2p)$	178	β^-	13.6	0.52
			$\beta^- + n$		0.48
^{11}Li	$^{12}\text{C}(\gamma, 2\pi^+p), ^{12}\text{C}(\pi^-, \pi^+p)$	8.5	β^-	20.6	0.07
			$\beta^- + xn$		0.92
^{12}Be	$^{12}\text{C}(\gamma, 2\pi^+), ^{12}\text{C}(\pi^-, \pi^+)$	11.4	β^-	11.7	—
			$\beta^- + n$		—

Table 6.5: summary of the nuclei which emit neutron after β decays which mimic delayed coincidence signal. These nuclei are produced by the interaction between cosmic ray muons and the ^{12}C in the liquid scintillator.

The isotopes with long lifetime are more critical for delayed coincidence analysis, because backgrounds from the shorter-lived isotopes are easily removed by the spallation cut.

The selection criteria for these isotopes are same one as that of anti-neutrino without the spallation cut. Prompt energy spectrum is shown in the left of Fig.6.9, and the delayed energy spectrum is right of that. The blue line of left figure shows the theoretical line of ^9Li β decay. From this figure, dominant source from the neutron emitter is ^9Li . Delayed energy spectrum is fit by the Gaussian, and the resulting 2.22 ± 0.02 MeV is consistent with neutron captured γ .

Next, we study the decay time of the ^9Li nuclei and the contribution of these backgrounds within the reactor anti-neutrino samples are estimated. $^8\text{He}/^9\text{Li}$ samples are divided into two cases, showering and non-showering muon induced events. Showering μ is defined as such that the residual charge of muons is larger than 10^6 p.e. and non-showering μ is defined the residual charge of muon is less than 10^6 p.e. As these elements are mainly produced by showering muons, the cut condition for those is more severe. Total volumes are vetoed for 2 seconds. On the other hand, 3 m cylindrical cut along to

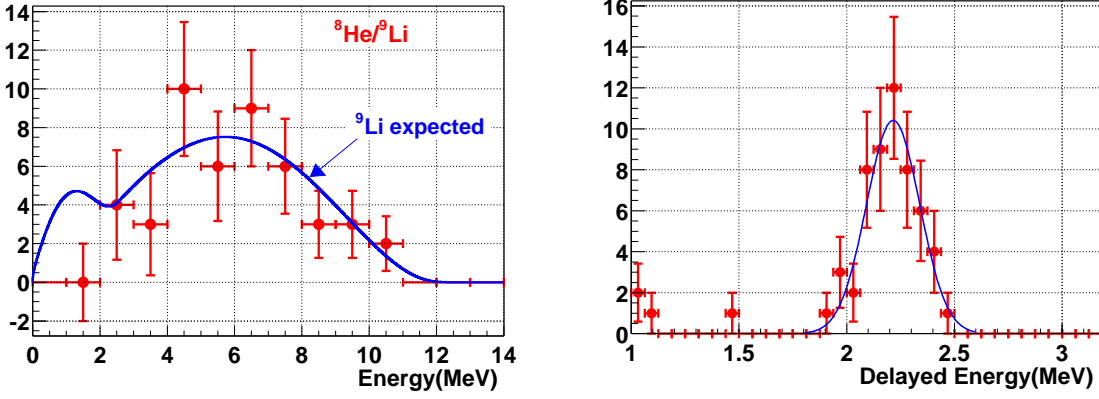


Figure 6.9: $^8\text{He}/^9\text{Li}$ energy spectrum. Left figure shows the prompt energy spectrum and right one shows the delayed energy spectrum.

the muon track for non-showering muons are applied for 2 seconds. The reduction factor of the 2 second veto is 4.1×10^{-4} .

Fig.6.10 shows the decay time distribution of the two cases. Left figure shows the time distribution for showering muon in fiducial volume and right figure shows that for non-showering muons with the distance within 3 m from the muon track. As clearly shown, the event rate from showering muons is more than that of non-showering ones. These data are fit by exponential function plus constant background and decay time is fixed to ^9Li lifetime as shown by the solid line. The two dashed lines in the right figure show the 90% confidence level.

Total events from showering muons are estimated to be 55 ± 8 , and those from non-showering muons are 16 ± 14 . The total events of remained backgrounds for both of these cases are 0.02 and 0.007 respectively per whole data samples.

Most severe background from these elements remained from the spallation cut is the case that residual charge of muon is less than 10^6 and the distance from the muon track is larger than 3 m. The background rates of this case are estimated by using tracking efficiency of the muon fitter. The left figure of Fig.6.11 shows the muon tracking efficiency result by using spallation neutron samples for non-showering muon. The efficiency of the muon tracking within 3 m is estimated to be 93.6%. This means 6.4% of total spallation events remains after this spallation cut. At last, the remained background rates from these elements are estimated to be $(16 \pm 14) \times 0.064 / 0.936 = 1.1 \pm 1.0$ per whole data samples. The event rate at the 2.6 MeV energy threshold is calculated from 0.9 MeV threshold result by using the expected energy spectrum. 85 % of the total events are contaminated into the energy threshold 2.6 MeV, and the 0.94 ± 0.85 events from $^8\text{He}/^9\text{Li}$ are estimated to be contained in our whole data samples.

The right figure of Fig.6.11 shows the decay time of events from the non-showering

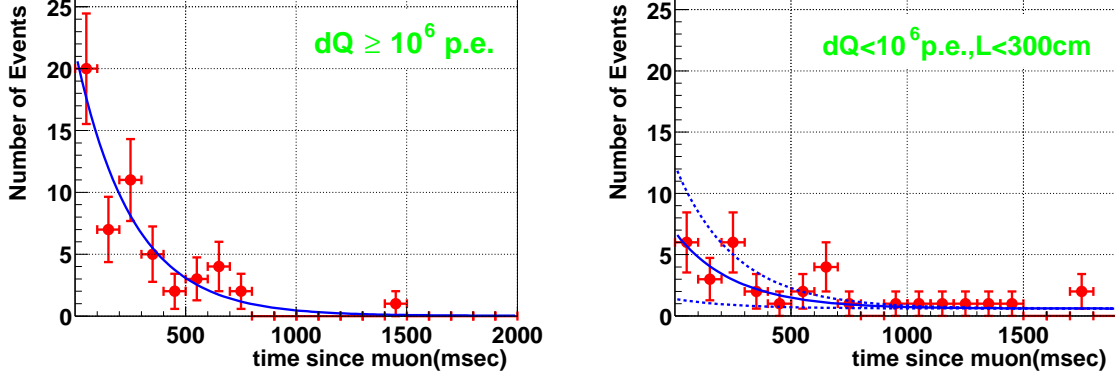


Figure 6.10: Decay time distribution of ${}^8\text{He}$, ${}^9\text{Li}$ samples. The left figure indicates the time distribution for showering muons and the right figure indicates that for non-showering muons with the distance within 3 m from the muon track. The fitting results by the exponential plus constant background function are also shown. The decay time is fixed to be the lifetime of ${}^9\text{Li}$.

muon with the distance more than 3 m away from the muon track. The solid line is also fitting result and it is consistent with estimated value.

Fast Neutron background

Correlated background rates from the fast neutrons are estimated in this section. First of all, the number of fast neutrons generated by the muon going through anti counter, is measured. These events are selected by the triple coincidence, which is delayed coincidence of the inner detector plus outer detector hits. Next, that of fast neutrons generated by the muon going through the rock surrounding the KamLAND, is simulated. Neutron production rate is normalized to the measured data. Total background rate from fast neutrons is obtained by summing measured and simulated rates.

The loose selection criteria for the fast neutron search are following. Charge of prompt candidate is between 0 p.e. and 5000 p.e. (15 MeV) and hits of anti PMT is bigger than 5. Energy of delayed candidate is between 1.5 MeV and 3 MeV and time difference between prompt and delayed events is less than 2 mseconds.

For the estimation of reactor anti-neutrino background, a further cut is applied. The difference between prompt and delayed vertex is less than 160cm and the time difference is between $10\mu\text{sec}$ and $660\mu\text{sec}$ and prompt energy is between 0.9MeV and 10MeV. This time cut of $10\mu\text{sec}$ is to remove the contribution of decay electron events from primary muon decay in the buffer region whose lifetime is $2.197\mu\text{sec}$. The efficiency of the time cut for the reactor neutrino sample is 95.6%.

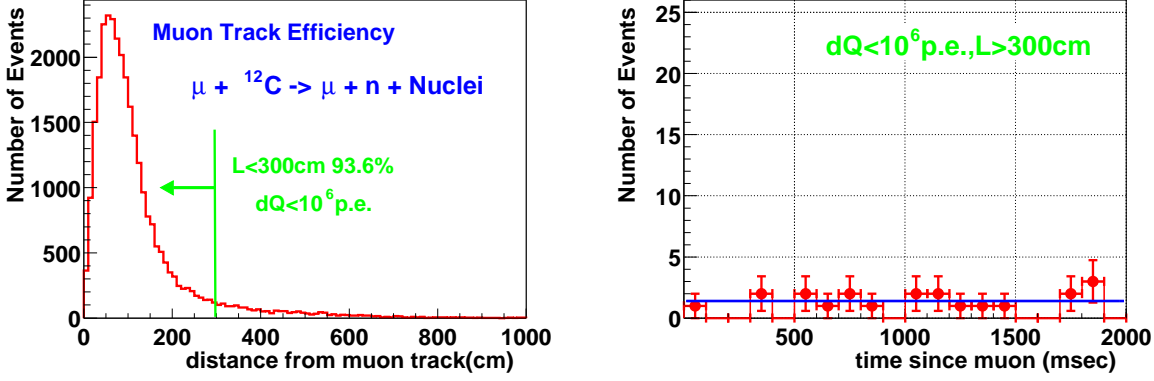


Figure 6.11: The left figure indicates the tracking efficiency of the muon fitter by using the spallation neutron samples for non-showering muons. The right figure indicates the decay time of events from the non-showering muons with the distance more than 3 m away from the muon track.

Figure 6.12 shows the characteristics of the fast neutron events. The upper left figure indicates the time correlation between prompt and delayed signal. The fitted value of capture time is $195 \pm 39 \mu\text{second}$ which is consistent with neutron capture time. The upper right figure indicates the energy spectrum of neutron captured γ signal. The mean energy of these events is 2.14 MeV, slightly lower than the neutron captured γ energy, 2.22 MeV. This is supposed to be that because most of these events occurs outside the fiducial volume, the energy is suppressed. The bottom figure shows the prompt event vertex position as a function of distance from the detector center.

There is no event of fast neutron candidate in the fiducial volume. This R distribution is fit by simple exponential curve, and the possible contamination of the fast neutron background are estimated. The fitting result of the decay length is $40 \pm 8 \text{ cm}$, and that of the total number of events of fast neutrons is 39 ± 6 events. The worst case of this fit are used for the estimation of the fast neutron contamination in the fiducial volume and the result is less than 2 events including the inefficiency of time window per whole data samples. But these 2 events are rejected by our analysis because of OD hits bigger than 5.

On the other hand, the fast neutron from the muon which goes through OD but is not detected by OD because of OD inefficiency can become fake delayed coincidence signal. As anti counter efficiency is 92% in this analysis from OD efficiency study, the fast neutron from no anti data is estimated to be less than 0.17 events.

The fast neutron contribution from rock outside the detector are calculated by simple simulation, and the total ratio of neutron contribution (neutron from muon not going through anti-counter but going through surrounding rock / neutron from muon going

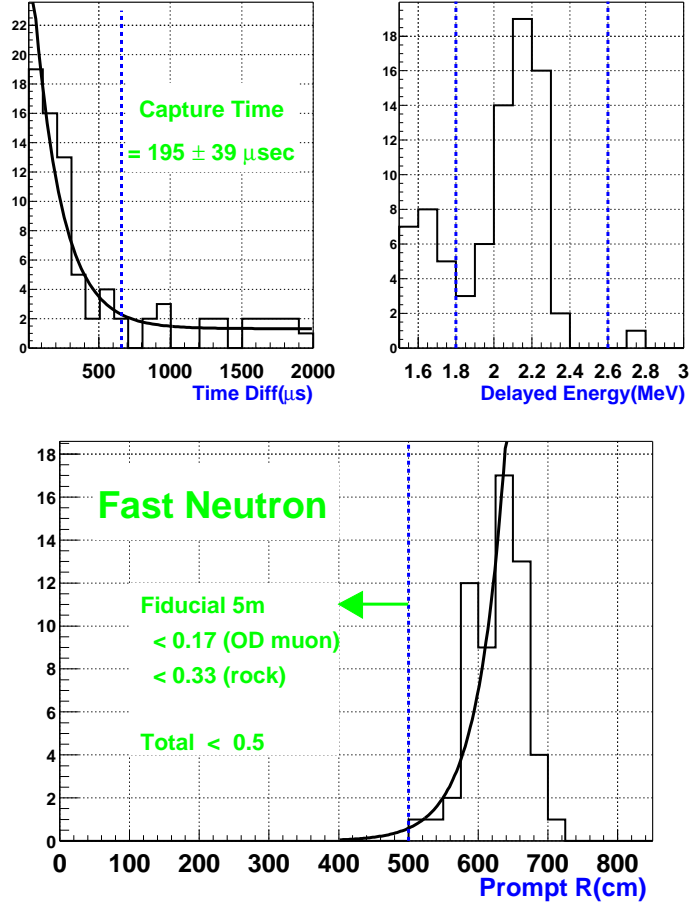


Figure 6.12: The various plots of fast neutron candidates in a 145.1 days sample. The upper left figure shows the time correlation between prompt and delayed signal. The upper right figure shows the energy spectrum of the delayed neutron captured gamma signal. The lower left figure shows the distance from the detector center of the prompt event vertex.

through anti-counter) is 0.11, so the contribution from rock is less than 0.3 events. So the total background events from the fast neutron are estimated to be less than 0.5 in whole data samples conservatively.

The cross section of neutron versus proton is about 300 mb at 30MeV which corresponds to the decay length 7cm in our liquid scintillator and 100 mb at several 100MeV which corresponds to 21cm. As we are now looking at the fast-neutron visible energy of $0 \sim 15$ MeV, the cross section 100 mb can be used to estimate the quantity of the fast neutron that can enter fiducial volume because the fast neutrons with several 100 MeV energy deposit at least several 10 MeV energy into the liquid scintillator. So our fitting result of 40 cm decay length is conservative estimation.

Fig.6.13 shows the energy spectrum of recoiled proton by fast neutrons. The deposit energy is produced via the protons which is recoiled by the fast neutrons. These samples don't indicate any distinctive shapes and are consistent with the flat distribution.

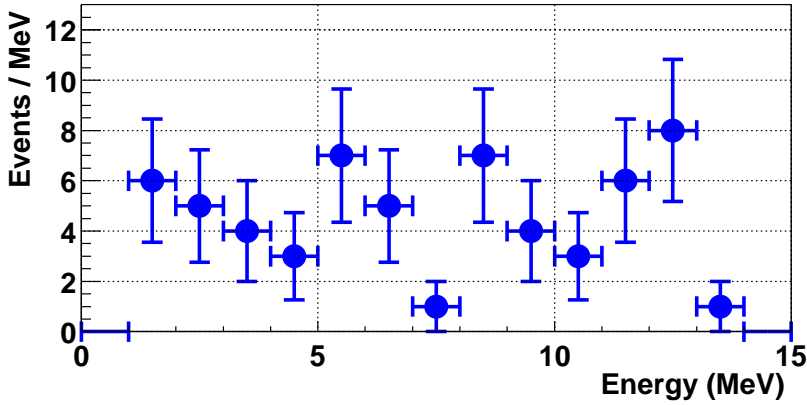


Figure 6.13: Energy spectrum of the protons recoiled by fast neutrons.

6.2.3 Terrestrial Neutrino Background

$\bar{\nu}_e$ emitted by ^{238}U and ^{232}Th decays in the crust and mantle of the earth, called “geo-neutrinos”, contribute low-energy events with $E < 2.6$ MeV. Observation of geo-neutrinos is one of the purposes of our experiment, Here, geo $\bar{\nu}_e$ is treated as “backgrounds” for the reactor $\bar{\nu}_e$ analysis.

The expected geo $\bar{\nu}_e$ energy spectrum [47] is shown in Fig.6.14 together with reactor $\bar{\nu}_e$ spectrum. Two peaks are seen from the geo $\bar{\nu}_e$ events. The peak with higher energy region (> 1.6 MeV) comes from ^{238}U decay chain, and the peak with lower region (< 1.6 MeV) comes from both ^{238}U and ^{232}Th decay chains. This model assumes that the radiogenic heat generation from U and Th is 16 TW, which is $\sim 40\%$ of the observed \sim

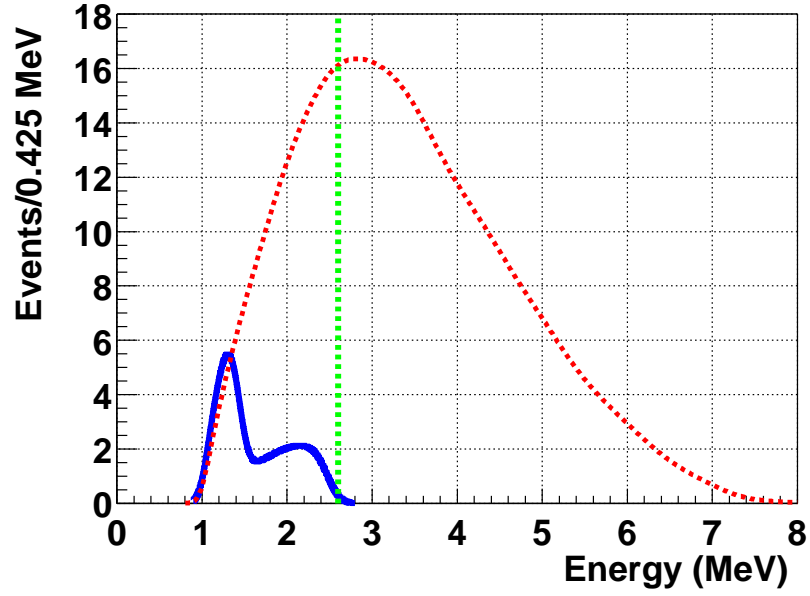


Figure 6.14: Expected geo $\bar{\nu}_e$ energy spectrum. The model of this expected geo-neutrino was taken from the Ref.[48]. Solid smooth line indicates the expected geo $\bar{\nu}_e$ energy spectrum. Dash smooth line indicates the expected reactor spectrum without oscillation for reference. Dash line indicates the energy threshold 2.6 MeV.

40 TW heat outflow on the earth's surface. Models of the earth disperse $\sim 50\%$ of the total U, Th in the mantle (~ 2900 km thick) and concentrate the other $\sim 50\%$ in a thin, ~ 35 km crust under the continents. The oceanic crust is much thinner (~ 6.5 km) with a much smaller ($\times 1/20$) U, Th abundance. The Th/U ratio is adopted here as 4, and it could be altered by differences in the segregation chemistry of U and Th during the evolution of the earth's mantle and crust.

At whole energy regions, ~ 9 geo $\bar{\nu}_e$ events are expected in our data set. However, the abundances of U and Th and their distributions in the earth are not well known. To avoid ambiguities from geo $\bar{\nu}_e$'s, a prompt energy cut, $E_{\text{prompt}} > 2.6$ MeV is employed in this analysis. At 2.6 MeV energy cut, the geo $\bar{\nu}_e$ background is estimated to be 0.044 events in whole data samples. These events are considered as the uncertainty of the background event rate.

A natural nuclear fission reactor with a power output of 3 to 10 Terawatt at the center of the earth has been proposed as the energy source of the earth's magnetic field [48]. Suppose there is a fission power 10 TW geo reactor at the center of the earth, the expected $\bar{\nu}_e$ events are estimated to be 10.1 events in whole data sample. The energy spectrum of the geo-reactors is same as the reactor $\bar{\nu}_e$. In the rate analysis, geo-reactor's background are not included because the existence of geo reactors and their fluxes are now unknown. If the rate of the geo reactor's background is subtracted, the significance might become over estimation.

6.2.4 Atmospheric Neutrino Background

Primary cosmic rays strike the nitrogen and oxygen nuclei in the earth's atmosphere and produce a shower of pions and Kaons which subsequently decay as

$$\begin{aligned} p(\alpha) + \text{Nuclei} &\rightarrow \pi^\pm(K^\pm) + X \\ \pi^\pm(K^\pm) &\rightarrow \mu^\pm + \nu_\mu(\bar{\nu}_\mu) \\ \mu^\pm &\rightarrow e^\pm + \nu_e(\bar{\nu}_e) + \bar{\nu}_\mu(\nu_\mu). \end{aligned}$$

The atmospheric neutrinos therefore consist of electron and muon neutrinos and their anti-neutrinos, and the ratio of ν_μ and ν_e is expected to be 2. The $\bar{\nu}_e$ events from the atmospheric neutrinos at the low energy regions such as several MeV for the reactor anti-neutrino analysis must be estimated. There are many uncertainties for the atmospheric neutrino flux calculations at low energy regions, such as primary cosmic ray fluxes, geomagnetic cutoff, hadron interaction and geometry. The conservative background rates of the atmospheric neutrinos are estimated by several flux calculation models. The base model for the estimation of the atmospheric neutrino flux is BGS [49]. This model is calculated at the energy range from 2 MeV to 3 GeV. This model is compared with two different models, HKHM flux [50] and FLUKA flux [51]. BGS and HKHM models are calculated by 1 dimension, and FLUKA is calculated by 3 dimension.

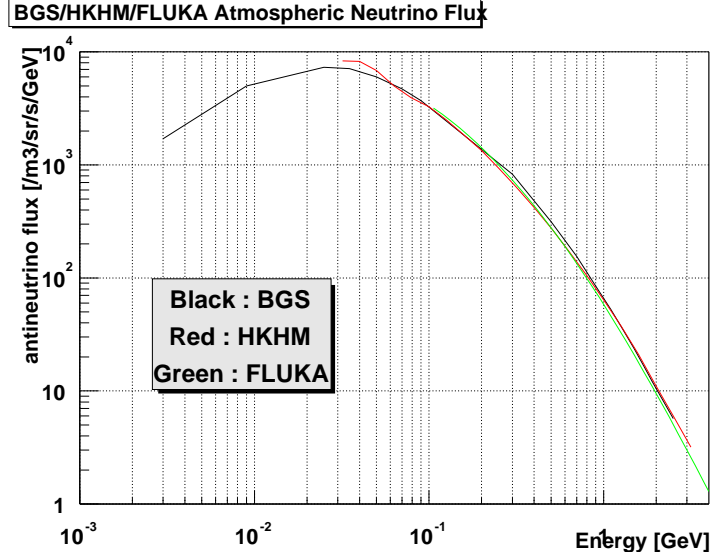


Figure 6.15: Atmospheric anti-neutrino fluxes with different models. The line with the lowest energy is the BGS model [49]. Other two lines are HKHM [50] and FLUKA[51].

Fig.6.15 shows the atmospheric anti-neutrino fluxes with different models. These fluxes have an agreement in $\sim 20\%$. The total event rates at KamLAND between 2 MeV to 10 MeV from atmospheric $\bar{\nu}_e$ is 1.02×10^{-4} events per whole data samples.

6.2.5 Summary

The background event rates for the reactor anti-neutrino analysis are summarized in the Table.6.6. Total background rates at 2.6 MeV threshold except for 10 TW geo reactor

	2.6 MeV threshold
Accidental Background	0.0085 ± 0.0005
$^9\text{Li}/^8\text{He}$	0.94 ± 0.85
Fast Neutron	< 0.5
U	negligible
Th	negligible
Atmospheric $\bar{\nu}_e$	1.02×10^{-4}
Geo $\bar{\nu}_e$ 16 TW	0.044
10TW Geo Reactor $\bar{\nu}_e$	10.1
Total	0.95 ± 0.99

Table 6.6: The summary of the background rates from different sources.

$\bar{\nu}_e$ are estimated to be 0.95 ± 0.99 events in whole data samples. The expected energy spectrum from all the backgrounds is shown in Fig.6.16 together with the reactor $\bar{\nu}_e$.

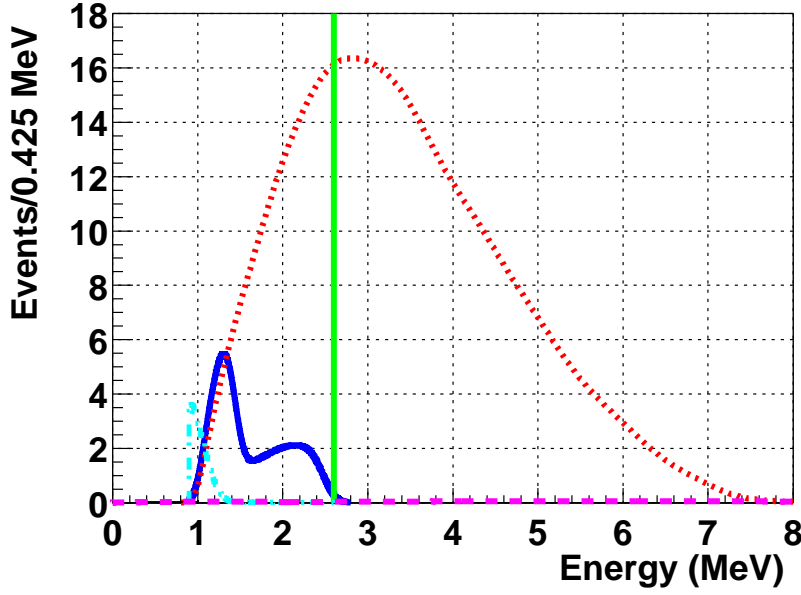


Figure 6.16: The background energy spectrum. The solid line indicates the geo- $\bar{\nu}_e$, dash line indicates the accidental background, dash-dot line indicates the $^8\text{He}/^9\text{Li}$ spectrum and dot line indicates the reactor $\bar{\nu}_e$ spectrum. The energy threshold 2.6 MeV is also shown in the figure.

Chapter 7

Analysis

In this chapter, the estimation of the event rate of the reactor anti-neutrino are described. And after the systematic uncertainties are summarized, the ratio of the observed event rate to the expected one is calculated including detection efficiency, statistical and systematic uncertainties. The consistency of the obtained ratio with no neutrino oscillation model is checked. Assuming neutrino oscillation is real solution for the reactor $\bar{\nu}_e$ disappearance, the allowed region of the oscillation parameter is discussed.

7.1 Expected Reactor Flux

7.1.1 Reactor Distance from KamLAND

Positions of Japanese commercial reactors are provided by TEPCO (The Tokyo Electric Power Company, Incorporated). These data contain the longitude and latitude of TOKYO Datum (the geodetic coordinate Japan standard) of each core of all the reactors. These data are transformed into the global ellipsoidal coordinate system WGS-84 (World Geodetic System - 1984) using simple transformation table [52] similar to tky2wgs [53]. After these data are transformed to WGS-84, the 3-dimensional coordinates (X, Y, Z) of a point are given by the latitude (ϕ), longitude (λ), and ellipsoidal height (H) as,

$$\begin{aligned} X &= (N + H)\cos\phi\cos\lambda, \\ Y &= (N + H)\cos\phi\sin\lambda, \\ Z &= (N(1 - e^2) + H)\sin\phi. \end{aligned}$$

Here, $N = a / \sqrt{1 - e^2\sin^2\phi}$ and $e^2 = f(2-f)$ with a and f representing the equator radius and eccentricity of the ellipsoid, respectively. WGS-84 takes $a=6378137.145$ m and $1/f = 298.257223$.

KamLAND coordinate is read out by the Japanese map with a scale of 1 to 25,000, and the result is following. East longitude is 137.3153, north latitude is 36.4225 and altitude

above sea level is 350m. After transformation of these coordinate to the 3-dimensional coordinates, the distances from the reactor cores to KamLAND are calculated.

The systematic uncertainty of the distance from the reactor to KamLAND is estimated by the comparison of the data from TEPCO with the data of the reactor positions read by the Japanese map with a scale of 1 to 25,000. The discrepancies between these data are found to be within 70 m. The precise measurement of the distance from Super-Kamiokande to KEK with GPS for the K2K experiment was done [54]. This reference describes the coordinates measured by GPS for both KEK and Super-Kamiokande. A GPS position example from this reference was used to check the validity of our method to read Japanese map, KEK 2 (Lat.36°09'12.9247" N, Long.140°04'14.6524" E., H.70.070m) and M1 (Lat.36°26'19.6398" N.,Long.137°16'42.8778" E., H.380.312m) near Super-Kamiokande. This distance between KEK 2 and M1 are calculated to be 252.779 km. This distance from the method reading Japanese map are calculated to be 252.833 km. This result is in good agreement with GPS data, and the discrepancy of those is less than 70 m. This means the total systematic uncertainty from the distance from the reactor core to KamLAND is less than 0.1 %. The detailed distances from the KamLAND to reactor cores and the reactor types are summarized in Table.7.1.

7.1.2 Reactor Thermal Power and Fuel Composition

There are 54 major commercial reactor cores in Japan and 17 reactor cores in Korea. Japanese electric power companies provide the data of thermal power generation and fuel burn up information of each reactor. Using a simple modeling of the reactor core developed by TEPCO SYSTEMS Co.,Ltd. and Tohoku Univ., fission rates of each fuel (^{235}U , ^{238}U , ^{239}Pu and ^{241}Pu) are obtained at each Japanese reactor core. Averaged over the present livetime period, the relative fission yields from the various fuel components are $^{235}\text{U} : ^{238}\text{U} : ^{239}\text{Pu} : ^{241}\text{Pu} = 0.568 : 0.078 : 0.297 : 0.057$. Fig.7.1 shows the total fission fluxes at KamLAND from reactors versus the distances from KamLAND. The contribution of the fission fluxes at the KamLAND is concentrated by the distance around 180 km. The largest contribution is $\sim 31\%$ from Kashiwazaki, whose distance is 160 km, and the closest reactor is Shika, whose distance is 88 km.

The time dependence of the thermal power generation data is checked by comparison with the independent records of electric power generation. The systematic uncertainty assigned to the thermal power is conservatively taken as 2 % from the regulatory specification for safe reactor operation, and that of the chemical composition of fission nuclei in the $\bar{\nu}_e$ flux is less than 1.0 % as explained at the section .

The thermal fluxes from foreign and Japanese research reactors is also considered. The contribution from Korea reactors is 2.46 % and that of other countries and Japanese research reactors is 0.7%. The thermal power operation conditions of Korea reactors can be obtained from the web pages [55]. As the thermal power conditions of other countries and the burn-up effects of other countries and Korea reactors are unknown, the

Reactor Name	Distance(m)	Reactor Type	Reactor Name	Distance(m)	Reactor Type
Kashiwazaki 1	159165.2	BWR	Fukushima1 3	349360.0	BWR
Kashiwazaki 2	159286.5	BWR	Fukushima1 4	349323.4	BWR
Kashiwazaki 3	159396.2	BWR	Fukushima1 5	349576.2	BWR
Kashiwazaki 4	159598.7	BWR	Fukushima1 6	349613.2	BWR
Kashiwazaki 5	160680.4	BWR	Fukushima2 1	345359.9	BWR
Kashiwazaki 6	160580.5	BWR	Fukushima2 2	345416.1	BWR
Kashiwazaki 7	160459.9	BWR	Fukushima2 3	345457.3	BWR
Ohi 1	178703.7	PWR	Fukushima2 4	345490.3	BWR
Ohi 2	178779.2	PWR	Tokai2	295364.0	BWR
Ohi 3	178994.9	PWR	Shimane 1	401065.6	BWR
Ohi 4	179112.7	PWR	Shimane 2	401211.2	BWR
Takahama 1	191196.5	PWR	Onagawa 1	430524.5	BWR
Takahama 2	191227.7	PWR	Onagawa 2	430648.2	BWR
Takahama 3	191639.9	PWR	Onagawa 3	430554.2	BWR
Takahama 4	191671.2	PWR	Ikata 1	560744.2	PWR
Shika	87767.4	BWR	Ikata 2	560799.6	PWR
Tsuruga 1	138425.8	BWR	Ikata 3	560657.3	PWR
Tsuruga 2	138443.2	PWR	Genkai 1	754372.9	PWR
Hamaoka 1	213620.9	BWR	Genkai 2	754483.9	PWR
Hamaoka 2	213696.7	BWR	Genkai 3	754600.1	PWR
Hamaoka 3	213903.2	BWR	Genkai 4	754711.1	PWR
Hamaoka 4	214043.2	BWR	Sendai 1	830331.1	PWR
Mihama 1	145669.0	PWR	Sendai 2	830252.6	PWR
Mihama 2	145719.0	PWR	Tomari 1	783134.7	PWR
Mihama 3	145782.7	PWR	Tomari 2	783016.2	PWR
Fukushima1 1	349447.4	BWR	Fugen	138465.0	ATR
Fukushima1 2	349396.7	BWR	Monju	141461.7	FBR

Table 7.1: Detailed distances from KamLAND to reactor cores and the types of the reactors. PWR, BWR, ATR, and FBR indicate Pressurized Water Reactor, Boiling Water Reactor, Advanced Thermal Reactor, and Fast Breeder Reactor, respectively.

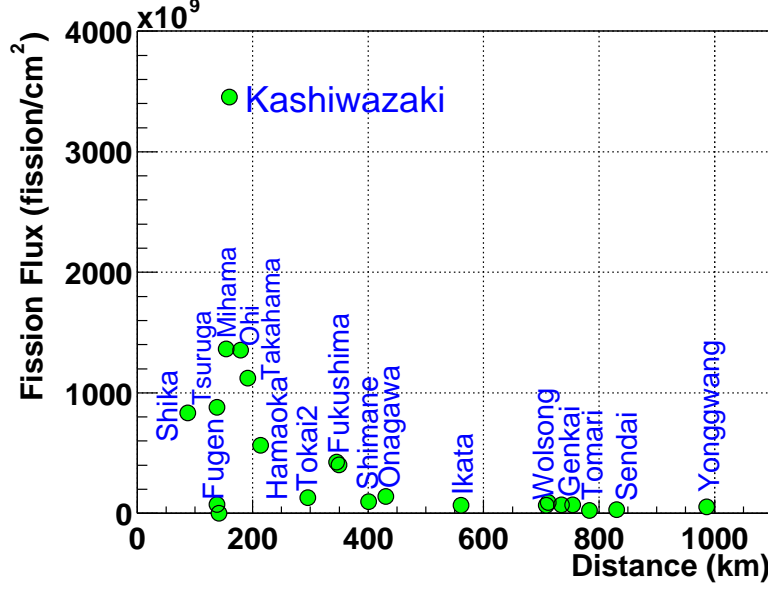


Figure 7.1: Fission flux at KamLAND from each reactor versus the distance to KamLAND.

systematic uncertainties from these $\bar{\nu}_e$ are considered 50% and 10%, respectively. That is, the systematic uncertainties of $\bar{\nu}_e$ from other countries and from Korea are estimated to be 0.35% and 0.3%.

7.1.3 Neutrino Flux from Each Fuel

As shown in Fig.1.7 in 7.1.2, the $\bar{\nu}_e$ energy spectrum generated by each fuel has a different spectrum. The uncertainty of $\bar{\nu}_e$ flux from each fission consists of the measured statistical error and the spectrum conversion error from the β to neutrino, and the uncertainty of $\bar{\nu}_e$ from each fission is obtained by adding these errors in quadrature. In the literature [41], as the 90% CL errors are adopted, these errors are converted to 1σ error. For ^{238}U , no measured spectrum from the fission fragments is available as mentioned before, and the calculated spectrum is used instead. The calculated results for ^{235}U and ^{241}Pu were compared to the measurements and were found to agree within approximately 10%. This is therefore used as an uncertainty in the spectrum of ^{238}U . Fig.7.2 shows the systematic uncertainty of each fission $\bar{\nu}_e$ spectrum. The systematic uncertainty of the neutrino flux from the total fission fragments is calculated to convolute the energy dependence of the uncertainties and the neutrino spectrum after $\bar{\nu}_e p \rightarrow n e^+$ reaction. The ratio of the number of each fission rate is also considered. Finally, 2.48% uncertainty at the 2.6 MeV

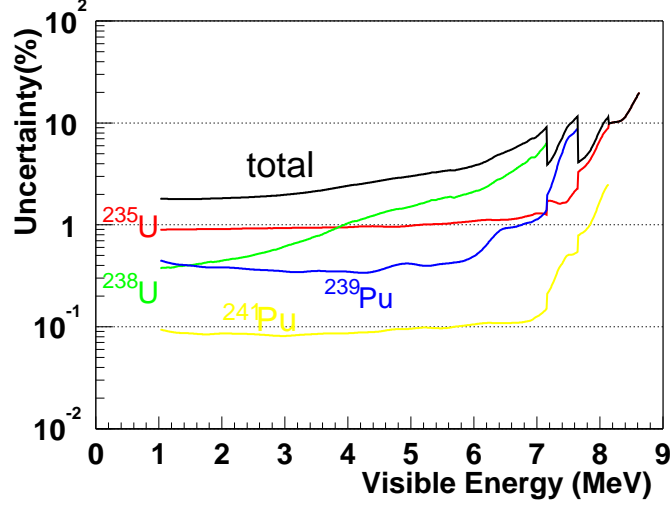


Figure 7.2: Uncertainties of neutrino spectra from four isotopes

threshold is assigned for the neutrino spectra.

7.1.4 Cross-Section

The cross-section of the $\bar{\nu}_e + p \rightarrow n + e^+$ reaction is explained at the section 2.1 and the cross-section as a function of the $\bar{\nu}_e$ energy is shown in Fig.2.1. This calculation includes the coulomb weak magnetism, recoil kinematics and inner and outer radiative corrections, and can be checked by the direct measurement of the neutron lifetime, which is measured to be 885.7 ± 0.8 sec, now. The systematic uncertainty of this reaction is estimated to be 0.2% [56].

7.1.5 Number of Targets

The number of proton targets are calculated by the composition of the liquid scintillator materials and density measurement. The density of KamLAND liquid scintillator was measured daily during liquid scintillator filling into the detector and summed over whole period. The result of the density is 0.77754 ± 0.0001 g/cm³, the error means the one from measurement device. The temperature coefficient of density expansion is measured for KamLAND liquid scintillator, which is 7.41×10^{-4} g/cm³/K. The temperature of the KamLAND liquid scintillator is ~ 11.5 °C. So the density at 11.5 °C is calculated to be 0.78013 g/cm³. Chemical composition of KamLAND liquid scintillator is calculated by the density measurement and daily filling log, N12 : PC = 80.2 : 19.8, and PPO 1.52 g/l. N12 is dodecane, C₁₂H₂₆ and molecular weight is 170. PC is

pseudocumene (1,2,4-Trimethylbenzene), C_9H_{12} and molecular weight is 120. PPO is 2,5-Diphenyloxazole, $C_{15}H_{11}NO$ and molecular weight is 221. From those information, H/C ratio can be calculated, 1.96914. H/N and H/O ratio is also calculable, both 15959.8. After these calculations, the number of proton relative to total weight is simply obtained by this relation,

$$\frac{H}{\text{weight}} = \frac{\text{Avogadro}}{1.00794 + 12.011/(H/C) + 14.00674/(H/N) + 15.9994/(H/O)}$$

After all, the number of protons per kton is calculated to be 8.470×10^{31} / kton. The number of carbons, oxygens and nitrogens are also calculated the 4.302×10^{31} / kton, 5.307×10^{27} / kton and 5.307×10^{27} / kton, respectively. Considering the natural abundance, 1H is calculated to be 8.469×10^{31} / kton, ^{12}C is to be 4.255×10^{31} / kton.

When fiducial volume is 5 m, total volume in the fiducial is 523.599 m^3 , the total weight of the fiducial volume is 408.48 ton by multiplying the density 0.78013 g/cm^3 at 11.5°C . So the total number of free protons in the fiducial volume is estimated to be 3.459×10^{31} .

Systematic uncertainty from the number of target protons is estimated from the temperature uncertainty, which is less than 1.5°C estimated from the time variation and the position dependence of the temperature of the liquid scintillator. That corresponds to be less than 0.1 % of the systematic uncertainty.

During oil filling, the purification system was operated, water extraction and N_2 purging. After N_2 purge, the water contamination into the liquid scintillator were measured to be ~ 30 ppm. From this water (H_2O), the number of H is estimated to be 2.007×10^{27} / kton, that of O is to be 1.004×10^{27} / kton. On the other hand, N_2 is expected to saturate. The saturated value of hexane (247 ppm) are used to estimate the contribution from N_2 , and the number of N is 1.062×10^{28} . O_2 contamination is also measured during oil filling and ~ 20 ppm are expected to be in the liquid scintillator. The expected number of O is 0.753×10^{27} . These are summarized in the Table.7.2.

atoms	the number / kton	nuclei	natural abundance	the number / kton
H	8.470×10^{31}	1H	0.99985	8.469×10^{31}
		2H	0.00015	1.271×10^{28}
C	4.302×10^{31}	^{12}C	0.98900	4.255×10^{31}
		^{13}C	0.01100	4.732×10^{29}
N	1.593×10^{28}	^{14}N	0.99634	1.587×10^{28}
O	7.064×10^{27}	^{16}O	0.99762	7.047×10^{27}

Table 7.2: The summary of the number of atoms in the liquid scintillator.

7.1.6 Neutron Capture on Proton

We select the delayed energy window 1.8 MeV through 2.6 MeV. It means that only neutron captured by proton are detected by inverse- β decay reaction. Other nuclei also absorb neutrons and emit γ s of different energies. Table 7.3 shows the summary of the captured γ energies and the probabilities of different nuclei. The total probability of the

nuclei	cross-section (barn)	energy (MeV)	probability
^1H	0.332	2.22457	1
^2H	0.0005	6.2574	2.26×10^{-7}
^{12}C	0.0034	4.9468	5.15×10^{-3}
^{13}C	0.0009	8.1762	1.51×10^{-5}
^{14}N	0.0750	10.8348	4.23×10^{-5}
^{16}O	0.0002	4.1425	5.01×10^{-8}

Table 7.3: The summary of the energy and the probability of the captured neutron by different nuclei.

neutrons captured by protons is 99.48 %.

7.1.7 $\bar{\nu}_e$ Detection Efficiency

The detection efficiency of $\bar{\nu}_e$ is summarized in the Table.7.4. Total detection efficiency of

	2.6 MeV threshold
Space Correlation	83.61 %
Time Correlation	95.29 %
Trigger Efficiency	—
Delayed Energy	98.85 %
Neutron Capture on Proton	99.48 %
Total	78.3 %

Table 7.4: Summary of the detection efficiency for $\bar{\nu}_e$ delayed coincidence.

$\bar{\nu}_e$ events is estimated to be 78.3 % at the 2.6 MeV threshold. Absolute trigger efficiency is tested by the LED light sources deployed at the center. The LED flashes with a frequency of 147 Hz. The rate of missing events is 0.02%. ^{60}Co source is also used to estimate absolute trigger efficiency. The ^{60}Co activity of 454 ± 14 Bq is measured by the beforehand, and the activity is compared to that measured by KamLAND, 445.3 ± 1.8 Bq. These activities are consistent at the 3% level. Delayed coincidence efficiency is measured using AmBe source. This source emits 4.4 MeV γ -ray and neutron. The

detection efficiency with the space correlation of 160 cm is measured. Fig.7.3 shows the energy spectra of the single events from the AmBe source run. The source deployed position is the detector center, and the events within 1.6 m radius are drawn. 4.44 MeV peak and 7.65 MeV γ s are emitted by the AmBe source. 2.2 MeV peak is the captured neutron signal. To check the detection efficiency of the space cut of 1.6 m radius, the space

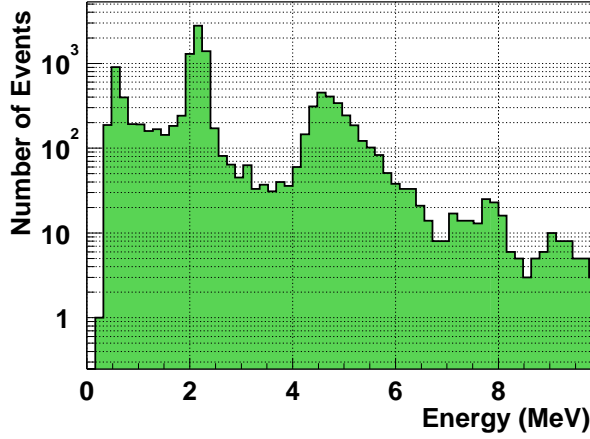


Figure 7.3: Energy spectrum of the AmBe source

correlation of the 4.44 MeV γ -ray and captured neutron signal is measured. Fig.7.4 shows the result of the space correlation. Prompt energy selection is between 4 MeV and 6 MeV, and the time correlation is within 500 μ s and delayed energy is 1.8 MeV to 2.6 MeV. The observed events within 160 cm per total events are $99.2 \pm 1\%$. This result is consistent with the simulation result discussed at section 5.7 at 1% accuracy. Time correlation is also checked and is consistent with the result of simulation, spallation neutron captured time at 4% level.

7.1.8 Expected Reactor Flux

The two-generation survival probability for the $\bar{\nu}_e$ s from each of the reactors i is given by

$$P_i(\bar{\nu}_e \leftrightarrow \bar{\nu}_e) = 1 - \sin^2 2\theta \sin^2 \left(\frac{1.27 \Delta m^2 d_i}{E_\nu} \right)$$

Expected reactor $\bar{\nu}_e$ events are calculated as following in the two-flavor neutrino oscillation scheme,

$$N^{\text{theory}}(E_\nu) = \int dE_\nu \sigma(E_\nu) N_p \sum_i \frac{S_i(E_\nu)}{4\pi d_i^2} P_i(\bar{\nu}_e \leftrightarrow \bar{\nu}_e)$$

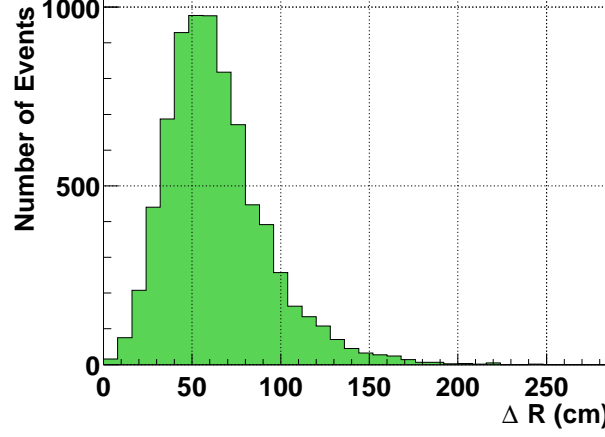


Figure 7.4: Space correlation of 4.44 MeV γ and neutron captured 2.22 MeV γ from AmBe source

where $\sigma(E_\nu)$ is the cross section of $\bar{\nu}_e + p \rightarrow n + e^+$ at the neutrino energy E_ν , $N_p = 3.459 \times 10^{31}$ is the number of free protons in the fiducial volume of the detector explained at the section 7.1.5, $S_i(E_\nu)/(4\pi d_i^2)$ is the expected $\bar{\nu}_e$ flux from the reactor i .

$S_i(E_\nu)$ is written down as,

$$S_i(E_\nu) = \sum_j \left(\int dt f_i^j(t) \right) FS^j(E_\nu)$$

where $f_i^j(t)$ is the fission rate at a given time t at fission nuclei j (^{235}U , ^{238}U , ^{239}Pu and ^{241}Pu), and this fission rate is integrated whole data taking time and is converted to the total fission number of each nuclei, and $FS^j(E_\nu)$ is the $\bar{\nu}_e$ energy spectrum from each fission nuclei per fission explained at section 7.1.3. Finally, the detection efficiency of 78.3 % is multiplied. The expected reactor $\bar{\nu}_e$ energy spectra detected by KamLAND are shown in Fig. 7.5. Solid histogram indicates the expected reactor $\bar{\nu}_e$ energy spectrum without neutrino oscillation. The typical oscillation parameters allowed by the LMA solution are also shown. Dashed histogram indicates the $\Delta m^2 = 5.5 \times 10^{-5} \text{ eV}^2$, dot histogram indicates the $\Delta m^2 = 3.0 \times 10^{-5} \text{ eV}^2$ and dot dashed one indicates the $\Delta m^2 = 1.0 \times 10^{-4} \text{ eV}^2$ and $\sin^2 2\theta = 0.83$. Total events of the expected reactor $\bar{\nu}_e$ are 86.8 events at 2.6 MeV threshold. The integrated ratio observed at the case of the oscillation parameter $\Delta m^2 = 5.5 \times 10^{-5} \text{ eV}^2$ to that of no oscillation at 2.6 MeV threshold is 0.6, $\Delta m^2 = 3.0 \times 10^{-5} \text{ eV}^2$ is 0.36 and $\Delta m^2 = 1.0 \times 10^{-4} \text{ eV}^2$ is 0.58. And also the typical pattern of the energy spectrum for each oscillation parameter is seen.

The ratio of the oscillation spectrum to the no oscillation spectrum is shown in Fig. 7.6. If the spectrum Distorsion is observed at KamLAND, this can be the direct evidence of

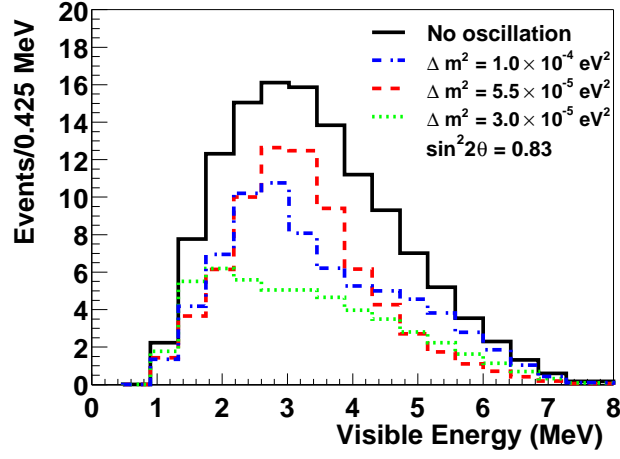


Figure 7.5: Expected reactor $\bar{\nu}_e$ energy spectrum at KamLAND.

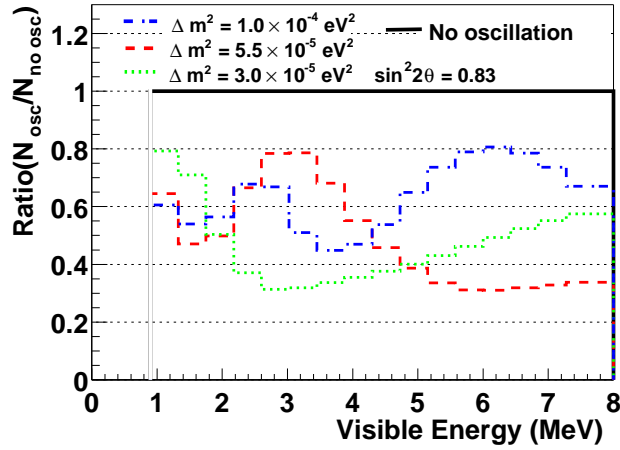


Figure 7.6: The distortions of the expected reactor $\bar{\nu}_e$ energy spectra at the different neutrino oscillation parameters.

the neutrino flavor transition. In the Fig.7.7, the observed prompt energy spectrum and the background spectrum as well as the expected reactor spectrum with no oscillation case are shown. A clear deficit of events is observed.

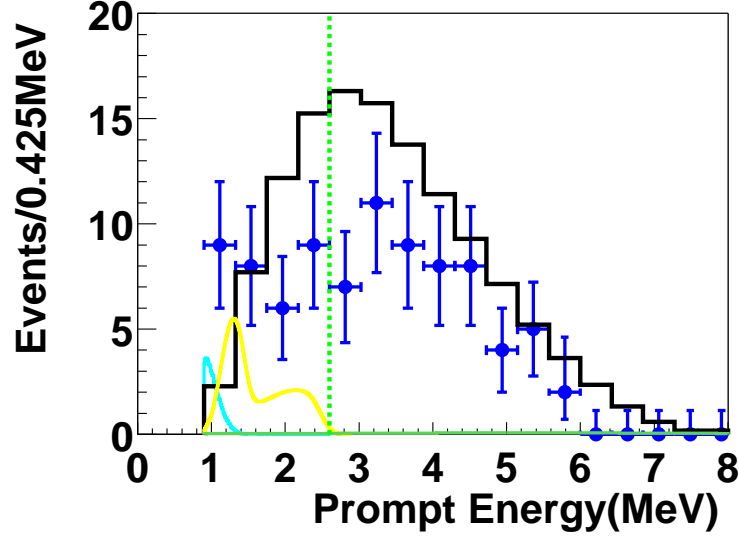


Figure 7.7: Energy spectrum of the observed prompt events (solid circles with error bars), as well as the expected no oscillation spectrum (histogram). The vertical dashed line corresponds to the analysis threshold at 2.6 MeV. Geo $\bar{\nu}_e$ and accidental background spectra are also shown.

7.2 Summary of the Systematic Uncertainties

Table.7.5 shows the summary of the systematic uncertainties for the $\bar{\nu}_e$ detection. The uncertainties of the reactor $\bar{\nu}_e$ flux and detector systematics are classified. The items upper region in the table corresponds to the reactor $\bar{\nu}_e$ flux and that lower region to the detector systematics. The total systematic uncertainty is obtained by adding the individual errors in quadrature.

7.3 No Oscillation Probability

In the previous chapters, it is shown that the number of observed events is 54 events and that of expected events are 86.8 events. The background rates contaminated in the observed events are 0.95 ± 0.99 events. The ratio of the observed and the expected events is $(54 - 0.95) / 86.8 = 0.611$. The statistical error is calculated to be ± 0.085 . The

Error source	Uncertainty
Reactor $\bar{\nu}_e$ flux	
$\bar{\nu}_e$ Spectra	2.5 %
Thermal Power of Japanese Reactors	2.0 %
Chemical Composition of Fission	< 1.0 %
Other Reactors	~ 0.35 %
Korean Reactors	~ 0.3 %
Time lag	0.28 %
Cross Section	0.2 %
Distance from Reactors	< 0.1 %
Number of Targets	< 0.1 %
Long life Nuclei	0.023 %
Detector systematics	
Fiducial Cut	4.6 %
Energy Threshold	2.1 %
Space Correlation	2.1 %
Time Correlation	0.5 %
Livetime	0.07 %
Flasher Cut	<0.01 %
Noise Cut	<0.0002 %
Trigger Efficiency	negligible
Total	6.4 %

Table 7.5: Summary of the systematics for the $\bar{\nu}_e$ detection.

systematics for the $\bar{\nu}_e$ detection is summarized to be 6.4%. Including the background systematics ± 0.99 events, total systematic uncertainty for the ratio is calculated to be ± 0.041 . So the ratio of the detected versus expected reactor events is summarized as 0.611 ± 0.085 (stat.) ± 0.041 (sys.).

The probability that the observed events at KamLAND is explained by statistical fluctuation without neutrino oscillation is calculated as following.

$$P = \frac{1}{\sqrt{2\pi}\sigma} \int_0^\infty e^{-\frac{(N^{\text{exp}} - x)^2}{2\sigma^2}} \sum_{n=0}^{N^{\text{obs}}} P(n) dx,$$

where N^{exp} means the mean value of the expected events, $86.8 + 0.95$, σ is the total systematic error $\sqrt{(86.8 \times 0.064)^2 + 0.99^2} = 5.66$ and $N^{\text{obs}} = 54$. $P(n)$ is the Poisson distribution with the mean value x as

$$P(n) = \frac{x^n}{n!} e^{-x}.$$

The expected events are assumed Gaussian distribution and the observed events are assumed Poisson distribution. The convolution of those relations is calculated and the probability of no oscillation is found to be 0.05 %.

For the first time, KamLAND has detected the reactor $\bar{\nu}_e$ disappearance at a high confidence level (99.95 %). Since one expects a negligible reduction of $\bar{\nu}_e$ flux from the SMA, LOW and VAC solar neutrino solutions, the LMA region is the only remaining oscillation solution.

Fig.7.8 shows the ratio of measured to expected flux for KamLAND as well as previous reactor experiments as a function of the average distance from the source.

7.4 Oscillation Analysis

As the ratio of detected events versus expected reactor events is 0.611 ± 0.085 (stat.) ± 0.041 (sys.), the disappearance of the reactor $\bar{\nu}_e$ is confirmed for the first time at the 99.95 % confidence level. So assuming the two-flavor neutrino oscillations, the rate analysis for the allowed oscillation parameters is performed.

We define the χ^2 as

$$\chi^2 = \frac{(R^{\text{detect}} - R^{\text{theory}})^2}{\sigma^2}$$

where $\sigma = \sqrt{\sigma_{\text{sys}}^2 + \sigma_{\text{sta}}^2}$, $\sigma_{\text{sys}} = 0.041$ and $\sigma_{\text{sta}} = 0.085$ being the total systematic and statistical error in the KamLAND data respectively, and $R^{\text{detect}} = 0.611$. R^{theory} is the ratio of $N(\sin^2 2\theta, \Delta m^2)$ to $N(\text{no oscillation})$, where $N(\sin^2 2\theta, \Delta m^2)$ means the expected number of events at the case of the oscillation parameters $(\sin^2 2\theta, \Delta m^2)$ and $N(\text{no oscillation})$ means the expected number of events without oscillation.

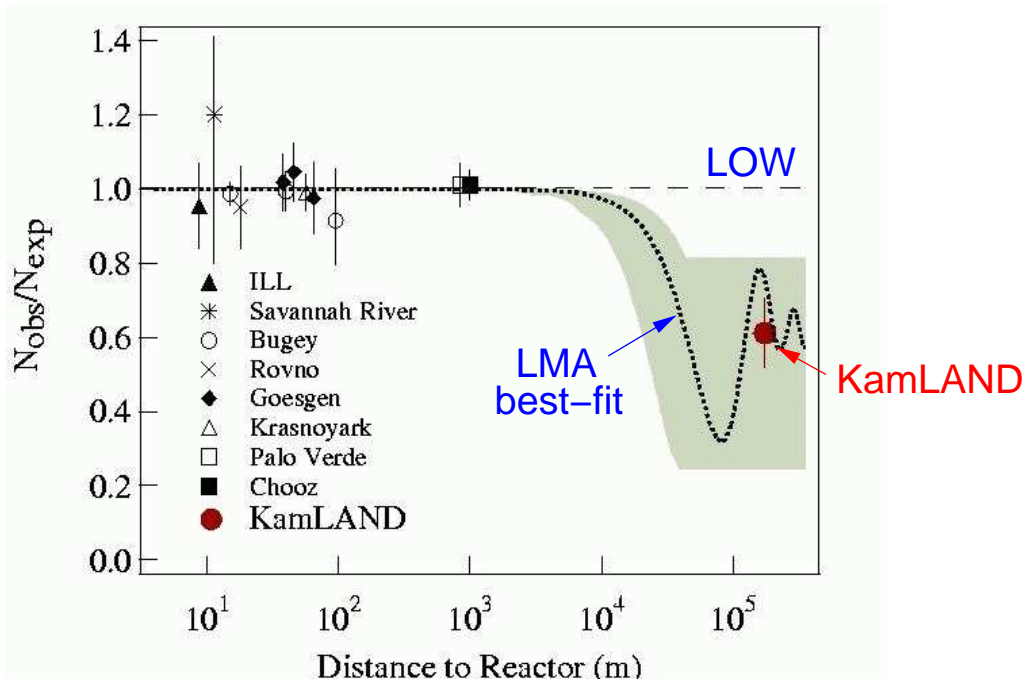


Figure 7.8: The ratio of measured to expected $\bar{\nu}_e$ flux from reactor experiments[58]. The solid dot is the KamLAND point plotted at a flux-weighted average distance (the dot size is indicative of the spread in reactor distances). The shaded region indicates the range of flux predictions corresponding to the 95 % C.L. LMA region found in a global analysis of the solar neutrino data[57]. The dotted curve corresponds to $\sin^2 2\theta = 0.833$ and $\Delta m^2 = 5.5 \times 10^{-5} \text{ eV}^2$ [57] and is representative of recent best-fit LMA predictions while the dashed curve shows the case of small mixing angles (or no oscillation).

Fig.7.9 shows the excluded regions of neutrino oscillation parameters for the rate analysis at 90%, 95%, 99% and 99.73% C.L. with $\chi^2 \geq 2.71, 3.84, 6.63$ and 9.00 , respectively. The 95 % C.L. allowed region of the Large Mixing Angle solution of solar neutrino experiments is also shown as a dark shaded region [57].

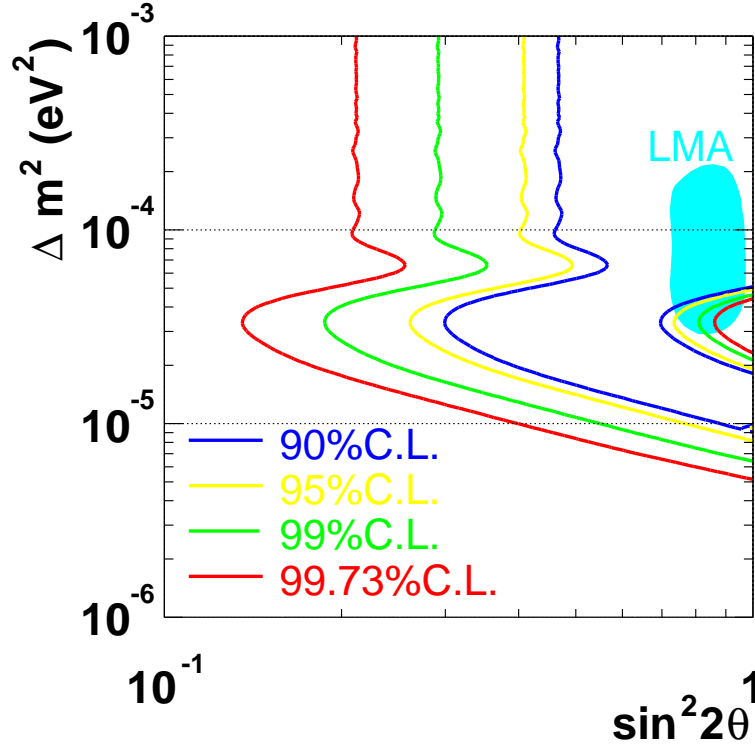


Figure 7.9: Excluded regions of neutrino oscillation parameters for the rate analysis at 90%, 95%, 99% and 99.73% C.L. The 95% C.L. allowed region of the Large Mixing Angle (LMA) solution of solar neutrino experiments [57] is also shown. All regions look identical under $\theta \leftrightarrow (\pi/2 - \theta)$ except for the LMA region.

All LMA regions except for smaller Δm^2 regions are allowed by this rate analysis. The LOW solution, which was the solution remained by the global analysis of all the solar experiments at the 99.73 % C.L., is now excluded at more than 99.73% C.L from this KamLAND result. So, the LMA region is the only remaining oscillation solution consistent with the KamLAND result, and the allowed LMA region is reduced slightly by only the rate analysis. We found the reactor $\bar{\nu}_e$ at this time in the 145.1 days sample. Future measurements with greater statistical precision and reduced systematic uncertainties will enable KamLAND to provide a high-precision measurement of the neutrino oscillation

parameters.

Taken into account of three generations of neutrinos, the exact survival probability $P(\bar{\nu}_e \rightarrow \bar{\nu}_e)$ is given by [9],

$$\begin{aligned} P(\bar{\nu}_e \rightarrow \bar{\nu}_e) = & 1 - \sin^2 2\theta_{13} \sin^2 \frac{\Delta m_{31}^2 L}{4E} \\ & - \frac{1}{2} \cos^2_{12} \sin^2 2\theta_{13} \sin \frac{\Delta m_{31}^2 L}{2E} \sin \frac{\Delta m_{21}^2 L}{2E} \\ & - (\cos^4 \theta_{13} \sin^2 2\theta_{12} + \cos^2 \theta_{12} \sin^2 2\theta_{13} \cos \frac{\Delta m_{31}^2 L}{2E}) \sin^2 \frac{\Delta m_{21}^2 L}{4E}. \end{aligned}$$

The best fit value of $|\Delta m_{31}^2|$ is given by $|\Delta m_{31}^2| = 2.5 \times 10^{-3} eV^2$ from the Super-Kamiokande atmospheric neutrino data [31]. Then, the third and the fifth terms can be ignored. In KamLAND, as $\Delta m_{31}^2 L/4E$ is about 100 and $\sin^2 \frac{\Delta m_{31}^2 L}{4E}$ is about 1/2, the equation is simply,

$$\begin{aligned} P(\bar{\nu}_e \rightarrow \bar{\nu}_e) & \cong 1 - \frac{1}{2} \sin^2 2\theta_{13} - \cos^4 \theta_{13} \sin^2 2\theta_{12} \sin^2 \frac{\Delta m_{21}^2 L}{4E} \\ & \cong \sin^4 \theta_{13} + \cos^4 \theta_{13} - \cos^4 \theta_{13} \sin^2 2\theta_{12} \sin^2 \frac{\Delta m_{21}^2 L}{4E} \end{aligned}$$

The CHOOZ experiment [34] established an upper limit of $\sin^2 2\theta_{13} < 0.15$, or $\cos^4 \theta_{13} \geq 0.92$, the equation can be rewritten,

$$P(\bar{\nu}_e \rightarrow \bar{\nu}_e) \cong \cos^4 \theta_{13} [1 - \sin^2 2\theta_{12} \sin^2 \frac{\Delta m_{21}^2 L}{4E}]$$

In the limit of $\cos^4 \theta_{13} \simeq 1$, $\sin^2 2\theta_{12}$ and Δm_{21}^2 correspond to the $\sin^2 2\theta$ and Δm^2 of the two generation case, respectively. In KamLAND, $\sin^2 2\theta = 1.0$ corresponds approximately to $0.86 < \sin^2 2\theta_{12} < 1.0$. The rate analysis showed that the allowed regions of $\sin^2 2\theta$ at KamLAND were $0.3 < \sin^2 2\theta < 0.7$ around oscillation maximum, $0.45 < \sin^2 2\theta < 1.0$ with larger Δm^2 at 90% C.L. These results correspond to $0.26 < \sin^2 2\theta_{12} < 0.7$ around oscillation maximum, $0.39 < \sin^2 2\theta_{12} < 1.0$ with larger Δm_{12}^2 , respectively.

It is conventional to ignore matter effects in analyzing the reactor experiments, essentially because the path length in the earth for the reactor $\bar{\nu}_e$ rather small. However, matter effects at KamLAND can influence the calculated $\bar{\nu}_e$ event rate by as much as 4% if the mass and mixing angle are near the region of maximum sensitivity [59]. Assuming that the $\bar{\nu}_e$ traverse a constant density medium ($\rho = 2.7 \text{ g/cm}^3$), MSW effect at KamLAND is studied. The fractional difference in the event rate with and without including matter effects in the earth is defined as $(N_{\text{MSW}} - N_{\text{VAC}})/N_{\text{VAC}}$. Fig.7.10 shows the fractional difference with and without including matter effects. The region with the largest difference is the smaller Δm^2 LMA regions, and the difference is $\sim 4\%$ there. However,

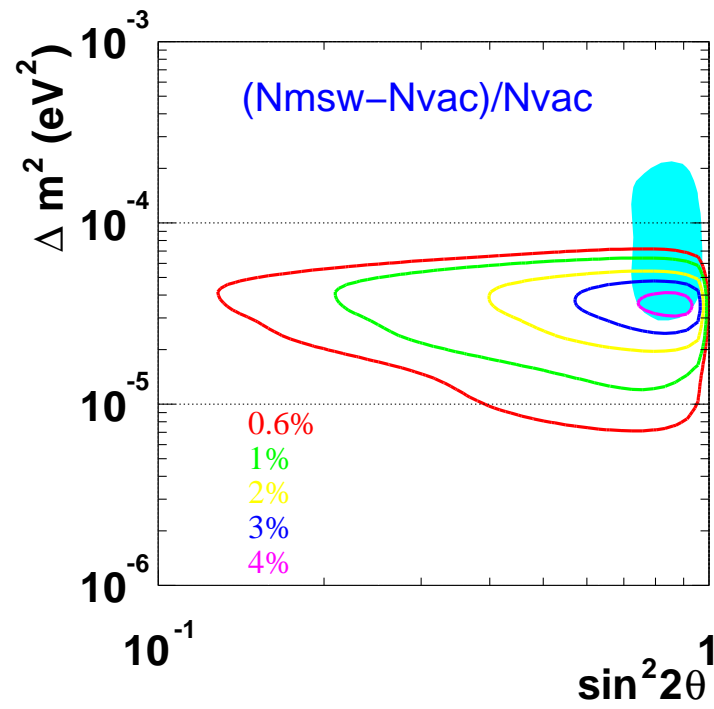


Figure 7.10: MSW effect at KamLAND

these regions are partly excluded by the rate analysis only. The rate analysis with including matter effects in the earth is also performed to check if the matter effect changes the result without including the matter effect. χ^2 definition is same as above. Fig.7.11 shows the excluded regions of neutrino oscillation parameters for the rate analysis at 90%, 95%, 99% and 99.73% C.L. The 95 % C.L. allowed region of the Large Mixing Angle solution of solar neutrino experiments is also shown. The difference between with and without matter effects is found to be quite small at present.

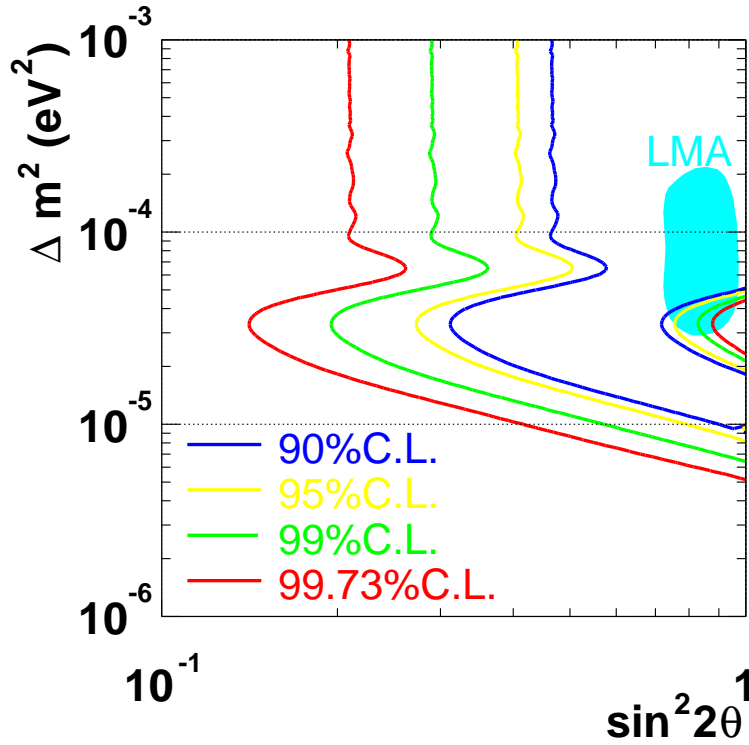


Figure 7.11: Excluded regions of neutrino oscillation parameters for the rate analysis at 90%, 95%, 99% and 99.73% C.L. with including matter effects. The 95% C.L. allowed region of the Large Mixing Angle (LMA) solution of solar neutrino experiments [57] is also shown.

7.5 Impact for Neutrino Physics

The reactor $\bar{\nu}_e$ disappearance was found for the first time by this analysis using 145.1 days data of the KamLAND. In the previous reactor experiment, the best sensitivity for the

mass squared difference Δm^2 of the two flavor neutrino oscillation was $\sim 10^{-3} \text{ eV}^2$. KamLAND made use of the long baseline from all of Japanese reactors to the detector, whose average distance is $\sim 180 \text{ km}$, and measured the $\bar{\nu}_e$ flux. The sensitivity was 100 times improved and could test the allowed regions of the neutrino oscillation parameters from the solar neutrino problem. This reactor $\bar{\nu}_e$ disappearance was consistent with the LMA MSW solution in the context of the two flavor neutrino oscillation, and the other solutions such as LOW (or SMA, VAC already excluded by solar neutrino experiments) was excluded at the 99.95% C.L. This means the solar neutrino deficit is independently confirmed by the terrestrial anti-neutrino sources, reactors. Assuming CPT invariance and two flavor oscillation,

$$\begin{aligned} P(\bar{\nu}_e \rightarrow \bar{\nu}_\mu) &= P(\nu_\mu \rightarrow \nu_e), \\ P(\nu_\mu \rightarrow \nu_e) &= P(\nu_e \rightarrow \nu_\mu). \end{aligned}$$

Thus, when CPT holds,

$$P(\bar{\nu}_e \rightarrow \bar{\nu}_\mu) = P(\nu_e \rightarrow \nu_\mu).$$

That is, the probability for oscillation of an anti-neutrino is the same as that for a neutrino. In the three flavor oscillation case, the probability can differ only by the contribution of CP violating phase. Now, the results of solar neutrino experiments and this reactor experiment are consistent. If any discrepancy of these measurements would be found, this will be evidence for a violation of CPT.

Next step for neutrino physics is not only to measure the precise measurement of the oscillation parameters, but also to find the magnitude of CP violating phase. Many projects of accelerator-based long baseline neutrino oscillation experiments are proposed for this purpose [60]. CP violating phase can be probed by comparing the flavor transformation probabilities of neutrinos and anti-neutrinos. The difference of the probabilities can be written down following in the absence of matter effect,

$$\begin{aligned} P(\nu_e \rightarrow \nu_\mu) - P(\bar{\nu}_e \rightarrow \bar{\nu}_\mu) &= -16 \sin \theta_{12} \cos \theta_{12} \sin \theta_{13} \cos^2 \theta_{13} \sin \theta_{23} \cos \theta_{23} \\ &\quad \sin \delta \sin \frac{\Delta m_{12}^2 L}{4E} \sin \frac{\Delta m_{13}^2 L}{4E} \sin \frac{\Delta m_{23}^2 L}{4E}, \end{aligned}$$

where δ is CP-violating phase [61]. This indicates that the observation of CP violation in neutrino oscillations is possible only if θ_{12} and Δm_{12}^2 are large and the atmospheric parameters are also large, as has been established by the atmospheric data. θ_{13} is also need to be large enough to explore CP violation. The limit for the $\sin^2 2\theta_{13} < 0.15$ is obtained by the CHOOZ experiment at present. This analysis result has shown that the LOW solution, which has smaller Δm^2 solution, is eliminated and Δm_{12}^2 and θ_{12} are large enough to render the experimental search for CP violation possible. That is, this analysis leads the neutrino physics to the exploration of CP violation in the lepton sector.

Maki-Nakagawa-Sakata [62] neutrino mixing matrix can be written as

$$U = \begin{array}{c} \nu_e \\ \nu_\mu \\ \nu_\tau \end{array} \begin{array}{ccc} \nu_1 & \nu_2 & \nu_3 \\ \left(\begin{array}{ccc} c_{12}c_{13} & s_{12}c_{13} & s_{13} \\ -s_{12}c_{23} - c_{12}s_{23}s_{13}e^{i\delta} & -c_{12}c_{23} - s_{12}s_{23}s_{13}e^{i\delta} & s_{23}c_{13}e^{i\delta} \\ s_{12}s_{23} - c_{12}c_{23}s_{13}e^{i\delta} & -c_{12}s_{23} - s_{12}c_{23}s_{13}e^{i\delta} & c_{23}c_{13}e^{i\delta} \end{array} \right) \end{array},$$

where $c_{ij} \equiv \cos \theta_{ij}$, $s_{ij} \equiv \sin \theta_{ij}$, $0 \leq \theta_{ij} \leq \pi/2$ and δ is the CP-violating Dirac phase. The mixing angle θ_{23} is in the ranges of $\sin^2 2\theta_{23} > 0.85$ from atmospheric neutrino data [63]. In KamLAND, the rate analysis shows that the mixing angle θ_{12} is in the ranges of $0.26 < \sin^2 2\theta_{12} < 0.7$ around oscillation maximum, $0.45 < \sin^2 2\theta_{12} < 1.0$ with larger Δm^2 . The limit of θ_{13} from CHOOZ experiment is $\sin^2 2\theta_{13} < 0.15$. The MNS matrix is simply written down by those data including this rate analysis result of $0.45 < \sin^2 2\theta_{12} < 1.0$ with larger Δm^2 ($\Delta m^2 \geq 10^{-4} eV^2$), neglecting the CP-violating term,

$$U = \begin{pmatrix} 0.69 - 0.93 & 0.35 - 1/\sqrt{2} & < 0.2 \\ 0.25 - 0.72 & 0.50 - 0.88 & 0.54 - 1/\sqrt{2} \\ 0.04 - 0.65 & 0.39 - 0.78 & 1/\sqrt{2} - 0.69 \end{pmatrix},$$

where the matrix elements are confined to the case of $\nu_\mu < \nu_\tau$, and only the modulus of the elements are shown. If the Δm^2 is around oscillation maximum, ($\Delta m^2 \simeq 3 \times 10^{-5} eV^2$),

$$U = \begin{pmatrix} 0.86 - 0.97 & 0.25 - 0.48 & < 0.2 \\ 0.18 - 0.53 & 0.62 - 0.87 & 0.54 - 1/\sqrt{2} \\ < 0.34 & 0.48 - 0.76 & 1/\sqrt{2} - 0.69 \end{pmatrix}.$$

All matrix elements are reasonably constrained with the present neutrino oscillation data and this analysis result. It is characteristic that all elements except for U_{e3} are sizable. These information of matrix elements and the Δm^2 s are useful to determine the condition of the experiments such as long-baseline neutrino experiments with strong neutrino beams which aim to detect CP violation effects. If the LOW solution of the solar neutrino problem would be real solution, the small Δm_{12}^2 pushes the CP violation effect outside the range feasible with accelerator experiments. Because this analysis is consistent with LMA solution, not LOW solution, neutrino physics to the exploration of CP violation is now opened.

Chapter 8

Conclusion

Reactor $\bar{\nu}_e$ flux and energy spectrum have been measured using 145.1 day's samples (162 ton \cdot year) of KamLAND from March 4 2002 to October 6 2002, and the reactor $\bar{\nu}_e$ disappearance was found for the first time. The ratio of the number of observed inverse- β decay events to the expected number of events without disappearance is 0.611 ± 0.085 (stat.) ± 0.041 (syst.) for $\bar{\nu}_e$ energies > 3.4 MeV. This deficit of events is inconsistent with the expected number of events at 99.95 % confidence level. In the context of two-flavor neutrino oscillations with CPT invariance, this reactor $\bar{\nu}_e$ disappearance result excludes all oscillation solutions but the LMA MSW solution to the solar ν_e problem. The MSW effect at KamLAND is also studied, and it is found that the effect is small enough for the rate analysis. Next step for neutrino physics is not only to measure the oscillation parameters precisely, but also to explore CP violating effect. Atmospheric neutrino experiments have already shown the Δm_{23}^2 and $\sin^2 \theta_{23}$ are large. This result has shown that Δm_{12}^2 and $\sin^2 2\theta_{12}$ are large enough to explore CP violation including solar neutrino experiments. That is, this analysis leads the neutrino physics to the exploration of CP violation in the lepton sector.

Appendix A

No Spallation Cut Analysis

Cylinder cut along the muon track are applied to remove the correlated backgrounds of ^8He and ^9Li induced by muon spallation events when the final sample of $\bar{\nu}_e$ events are selected. To confirm the efficiency of this cylinder cut, alternative analysis without the spallation cut are performed [64]. The number of events per unit time which satisfies the $\bar{\nu}_e$ event signature following a time t after a muon traversal is given by

$$\frac{dN(t)}{dt} = \frac{N_{spall}}{\tau} e^{-t/\tau} + N_{\bar{\nu}_e} R_\mu e^{-tR_\mu},$$

where N_{spall} is the number of spallation products in the final data sample, τ is the isotope lifetime, $N_{\bar{\nu}_e}$ is the number of $\bar{\nu}_e$ events, and R_μ is the rate of incident muons. Fig.A.1 (Fig.A.2) shows the timing distribution from the last muon of the events selected by the normal reactor anti-neutrino selection criteria with prompt energy larger than 0.9 MeV (2.6 MeV) without spallation cut. Solid histogram shows the timing distribution of the total events and the dashed histogram shows that of the events with cylinder cut. The fitting using above function is done where $N_{\bar{\nu}_e}$ and N_{spall} are treated as free parameters and τ and R_μ are fixed to 0.2568 sec and 0.34 Hz. The results show the expected events of the reactor anti-neutrino are 98.48 ± 11.5 (57.66 ± 8.7) events and the spallation events are 75.95 ± 10.44 (71.6 ± 9.5) events for energy larger than 0.9 (2.6) MeV. The livetime of this analysis is just longer than that of cylinder cut, 145.09 days, because the spallation cut reduces the livetime by 11 %. To compare this fitting result with the number of $\bar{\nu}_e$ events detected by the analysis with cylinder cut, the effective livetime ratio is multiplied to the fitting result. So the effective $\bar{\nu}_e$ events are 87.6 ± 10.2 (51.3 ± 7.7). The detected $\bar{\nu}_e$ events by cylinder cut are 86 (54) events and 1.1 ± 1.0 (0.94 ± 0.85) $^8\text{He}/^9\text{Li}$ events are included in that samples. So the total $\bar{\nu}_e$ events are estimated 85 (53) events. This result is consistent with the fitting result by 3% accuracy.

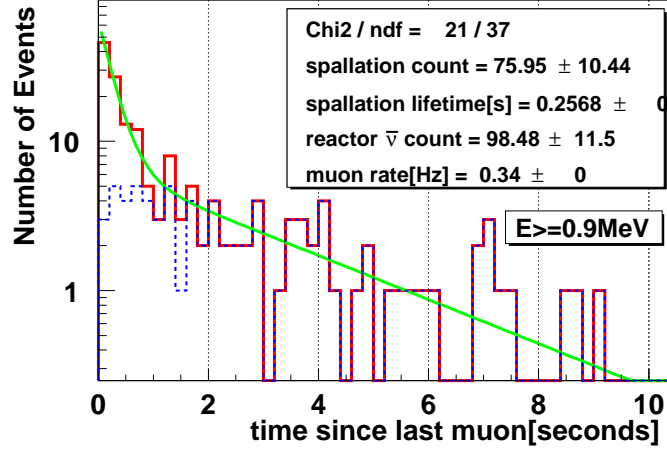


Figure A.1: The timing distribution from the last muon of events selected by the reactor anti-neutrino selection criteria with prompt energy larger than 0.9 MeV without spallation cut. Solid histogram shows the timing distribution of the total events and the dashed histogram shows that of the events with spallation cut.

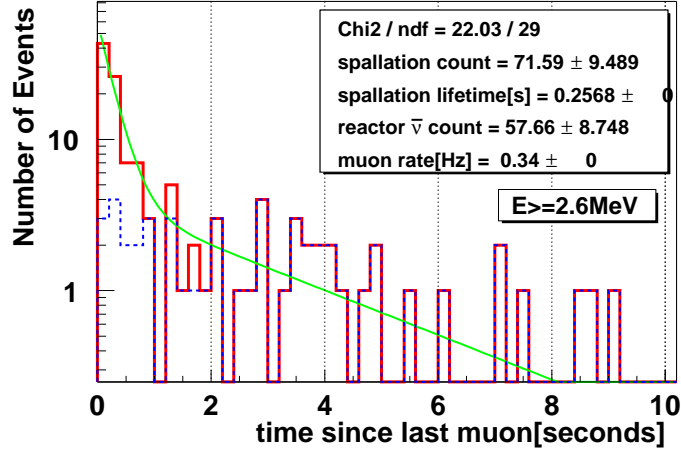


Figure A.2: The timing distribution from the last muon of events selected by the reactor anti-neutrino selection criteria with prompt energy larger than 2.6 MeV without spallation cut. Solid histogram shows the timing distribution of the total events and the dashed histogram shows that of the events with spallation cut.

Bibliography

- [1] W. Pauli, Letter to L.Meitner and her colleagues (letter open to the participants of the conference in Tübingen) (1930).
- [2] F. Reines and C. L. Cowan, *Nature* **178**, 446 (1956).
- [3] G. Danby *et al.*, *Phys. Rev. Lett.* **9**, 36 (1962).
- [4] M. L. Perl *et al.*, *Phys. Rev. Lett.* **35**, 1489 (1975).
- [5] K. Kodama *et al.* [DONUT Collaboration], *Phys. Lett. B* **504**, 218 (2001) [arXiv:hep-ex/0012035].
- [6] t. L. Group and t. S. Group [OPAL Collaboration], arXiv:hep-ex/0212036.
- [7] V. M. Lobashev *et al.*, *Phys. Lett. B* **460**, 227 (1999), or
- [8] L. Wolfenstein, *Phys. Rev. D* **17**, 2369 (1978), *D* **20**, 2634 (1979) and S. P. Mikheyev and A. Y. Smirnov, *Nuovo Cim.* **9 C**, 17 (1986)
- [9] H. Minakata, H. Sugiyama, O. Yasuda, K. Inoue and F. Suekane, arXiv:hep-ph/0211111.
C. Weinheimer *et al.*, *Phys. Lett. B* **460**, 219 (1999).
- [10] A. Aguilar *et al.* [LSND Collaboration], *Phys. Rev. D* **64**, 112007 (2001) [arXiv:hep-ex/0104049].
- [11] K. Hagiwara *et al.* [Particle Data Group Collaboration], *Phys. Rev. D* **66**, 010001-401 (2002).
- [12] B. Armbruster *et al.* [KARMEN Collaboration], *Phys. Rev. D* **65**, 112001 (2002) [arXiv:hep-ex/0203021].
- [13] A. O. Bazarko [BooNE Collaboration], arXiv:hep-ex/0210020.
- [14] S. Fukuda *et al.* [Super-Kamiokande Collaboration], *Phys. Rev. Lett.* **86**, 5656 (2001) [arXiv:hep-ex/0103033].

- [15] R. J. Davis, D. S. Harmer and K. C. Hoffman, Phys. Rev. Lett. **20**, 1205 (1968).
- [16] J. N. Bahcall, S. Basu and M. H. Pinsonneault, Phys. Lett. B **433**, 1 (1998) [arXiv:astro-ph/9805135].
- [17] B. T. Cleveland *et al.*, Astrophys. J. **496**, 505 (1998).
- [18] K. S. Hirata *et al.* [KAMIOKANDE-II Collaboration], Phys. Rev. Lett. **65**, 1297 (1990).
- [19] Y. Fukuda *et al.* [Kamiokande Collaboration], Phys. Rev. Lett. **77**, 1683 (1996).
- [20] W. Hampel *et al.* [GALLEX Collaboration], Phys. Lett. B **447**, 127 (1999).
- [21] J. N. Abdurashitov *et al.* [SAGE Collaboration], Phys. Rev. C **60**, 055801 (1999) [arXiv:astro-ph/9907113].
- [22] S. Fukuda *et al.* [Super-Kamiokande Collaboration], Phys. Lett. B **539**, 179 (2002) [arXiv:hep-ex/0205075].
- [23] Q. R. Ahmad *et al.* [SNO Collaboration], Phys. Rev. Lett. **89**, 011301 (2002) [arXiv:nucl-ex/0204008].
- [24] Q. R. Ahmad *et al.*, Phys. Rev. Lett. **89**, 011302 (2002).
- [25] R. Becker-Szendy *et al.*, Phys. Rev. D **46**, 3720 (1992).
- [26] W. W. Allison *et al.* [Soudan-2 Collaboration], Phys. Lett. B **449**, 137 (1999) [arXiv:hep-ex/9901024].
- [27] Y. Fukuda *et al.* [Kamiokande Collaboration], Phys. Lett. B **335**, 237 (1994).
- [28] Y. Fukuda *et al.* [Super-Kamiokande Collaboration], Phys. Lett. B **436**, 33 (1998) [arXiv:hep-ex/9805006] for Multi-GeV and Y. Fukuda *et al.* [Super-Kamiokande Collaboration], Phys. Lett. B **433**, 9 (1998) [arXiv:hep-ex/9803006] for Sub-GeV.
- [29] K. Daum [Frejus Collaboration.], Z. Phys. C **66**, 417 (1995).
- [30] Y. Fukuda *et al.* [Super-Kamiokande Collaboration], Phys. Rev. Lett. **81**, 1562 (1998) [arXiv:hep-ex/9807003].
- [31] M. Shiozawa, presented at the XXth Int.Conf. on Neutrino Physics and Astrophysics, Munich, May 2002.
- [32] M. H. Ahn *et.al.*, arXiv:hep-ex/0212007.
- [33] Y. Declais *et al.*, Phys. Lett. B **338**, 383 (1994).

- [34] M. Apollonio *et al.* [CHOOZ Collaboration], Phys. Lett. B **466**, 415 (1999) [arXiv:hep-ex/9907037].
- [35] F. Boehm *et al.*, Phys. Rev. D **64**, 112001 (2001) [arXiv:hep-ex/0107009].
- [36] P. Vogel and J. F. Beacom, Phys. Rev. D **60**, 053003 (1999) [arXiv:hep-ph/9903554] and P. Vogel, Phys. Rev. D **29**, 1918 (1984).
- [37] Andriy Kurylov 2002 (private communication).
- [38] Y. Declais *et al.*, Phys. Lett. B **338** (1994) 383.
- [39] L. H. Miller, UMI-30-00068
- [40] J. B. Birks, Proc. Phys. Soc. A **64**, 874 (1951).
- [41] K. Schreckenbach *et al.*, Phys. Lett. B **160**, 325 (1985) for ^{235}U , A. A. Hahn *et al.*, Phys. Lett. B **218**, 365 (1989) for ^{239}Pu and ^{241}Pu . Low energy bin was taken from P. Vogel and J. Engel, Phys. Rev. D **39**, 3378 (1989).
- [42] P. Vogel (private communication).
- [43] <http://www.insc.anl.gov/>
- [44] Richard B. Firestone and Virginia S. Shirley, “Table of Isotopes, Eighth Edition”, John Wiley & Sons, Inc. (1996).
- [45] W. R. Nelson and J. Liu, SLAC-TN-92-001
- [46] T. Hagner *et al.*, Astroparticle Physics **14** 33-47 (2000).
- [47] R. S. Raghavan, S. Schoenert, S. Enomoto, J. Shirai, F. Suekane and A. Suzuki, Phys. Rev. Lett. **80** 635 (1998).
- [48] R. S. Raghavan, arXiv:hep-ex/0208038.
- [49] T. K. Gaisser, T. Stanev and G. Barr, Phys. Rev. D **38** 85 (1988).
- [50] M. Honda, T. Kajita, K. Kawahara and S. Midorikawa, Phys. Rev. D **52**, 4985 (1995).
- [51] G. Battistoni, A. Ferrari, T. Montaruli and P. R. Sala, arXiv:hep-ph/9907408.
- [52] <http://vldb.gsi.go.jp/sokuchi/coordinates/localtrans.html>.
- [53] Coordinate Transformation Program TKY2WGS, Geographical Survey Institute.
- [54] H. Noumi *et al.*, Nucl. Instrum. Meth. A **398**, 399 (1997).

- [55] <http://www.insc.anl.gov/>.
- [56] P. Vogel (private communication).
- [57] G. L. Fogli *et al.*, Phys. Rev. D **66**, 053010 (2002).
- [58] K. Hagiwara *et al.* [Particle Data Group Collaboration], Phys. Rev. D **66**, 010001-406 (2002).
- [59] J. N. Bahcall, M. C. Gonzalez-Garcia and C. Pena-Garay, arXiv:hep-ph/0212147.
- [60] Y. Itow *et al.*, “The JHF-Kamioka neutrino project,” arXiv:hep-ex/0106019,
M. V. Diwan, “Status of the MINOS experiment,” arXiv:hep-ex/0211026,
M. Komatsu, P. Migliozzi and F. Terranova, “Sensitivity to Theta(13) of the CERN
to Gran Sasso neutrino beam,” arXiv:hep-ph/0210043,
H. Minakata, H. Nunokawa and S. Parke, “The complementarity of eastern and
western hemisphere long-baseline neutrino oscillation experiments,” arXiv:hep-
ph/0301210.
- [61] A. de Gouvea and H. Murayama, arXiv:hep-ph/0301050.
- [62] Z. Maki, M. Nakagawa and S. Sakata, Prog. Theor. Phys. **28**, 870 (1962).
- [63] X. G. He and A. Zee, arXiv:hep-ph/0301092.
- [64] Alternate Method to Subtract Spallation Background in KamLAND, G. A. H-Smith
and R. D. McKeown, not published.